UNIVERSITY OF SHEFFIELD

Application of computational limit analysis to soil-structure interaction in masonry arch bridges

by

Dong Nguyen

A thesis submitted in partial fulfillment for the
degree of Doctor of Philosophy

in the

Department of Civil and Structural Engineering

December 2008

Declaration of Authorship

I, Dong Nguyen, declare that this thesis entitled, 'Application of computational limit analysis to soil-structure interaction in Masonry arch bridges' and the work presented in it are my own. I confirm that:

- This work was done wholly or mainly while in candidature for a research degree at this University.

- Where any part of this thesis has previously been submitted for a degree or any other qualification at this University or any other institution, this has been clearly stated.

- Where I have consulted the published work of others, this is always clearly attributed.

- Where I have quoted from the work of others, the source is always given. With the exception of such quotations, this thesis is entirely my own work.

- I have acknowledged all main sources of help.

- Where the thesis is based on work done by myself jointly with others, I have made clear exactly what was done by others and what I have contributed myself.

Signed:

Date:

Abstract

For the assessment of Masonry Arch Bridges (MAB), many structural and material models have been applied, ranging from sophisticated non-linear finite element analysis models to much simpler rigid-block limit analysis models. i.e. elastic and plastic methods respectively. The application of elastic analysis to MAB suffers many drawbacks since it requires full mechanical characterization of ancient masonry structures. The mechanical characterization of ancient masonry is difficult since these structures have typically undergone a century or more of environmental deterioration and in many cases have been already subjected to extensive modification. Also, sophisticated material models generally require specialized parameters that are hard to assess, particularly if non-destructive tests are used. In these cases practicing engineers typically favour simpler material models, involving fewer parameters. Thus non-linear finite element methods or other sophisticated models may not be a good choice for the assessment of MAB, while simplified approaches for example based on limit analysis principles are likely to be more appropriate. In this research, a holistic computational limit analysis procedure is presented which involves modelling both soil and masonry components explicitly. Masonry bridge parts are discretized using rigid blocks whilst the soil fill is discretized using deformable triangular elements and modelled as a Mohr-Coulomb material with a tension cut-off. Lower and upper bound estimates of the collapse load are obtained. Results are compared with those from recently performed bridge tests carried out in collaboration with the University of Salford. A key project finding is that the use of peak soil strength parameters in limit analysis models is inappropriate when the soil is modelled explicitly. However, use of mobilized strengths appears to be a promising way forward, yielding much closer correlation with experimental data.

Acknowledgements

Contents

List of Figures

List of Tables

Abbreviations

MP	Mathematical Programming
LP	Linear Programming
NLP	Non Linear Programming
MAB	Masonry Arch Bridge
PWL	Piecewise Linear
FELA	Finite Element Limit Analysis
FEA	Finite Element Analysis (conventional elastic or elasto-plastic)
MSLA	Mobilized Strength Limit Analysis
SSI	Soil-Structure Interaction
DLO	Discontinuity Layout Optimization
MEXE	Military Engineering Experimental Establishment
TRL	Transport Research Laboratory

Chapter 1

Introduction

1.1 Background

Masonry arch bridges are of substantial importance to the infrastructure of the
highway networks of Europe. Hundreds of thousands are still in service, despite
their age and the significant changes in loading conditions since their construction.
Most bridges were constructed over a century ago and were built to carry far
less loading than they are subject to today. With the current tendency towards
heavier vehicle weights, combined with the deterioration of the natural structural
materials from loading and environmental effects, it can no longer be assumed that
these bridges will remain capable of carrying all vehicles currently on the road
network. It is estimated that there are over forty thousand highway masonry arch
bridges in the UK in need of reassessment due to recent and anticipated European
Community Directives (Page, 1993). Consequently in recent years considerable
effort has been spent in order to obtain a better understanding of the behaviour
of masonry arch bridges.

The aim of the work described in this thesis has been to improve current limit
analysis assessment methods, and results from the model developed will be com-
pared with experimental data gleaned from carefully controlled laboratory tests.
Conventional limit analysis (and many other) models often suffer from the fact

that the anticipated influence of backfill generally needs to be stipulated in advance of an analysis; hence the soil-structure interaction model necessarily has to be simplified.
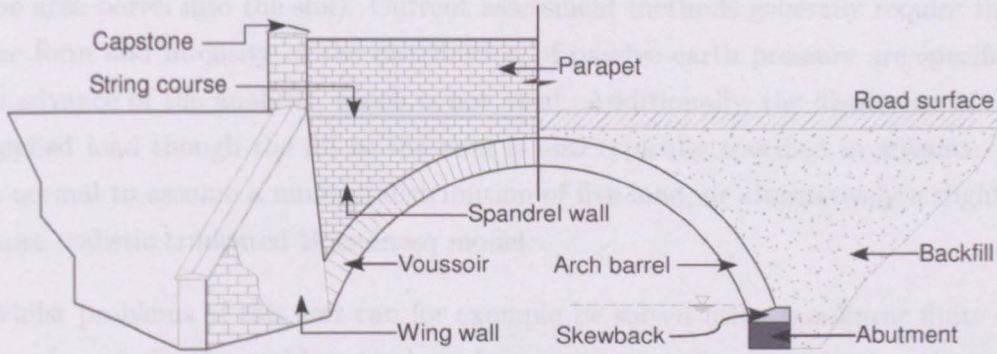
FIGURE 1.1: Typical masonry arch bridge
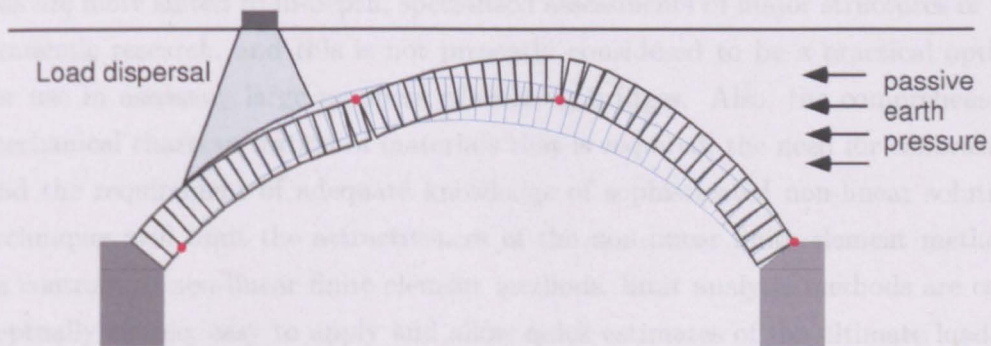
FIGURE 1.2: Soil-structure interaction in masonry arch bridge

Strictly speaking, soil-structure interaction (SSI) is present to some degree in every problem where a structural element is in contact with the ground. However, in current practice SSI is often neglected or inappropriately modelled. In some cases, neglecting SSI is quite reasonable and is justified by experience based on satisfactory performance of the resulting design. Examples include a footing foundation for a low-rise building and simple rigid retaining walls. Unfortunately, there are also cases where neglecting SSI can no longer be justified. In the case of masonry arch bridges, the load carrying capacity can be strongly influenced by the presence of backfill, the latter serving both to disperse applied loads and to provide restraint to sway of the arch barrel at the ultimate limit state. However, to model the effect

of passive earth pressure distribution, a reduced (empirically derived) factor of 1/3 is typically applied to the lateral earth pressure coefficient, K_p. In fact, passive earth pressures arise from deformation of the soil mass (e.g. the movement of the arch barrel into the soil). Current assessment methods generally require that the form and intensity of the distribution of passive earth pressure are specified in advance of the analysis, which is not ideal. Additionally, the dispersion of the applied load though the fill to the arch is also typically specified in advance. It is normal to assume a uniform distribution of live load, or alternatively a slightly more realistic truncated Boussinesq model.

Whilst problems of this sort can for example be solved using non-linear finite element analysis, the problem tends to be computationally expensive to solve and demands that the user has appropriate expertise. Non-linear finite element methods are more suited to in-depth, specialized assessments of major structures or for academic research, and this is not presently considered to be a practical option for use in assessing large numbers of existing bridges. Also, the comprehensive mechanical characterization of materials that is required, the need for calibration and the requirement of adequate knowledge of sophisticated non-linear solution techniques still limit the attractiveness of the non-linear finite element method. In contrast to non-linear finite element methods, limit analysis methods are conceptually simple, easy to apply and allow quick estimates of the ultimate load to be made. Limit analysis is currently used to solve various practical engineering problems (e.g. geotechnical, concrete slab and metal forming problems). In this research, a holistic computational limit analysis procedure is developed which involves modelling both soil and masonry components explicitly. The aims of this research will be achieved by carrying out the objectives, outlined in the following section.

1.2   Objectives and methodology

By the time the project started the coupled soil-structure limit analysis problem had received the attention of Italian researchers Cavicchi & Gambarotta (2005),

who also investigated the masonry arch bridge analysis problem. However only upper bound solutions were presented by them at that time ,no indication of the proximity of these to exact solutions was available. Results from their limit analysis model were not validated against bridge test data for which the constituent materials were well characterized. This made it difficult to draw firm conclusions. The aim was to address these issues in the present project. The main objective of this work is to investigate the performance of finite element limit analysis as a practical tool for the assessment of soil-arch interaction. In order to achieve this primary objective, the following tasks had to be undertaken:

- development of a finite element limit analysis model for combined soil and masonry problems, and initial verification of this through application to a number of standard benchmark problems.

- more in-depth verification of the model through application of this to a number of full scale bridge tests.

- implementation of enhancements to the model as proves necessary.

- consideration of other potential applications of the developed numerical model.

1.3   Thesis layout

Chapter 1-Introduction: This chapter gives a brief outline of the contents of this thesis, together with a statement of the issues investigated.

Chapter 2-Literature review: This chapter briefly reviews historical and current assessment methods applied to masonry arch bridges. Various methods of strengthening bridges are also outlined. The fundamental theory of plasticity and the basis of limit analysis are described and this chapter also looks at application of limit analysis to geomechanics and masonry problems, and contributions in these fields are recognized and discussed.

Chapter 3-Numerical limit analysis model of masonry-soil interaction: This chapter establishes a mathematical formulation which can be applied to masonry arch bridge structures. Both lower bound and upper bound formulations for soil and masonry are presented in detail. Numerical solutions obtained from the soil model are validated against benchmark literature solutions.

Chapter 4-Application of numerical limit analysis model to soil structure interaction problems: the numerical model developed in the previous chapter is used to analyse a number of laboratory bridges tested recently at Salford University. Results from the model are discussed and issues which arise are emphasised at the end of the chapter. An important conclusion is that soil strength mobilization is important when analysing masonry arch bridges. This chapter also identifies the need for an improved model.

Chapter 5-Mobilized strength limit analysis of masonry arch bridges: In this chapter the issues raised in chapter 4 are discussed and a new approach to solve the soil strength mobilization problem is introduced. The new approach is validated by comparing solutions with results from the literature. The new model is then used to re-analyse Salford tests.

Chapter 6- Discussion: A number of issues relating to the finite element limit analysis models developed are discussed. This chapter also includes consideration of potential other applications of finite element limit analysis. In addition to finite element limit analysis, the author's contribution to the development of the innovative new discontinuity layout optimization (DLO) method is also described in this chapter.

Chapter 7- Conclusions and recommendations : In this chapter the main conclusions are drawn together and recommendations for future work are outlined.

Chapter 2

Literature review

2.1 Introduction

It is not clear where and when the construction of arch bridges originated, but archaeologists believe that arches and vaults originated in Egypt and China about five thousand years ago CIRIA (2006). In Europe the establishment of masonry arches as part of the common European cultural heritage is a legacy of the Roman Empire. The development of transport infrastructure for trade, communication and military activities was vital to the administration of the Empire. The Romans made great use of the arch. Figure 2.1 shows one of their largest stone arch bridges, built in 105AD at Alcantra in Spain. It has six arches, up to 30m in span and is probably the oldest stone arch of any significant size outside China still in existence (Page, 1993).

Most Roman arches were semicircular in shape but some were segmental. Most bridges were constructed from cut stone voussoirs, usually without mortar. Regrettably there are no Roman bridges still in existence in the United Kingdom. After the Romans many arch bridges were build in Britain in medieval times, perhaps the most famous being London Bridge, begun in 1176 and completed in 1209. The main period of arch bridge building in the United Kingdom began with the construction of the canals in the second half of the eighteenth century and

FIGURE 2.1: Roman bridge at Alcantara, Spain (built 103-106 AD)(*source from wikipedia*)

ended when the railway network was substantially completed at the beginning of the twentieth century. Very few masonry arch bridges have been built since the first world war. It is estimated that there are about forty thousand masonry arch highway bridges in the UK, and thirty three thousand railway masonry arch spans. Most are modest structures with spans up to about ten metres. There are only a small proportion with spans greater that twenty metres; the longest span in the United Kingdom is the Grosvenor Bridge, Chester, with a span of 61metres.

Bridges built from stone were potentially very solid and durable structures, but relied greatly on the quality of locally available materials and the skill of the masons. Until the end of the Middle Ages, brickwork was seen as inferior to stone for construction. The material used to fill an arch bridge often consisted of whatever was readily to hand, such as the material excavated during the building of the

foundations. It may nevertheless have high strength as a result of its composition and due to consolidation and compaction over the years. Figure 1.1 shows the basic structural elements of a typical masonry arch bridge. The arch spans between two abutments, with backfill providing a transition between the arch and the bridge surface. Spandrel and wing walls retain the fill and carry the parapets. Spandrel walls also stiffen the arch ring at its edges and may sometimes also have a considerable strengthening effect. Many arch bridges have backing at their haunches, with a cemented material to provide extra strength.

2.2 Bridge bearing capacity analysis and assessment methods

There are many different approaches used by industry to assess the load carrying capacity of masonry arch bridges. They range from very simple models such as the MEXE method, BA16 (1997), to sophisticated elasto-plastic finite element models. However, the most frequently used method is probably still the MEXE method - despite the fact that it appears inappropriate and often inaccurate.

Semi-empirical method

The MEXE method is semi-empirical, being originally based on an elastic analysis procedure developed by Pippard et al. (1936), who modelled a linear-elastic parabolic arch barrel, pinned at its supports and carrying a central point load. He made a number of simplifying assumptions and was thus able to formulate tables for the strength of a given bridge based on limiting compressive stress criteria. Assuming a soundly built and maintained parabolic arch with span : rise ratio of $4:1$, the provisional axle load PAL (in kN) is given by:

$$PAL = [740(d + h)^2]/L^{1.3} \text{ or } 70 \text{ whichever is less.} \tag{2.1}$$

in which, L is the span of the arch, d is the thickness of the arch barrel adjacent to the keystone and h is the average depth of fill, at the quarter points of the transverse road profile, between the road surface and the arch barrel at the crown, including road surfacing. This provisional assessment is then modified by empirical factors which allow for deviation of the arch from the above 'benchmark' bridge structure. The method, however, has a number of disadvantages (Hughes & Blackler, 1997):

- The only resisting mechanisms considered are the arch and the weight of the backfill.

- The limiting load criterion is not realistic.

- Inappropriate assumptions are made about the geometry and load location.

- When used by inexperienced engineers, some modifying factors can be dangerously subjective.

- The assessed capacity is widely assumed to be conservative, but in fact can be unsafe.

- The effect of strengthening measures cannot be considered.

Limit analysis (or 'Mechanism') methods

The simplest type of limit analysis procedure applied to arches is commonly referred to as the 'mechanism method'. This is an arguably more rational approach where the arch barrel is assumed to collapse by the formation of a mechanism; the 'mechanism' method has become synonymous with an assumed 4 hinge failure mechanism. Simple equilibrium calculations can be used to evaluate the vehicle load needed to precipitate collapse for a given postulated mechanism geometry. This procedure is repeated with different mechanism geometries until a minimum load is found. The mechanism method has recently been incorporated in modern software applications, obviating the need for the user to manually iterate to find

the worst-case scenario. Currently available examples include a mechanism analysis spreadsheet developed at Cardiff University (Hughes et al. 2002), and Archie-M (2007). Modern forms of the mechanism method (e.g. Crisfield & Packham (1987), Ng & Fairfield (2004)) can also take account the passive resistance when the arch barrel is moving into the fill. The mechanism method is attractive not just because it is more rigorous than the MEXE method but also because formation of a mechanism at failure has been witnessed in many of the full-scale bridge tests carried out on masonry arch bridges (see e.g. Page 1993). However, the assumed contribution of the soil to bridge capacity generally has to be specified in advance and has a semi-empirical basis; extending this simple model, e.g. so as to be able to treat bridges containing reinforced soil would be very challenging.

Limit analysis methods have been developed for masonry arches for many years. Examples are the works of Kooharian (1952), Heyman (1982), Livesley (1978) and Boothby (1994). A limit analysis software package called RING stemmed from research by Gilbert & Melbourne (1994) and this software is now widely used in industry. However, a drawback with this software is that the perceived effect of the soil, rather than the soil itself, is modelled. i.e. this is not a holistic model involving soil and masonry. Recently, Cavicchi & Gambarotta (2005, 2007) have presented an upper, and, more recently, lower bound finite element limit analysis model of the soil-arch interaction problem, which is also considered here. In this model, a holistic model of soil-arch interaction has been used. However, in their upper bound model the masonry was represented using 1D beam elements (rather than using more realistic 2D masonry blocks), and relatively inaccurate constant strain elements were employed in the finite element model of the soil. One objective of this research is to address both these shortcomings, and to also tightly bound the true solution from both above and below. Up until now limit analysis models have generally been two dimensional. Consequently when such models are applied to real, three-dimensional bridges, certain assumptions have to be made about the third dimension. Standard practice to date has been to assume that an applied load will mobilize a fixed width strip of the bridge. However, Harvey et al. (2005); Harvey (2006) have recently questioned this assumption for wide bridges, proposing instead an interesting fan-like distribution model to simulate

the dispersal of an applied load through the arch barrels. Further validation work is recommended before this model can be used in practice.

Finite element analysis methods

The finite element method is a powerful and widely used numerical discretization procedure applied to many practical engineering problems.

Considering conventional elasto-plastic finite element analysis (FEA), there are cases where its limitations are hard to overcome. The analysis of masonry arch bridge using this method is one of them. Drawbacks of using FE analysis include: the input parameters are difficult to determine (e.g. the backfill properties, the masonry strength, the properties of the interface between different structural elements and the initial stress state). Also, as the complexity of the model increases so does the time required to obtain results. Moreover, results from FEA are very much dependent on the accuracy of the assumed material properties, which often are difficult to evaluate by experimental analyses. Several authors have proposed simplified models for the analysis of arch-like structures, e.g. Choo & Gong (1990); Brencich & Francesco (2004); Betti et al. (2008); Drosopoulos et al. (2006). Although simplified, these models still require the assessment of elastic and inelastic parameters, and also involve a potentially fragile non-linear solution procedure. Choo & Gong (1990) developed FEA models for the arch using one dimensional elastic beam elements, which were assumed to have no tensile strength. The horizontal soil pressure are taking into account by fixing horizontal elastic plastic struts to the arch barrel, rather by modeling the backfill directly using elements. Ng et al. (1999) describes analysis of masonry arch bridges using general-purpose FEA software (LUSAS) and reports close agreement between predictions from FEA and the results of the full-scale tests carried out by TRL (Page (1993)). However, a conclusion from this paper was that FEA could model the load deflection behavior extremely well only in cases where the material properties were well known. Unfortunately this is often only the case for bridges where, for research purposes, tests to collapse have been undertaken, with associated material

testing. Thavalingam et al. (2001) compares different computational modelling approaches for masonry arches, including discrete element modelling and non-linear FEA, and concludes that the latter is preferable due to ease of use and ability to obtain converged solutions. Two dimensional models are included in the works of Loo & Yang (1991) Boothby et al. (1998), Owen et al. (1998) Sicilia et al. (2001), Ford et al. (2003), and three dimensional models by Fanning & Boothby (2001). 1D models have proven to be 'efficient' for assessment and design purposes, for both single and multispan bridges, whilst 2D and 3D models may give detailed information on local phenomena at the expense of high computation costs.

2.3 Strengthening techniques for bridges

Various methods have recently been developed for strengthening masonry arch bridges. These vary in effectiveness and each has advantages and disadvantages.

Saddling: casting a concrete saddle on the extrados is a popular method of strengthening arches having low assessed strength. It involves excavation of the fill to expose the extrados of the arch barrel. A reinforced or mass concrete flat or curved slab is subsequently cast in place over the original barrel. The advantage of this method is that the work is invisible but it is expensive and will disrupt traffic flow during construction. Figure 2.2 shows Woolbeding Bridge with the fill excavated prior to installation of a reinforced concrete saddle (Mabon (2002)). Whilst saddling will undoubtedly increase the capacity of the bridge, with minimal change to the external appearance of the bridge, it is expensive and will cause considerable disruption to traffic and buried services which may be located within the fill crossing the bridge.

Sprayed concrete: is widely used as a means of increasing arch ring thickness to increase load capacity. This may be used in conjunction with a reinforcing mesh. Applying sprayed concrete can cause moisture to be locked into the barrel, which can lead to problems in the long term. Another disadvantage of the method is that it reduces headroom under the arch.

FIGURE 2.2: Strengthening Woolbeding Bridge (Mabon 2002)

Use of steel: there are various systems available. For example a network of steel bars can be inserted in slots cut into the intrados and bonded using special adhesives. Such systems have been shown to increase the strength of bridges. Again, these methods will affect the appearance of the intrados.

Anchor: a popular strengthening method is to insert *anchors* through the fill and into the arch barrel. The system works by grouting a deformed stainless steel reinforcing rod into holes drilled into the arch. This adds internal reinforcement to the arch bridge so that it acts as a reinforced unit.

2.4   Load tests on full scale masonry arch bridges, to collapse

Page (1993) reviews various experimental investigations which have been carried out on masonry arch bridges. Thirteen load tests to collapse on full scale bridges

FIGURE 2.3: Typical anchor positions and installation of reinforcement from the road surface (Mabon 2002)

are reported, ten of these being TRL organized tests on redundant bridges and full scale models, and three being undertaken by Davey (1953) before the second world war (numbers 10 to 13 in the table). Brief details of these tests are shown on Table 2.1. Page carried out tests numbered 3 to 8 on the table, and details of these can be found in Page (1987, 1988, 1989). However, at the time these tests were conducted the MEXE method was popular so only data necessary for a MEXE assessment was taken. Many material properties required by more advanced analysis techniques were not made available. Prestwood bridge (number 4 on the table) is the only bridge where reasonably good information on material properties is available. However, the test loading arrangement was not ideal, especially when calibrating an assessment model that takes soil-arch interaction into account (see chapter 4 for more details).

2.5   Theory of plasticity: historical remarks

The history of plasticity dates back to 1864 when Tresca published his yield criterion based on experimental results on punching and extrusion. Since then, tremendous progress has been made by many researchers, such as de Saint-Venant (1870), Von Mises (1928), who have established some of the key foundations on which plasticity theory now rests (Khan & Huang (1995)). Although the work by Tresca on

No	Bridge	Span (m)	Rise (m)	Width (m)	Ring thickness (m)	Depth of fill at crown(m)	Collapse load (kN)
1	Bridgemill	18.3	2.85	8.3	0.711	0.203	3100
2	Bargower	10.0	5.18	8.68	0.558	1.2	5600
3	Preston	5.18	1.64	5.7	0.36	0.38	2100
4	Prestwood	6.55	1.43	3.8	0.34	0.165	228
5	Torksey	6.55	1.43	3.8	0.34	0.246	1080
6	Shinafoot	6.16	1.18	7.02	0.365	0.215	2524
7	Strathmashie	9.42	2.99	5.81	0.6	0.41	1325
8	Barlae	8.53	1.69	9.8	0.45	0.295	2900
9	Dundee	4.0	2.0	6.0	0.25	0.2	1040
10	Bolton	6.0	1.0	6.0	0.22	0.3	1170
11	Croft Breadsall	6.45	2.06	5.41	0.356	0.254	783
12	Yardley Wood	6.5	1.97	4.48	0.343	0.305	1230
13	Alcester Road	6.45	1.93	10.18	0.356	0.305	568

TABLE 2.1: Thirteen full scale bridge tests to destruction

the yield criterion of metal is widely regarded as the starting point of the classical theory of plasticity, fundamental research on the failure or yielding of soils had been carried out much earlier by Coulomb (1773), and applied in practice by Rankine (1857) to solve earth pressure problems involving retaining walls. The first attempt to formulate the stress-strain relationship for plastic deformation was made by de Saint-Venant (1870). He worked on the plane plastic strain problem using Tresca's criterion and assuming zero work hardening. For the first time he proposed that the principal axes of the strain increment coincided the axes of principal stress. The elastic strain ϵ^e was neglected so that the plastic train ϵ^p was equal to the total strain ϵ. The coaxial assumption made by de Saint-Venant proved to be a foundation for the classical theory of plasticity with regard to stress-strain relations. Saint-Venant's idea was extended to the three-dimensional by Von Mises (1913). The basic assumptions of the theory of plasticity can be stated as follows:

- The elastic strain ϵ^e is so small as to be negligible.

- The increment of strain $d\epsilon$, or equivalently the rate $\dot{\epsilon}$, is coaxial with stress.

The general mathematical treatment of the constitutive equation for plastic de-
formation of flow was proposed by Von Mises (1928). He noticed that in elasticity
theory the strain tensor was related to the stress through an elastic potential
function, the complementary strain energy U, such that:

$$\epsilon_{ij} = \frac{\partial U}{\partial \sigma_{ij}} \tag{2.2}$$

By generalizing and applying this idea to plasticity theory, von Mises proposed
that there existed a plastic potential function $Q(\sigma_{ij})$ and the plastic strain rate.

$$\epsilon^p = p\frac{\partial Q(\sigma_{ij})}{\partial \sigma_{ij}} \tag{2.3}$$

Where p is a proportional positive scalar factor. To determine p, the yield criterion
was used.

- Geometrically this equation means that the plastic strain rate vector ϵ^p is
  perpendicular to the surface. Therefore is also referred to as the *normality
  rule* in plasticity theory.

- For an isotropic material, $Q(\sigma_{ij})$ is a function of the invariants of the stress
  tensor.
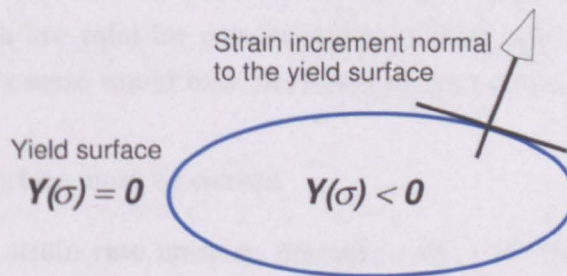
FIGURE 2.4: Yield surface and normality condition

The main purpose of using the plastic potential theory is to determine the plastic
potential . In fact the effective form of the function is an open question. *A common*

approach in plasticity theory is to assume that the plastic potential function $Q(\sigma_{ij})$ is the same as the yield function $Y(\sigma_{ij})$. Then the equation can be rewritten as:

$$Q(\sigma_{ij}) = Y(\sigma_{ij})$$

and the plastic strain rate $\dot{\epsilon}^p$ is normal to the yield surface. This is called the *associated flow rule*. On the other hand, if $Q(\sigma_{ij}) \neq Y(\sigma_{ij})$ the flow rule is called *nonassociated*.

Von Mises (1928) and Hill (1948) proposed the maximum plastic work principle. It states that: If the yield surface is strictly *convex*, the actual work done in a given plastic strain rate is greater than the fictitious work done by an arbitrary state of stress not exceeding the yield limit. In short, the maximum plastic work principle is a mathematical statement of the following two important ideas:

- The yield surface is convex.

- The plastic strain rate is normal to the yield surface.

However, the notations of *normality* and *yield convexity* mentioned above are just mathematical ideas. In an attempt to provide a missing link between material behaviour and these mathematical ideas, Drucker (1952) introduced a fundamental stability postulate. In essence, Drucker's stability postulate is a generalization of simple facts which are valid for certain classes of materials. A material that is stable in Drucker's sense would have the following properties:

- The yield surface must be convex.

- The plastic strain rate must be normal to the yield surface (i.e. have an associated flow rule).

- The rate of strain hardening must be positive or zero (i.e. an additional stress must cause an additional strain).

- The maximum plastic work principle is valid.

2.6 Limit analysis: basic theory

In the theory of elasticity, use has to be made of the stress-strain relations to determine whether given stress and displacement states correspond and a unique solution results. In an elastic-plastic material, however, there is as a rule a three-stage development in a solution (when the applied loads are gradually increased in magnitude from zero). These are namely the initial elastic response stage, the intermediate contained plastic flow stage and finally the unrestricted plastic flow stage. The complete solution by this approach is likely to be cumbersome for even the simplest problems. Therefore, methods are needed to furnish the load carrying capacity in a more direct manner. Limit analysis is a method which enables definite statements to be made about the collapse load (or load multiplier) without recourse to a step-by-step elastic-plastic analysis. Limit analysis considers the stress-strain relationship in an idealized manner as it is illustrates in 2.5;
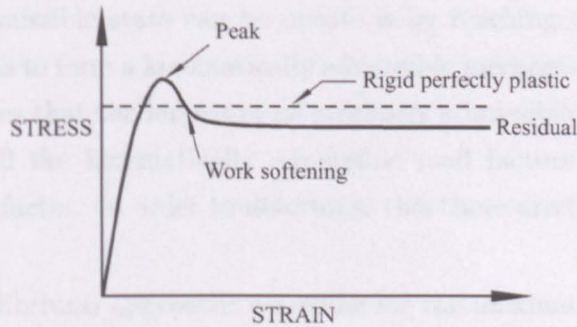
FIGURE 2.5: Stress-strain relationship for ideal and real soils

Assuming a rigid, perfectly-plastic solid subject to a static load distribution, the problem of limit analysis consists of finding the minimum multiple of this load distribution that will cause the body to collapse. In order to mathematically model this type of material, the yield function, Y, is defined in such a way that for $Y < 0$ the material remains rigid, for $Y = 0$, materials become plastic, and for $Y > 0$ the stress state is inadmissible. At the yield surface, material becomes plastic and it is necessary to define the flow direction. The classical limit analysis theory assumed that the flow direction is normal to the yield surface. This hypothesis, also called

normality condition, implies that this type of flow provides greatest resistance against deformation and the energy dissipation by this flow is the maximum.

A structure is said to be in a 'statically admissible state' when the internal stresses are in equilibrium with the external forces and at no point in the structure is the yield condition violated. Assuming that a proportional loading analysis will be performed, it can be stated that if f is the base variable load and λ is the load factor (non-negative), then λf is the load actually applied on the structure. The load factor can be increased from zero up to a limit for the structure to remain safe. The 'exact' load factor is the largest of all possible statically admissible load factors. Another possibility of classical limit analysis is the kinematic (upper-bound) approach. The upper-bound theorem of classical limit analysis states that the 'exact' load factor is the smallest of all possible kinematically admissible load factors. The plastic limit load factor is the same either obtained by the static or kinematic approaches. This means that the only way in which a structure in a statically admissible state can be unsafe is by reaching the yield surface in enough places so as to form a kinematically admissible mechanism. The uniqueness theorem establishes that the largest of all statically admissible load factors equals the smallest of all the kinematically admissible load factors and is the 'exact' plastic limit load factor. In order to determine this there are three possible ways:

- Static (equilibrium) approach: searching for the maximum statically admissible load factor

- Kinematic approach: searching for the minimum kinematically admissible load factor

- By equating the load factors of both formulations determined.

2.7 Computational limit analysis

2.7.1 Introduction

Limit analysis plays a significant role in safety assessment and structural design, especially in civil engineering. Over the past few decades extensive research has been carried out on developing computational limit analysis approaches. Computational limit analysis involves two main aspects: (i) discretination e.g. by finite element (FE) approach and (ii) mathematical programming to solve the formulated optimization problem. For an FE based approach, the former involves breaking the continuum into a finite number of pieces (elements); describing the behavior of each element by some suitable mathematical field equations; and then connecting the elements together at nodes. This results in a set of algebraic equations that represent the behavior of the whole continuum under loading and boundary conditions. For limit analysis, these equations may be static equilibrium or kinematic compatibility equations together with associated relations. Computational limit analysis can be established and modelled as optimization problems, in which a functional is maximized or minimized, subject to sets of equality and inequality constraints. The resulting optimization problems are then solved by user developed or commercial optimization packages.

2.7.2 Mathematical optimization

Mathematical optimization or mathematical programming is an operations research technique designed to solve problems in which an optimal value is sought subject to specified constraints. Mathematical programming models include linear programming (LP) and non-linear programming (NLP). In a optimization problem, one seeks to minimize or maximize a real function of real or integer variables, subject to constraints on the variables. The term mathematical programming

refers to the study of these problems: their mathematical properties, the development and implementation of algorithms to solve these problems, and the application of these algorithms to real world problems. A mathematical optimization problem, or just optimization problem, has the form

$$\text{minimize } f_0(x) \tag{2.4}$$

$$\text{subject to } f_i(x) \leq b_i, \text{i=1},\ldots,\text{m}.$$

Here the vector $x = (x_1,\ldots,x_n)$ contains the optimization variables of the problem, the function f_o is the 'objective' function, the functions f_i with $i = 1,\ldots,m$ are the 'constraint functions', and the constants $b_1,\ldots,b_m$ are the limits, or bounds, for the constraints. A vector x^* is called optimal, or a solution of the problem 2.4, if it has the smallest objective value among all vectors that satisfy the constraints: for any z with $f_1(z) \leq b_1,\ldots,f_m(z) \leq b_m$ we have $f_0(z) \geq f_0(x^*)$. The classes of optimization problem characterized by particular forms of the objective and constraint functions. As an important example, the optimization problem 2.4 is referred to as a 'linear programming' problem if the objective and constraint functions $f_0\ldots,f_m$ are linear, *i.e.* satisfy

$$f_i(\alpha x + \beta y) = \alpha f_i(x) + \beta f_i(y) \tag{2.5}$$

for all $x, y \in \mathbf{R}^n$ and all $\alpha, \beta \in \mathbf{R}$. Conversely if the functions are not linear, the problem is referred to as a 'nonlinear programming' problem.

Figure 2.6 shows an example of a linear programming problem, where f_0 is the objective function, f_{1-5} are the constraints, and the optimum solution will lie inside the shaded area. Short details of mathematical programming can be found in Appendix A. It also provides details of the duality concept of linear optimization, which is valuable for modelling masonry structures, and will be discussed in Chapter 3.

In this thesis, the main mathematical programming technique is linear programming although the optimizer software which will be used (Mosek, 2006) can also
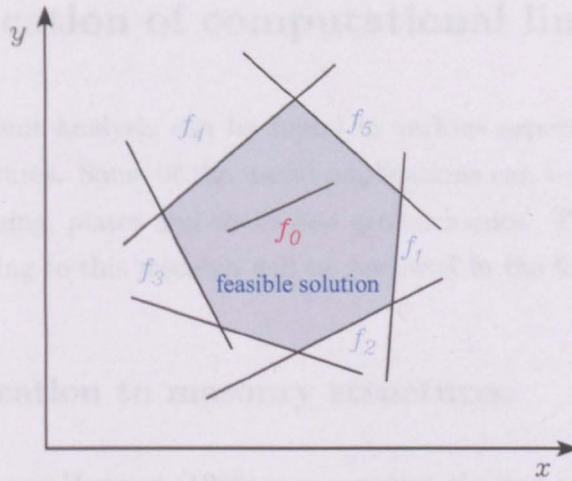
FIGURE 2.6: A linear programming problems with the feasible solution

solve certain non-linear problems. LP has been used in limit analysis for many years since good LP packages were available before the development of NLP. In limit analysis, the use of linear programming requires the use of piecewise linear (PWL) approximation of yield surfaces. Generally, use of PWL yield surfaces can increase the size of the model (increasing the number of constraints and variables). However, this can be moderated by using some type of adaptive procedure. Representative contributions have been made by Anderheggen & Knopfel (1972); Christiansen (1991); Andersen & Christiansen (1995); Krabbenhoft & Damkilde (2003); Lyamin & Sloan (2002a). In most cases, the yield functions are nonlinear (except some special cases such as Tresca yield condition in the principal stress space), and hence a NLP problem is arrived at when a limit analysis model is formulated. Many authors have been using NLP in their model, representative works have been made by Casciaro & Cascini (1982); Ciria & Peraire (2004); Makrodimopoulos & Martin (2005); Andersen et al. (1998); Zouain & Herskovits (1993); Christiansen & Andersen (1999); Martin & Makrodimopoulos (2008). However, there exists a trade-off between the speed of LP with PWL yield surfaces and NLP with original nonlinear yield surfaces in limit analysis.

2.8 Application of computational limit analysis

Applications of limit analysis can be found in various aspects of practical civil engineering structures. Some of the useful applications can be found in the analysis of metal forming, plates and shells and geomechanics. There are two useful applications relating to this research will be reviewed in the following sections.

2.8.1 Application to masonry structures

Kooharian (1952) and Heyman (1966) were amongst the first to consider (vaulted) masonry block structures in the context of the plastic limit analysis theorems which emerged during the preceding century. Their model was based on three key assumptions:

- *Sliding failure cannot occur*

- *Masonry has no tensile strength*

- *Masonry has an infinite compressive strength*

It may be argued that masonry is brittle and therefore cannot deform plastically. However, it is perfectly possible to create a ductile structure from a brittle material. The plastic behaviour of the arch is well explained Harvey (2006) as below.

"Considering an arch is subjected to a sufficiently large concentrated live load, it will crack. Typically, there will be an initial crack near the crown of the arch which is often too small to be visible. In that circumstance, the crack will migrate from the crown towards the load and only become visible as the load increases further. Once the hinge has reached the load point, the rotation there will grow with increasing load, but without substantial change of geometry of the structure. The eccentricity of the thrust at that point reaches a limit and the effective moment in the arch, the eccentricity of the thrust times its value, becomes stable. Cracks begin to form elsewhere and migrate towards stable positions. Each hinge rotates

freely at a constant moment until a fourth hinge forms and the structure becomes a mechanism. This is classic plastic behavior."

The importance of these assumptions is that they enable the bounding theorems of plasticity to be directly applied to the determination of a collapse load for a masonry arch and vault.
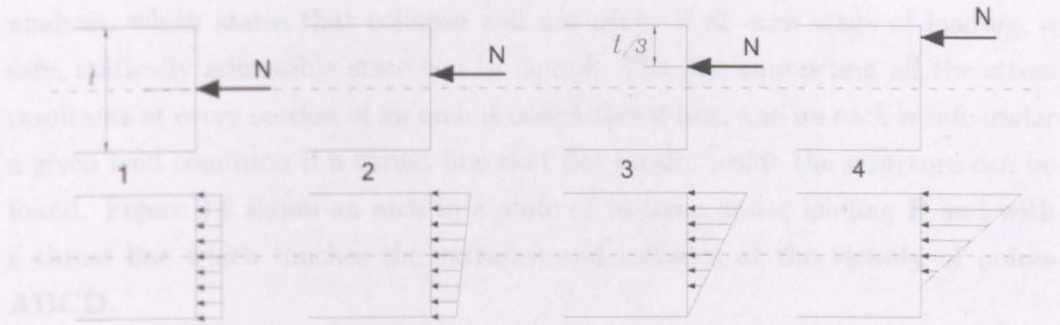
FIGURE 2.7: Normal force acting at various position across a masonry cross-section

In order to realize the consequences of this hypothesis, consider a cross-section of an arch-like structure in two dimensions as in figure 2.7. Since shear failure is avoided, only the normal components of the stresses are considered. The resultant of these stresses must be a compressive force and must act inside the cross section since otherwise tensile stresses would be generated. Any of the first three positions of **N** shown on the figure can be considered to be safe. When **N** acts at position 3, a limiting condition is reached by the stress distribution. If **N** acts beyond this point, as in position 4, there theoretically would be tensile stresses set up in an area of the voussoir. However, since the joint is assumed not to be able to transmit tensile stresses, the traditional conservative rule that requires the normal force to remain within the middle third is breached (see Heyman (1982)). However, if the normal force acts beyond position 3 and still lies within the voussoir, the maonry arch will not collapse. This conclusion is supported by Pippard & Chitty (1952) after series of careful experiments on the analysis and design of a voussoir arch. As the normal force resultant approaches the edge of the section, a large stress concentration appears and crushing or spalling is likely to occur. But because of

the infinite compressive strength assumption, the resultant is allowed to reach the very edge. At this stage, the section is fully cracked and free to rotate around the edge, i.e. a hinge can form at this point. Extending this idea further for every section within an arch leads to the conclusion that if a stress state can be found where every section is safe and the external and internal forces are in equilibrium, then the structure is itself in a safe state. This matches the first theorem of limit analysis, which states that collapse will not occur if at each stage of loading, a safe, statically admissible state can be found. The line connecting all the stress resultants at every section of an arch is called *thrust line*, and an arch is safe under a given load condition if a thrust line that lies totally inside the structure can be found. Figure 2.8 shows an arch in a state of collapse under loading **P** and with a thrust line which touches the extrados and intrados at the vicinity of points **ABCD**.
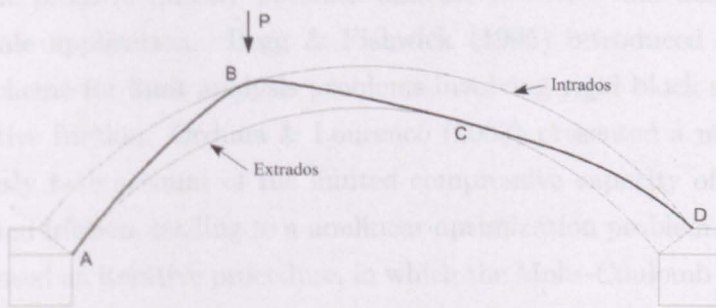
FIGURE 2.8: An arch in the state of collapse

The pioneer of using modern computational methods to determine the collapse load of masonry gravity structures was Livesley (1978), who posed a lower bound formulation which could be solved using linear programming. In this formulation the problem involves maximization of the collapse load factor, subject to equilibrium and yield constraints. In his paper, Livesley shows that the adoption of associative friction leads to an incorrect collapse mechanism. More importantly it may also give an overestimate of the true collapse load. When using linear programming to solve limit analysis problems, flow will always occur normal to the specified surface (i.e. according to the so-called 'normality rule'). It should

perhaps be mentioned that for certain classes of problems the assumption of associative friction has been found to provide numerical predictions which are in broad agreement with experimentally observed results. For example, in a study of the behaviour of multi-ring arches Melbourne & Gilbert (1995) observed that associative friction solutions appeared to agree reasonably well with experimental results.

Following Heyman and Livesley's works, a number of related investigations have been carried out. Boothby (1994) considered the failure between blocks at the contact interface, both sliding and hinging. Several attempts have been made to solve the non-associative flow problem recently, for example: Ferris & Tinloi (2001) demonstrated the use of Mixed Complementary Programming (MPC) and Mathematical Program with Equilibrium Constraints (MPEC) algorithms. However, the problem quickly becomes difficult to solve, and hence unsuitable for large scale application. Begg & Fishwick (1995) introduced an automatic numerical scheme for limit analysis problems involving rigid block structures and non-associative friction. Orduna & Lourenco (2003) presented a model that can simultaneously take account of the limited compressive capacity of masonry and non-associated friction, leading to a nonlinear optimization problem. Gilbert et al. (2006) proposed an iterative procedure, in which the Mohr-Coulomb failure surface is updated at each iteration until a converged solution is obtained. However, in spite of much research, the challenge of reliably computing the collapse load of problems involving non-associative function remains.

2.8.2 Application in geomechanics

It is well known that limit analysis is a powerful tool for analyzing the stability of problems in soil mechanics. The plastic limit theorem of Drucker (1954) can conveniently be employed to obtain upper and lower bounds on the collapse load for a number of geomechanics problems. The theory assumes a perfectly plastic soil model with an associated flow rule and states that any statically admissible stress fields will correspond to a lower bound on the true limit load. However, it

is often difficult to apply the theorem to practical problems involving complicated loading and geometry. An alternative method of computing lower bounds, which uses finite elements and linear programming was originally presented by Lysmer (1970). Lysmer proposed a technique for computing lower bound limit loads in soil mechanics involving discretizing the soil mass into a number of 3-noded triangular elements. The nodal variables were the unknowns and statically admissible stresses were allowed to occur at the shared edge between adjacent triangles. In contrast to standard finite element formulations, each node was unique to a particular element and more than one node could share the same co-ordinates.

Application of boundary conditions, equilibrium equation and yield criterion leads to an expression for the collapse load which is maximized subject to a set of constraints on the stresses. In order to avoid nonlinear constraints occurring in the constraint matrix, the yield criterion must be expressed as a linear function of the unknown stresses. For the Tresca and Mohr-Coulomb yield criteria, this is achieved by employing a polygonal approximation of the yield surface.

The advantage of numerical formulations are that complex loading patterns and geometries can be dealt with. Moreover, inhomogeneous soil properties can be modelled. However, a major drawback is the large amount of computer time potentially required to solve the resulting linear programming problem. This is because the linearized yield criterion typically generates a very large number of inequality constraints on the nodal stresses. Lysmer attempted to overcome this problem by employing an iterative technique which used a small subset of the total number of yield constraints. Although this approach reduced the computational effort significantly it was found, in some cases, to be unstable. This is because the method assumed that the path followed by each nodal stress during the optimization process would be relatively localized. If this is not the case, then the linear programming problem may become unbounded. Some of the most active researchers in this field over the past two decades have been Sloan and his collaborators at the University of Newcastle, Australia: Sloan (1988, 1989); Sloan & Kleeman (1995); Yu et al. (1994); Merifield et al. (2001). Linear programming and, more recently, non-linear programming upper and lower bound formulations

have been considered, Lyamin & Sloan (2002a,b). In Sloan (1989), an upper bound model using constant strain triangles is applied to geotechnical problems. However the mesh has to be arranged in a specific manner to avoid volumetric locking problems. In order to overcome this, Yu et al. (1994) used linear strain triangles with straight sides and mid-side nodes. However, in this paper, the shearing direction between elements has to be specified in advance; Sloan & Kleeman (1995) proposed a new formulation to overcome this. Solutions for bearing capacity problems involving respectively two-layer clay and sand over clay are provided by Merifield et al. (1999); Shiau et al. (2003). The solutions compare well with existing elasto-plastic analysis solutions. With the use of numerical limit analysis, Ukritchon & Klangvijit (2003) computed values for the bearing capacity factor N_γ, finding good agreement with existing results. Chen et al. (2004) used FELA to assess slope problems involving pore water pressure. With the use of the interior point optimization method, Pastor et al. (2003) investigated the maximum height of a vertical slope ('cut') problem. For soil with cohesion c, the given solution for $\gamma h/c$ was found to be between 3.767 and 3.782. The bearing capacity of various types of footings in sand in 3D have recently been investigated by Lyamin et al. (2007), who obtained solutions which compared well with others in the literature. However, it should be noted that the mesh was carefully refined, making use of specific element arrangements to avoid locking. Loukidis et al. (2003) investigated the use of FELA to assess the stability of slopes subjected to seismic loading, concluding that FELA is a versatile tool for the determination of rigorous lower and upper bounds on acceleration which will trigger failure. Other investigators who have studied the computation of lower bound limit loads by finite elements and linear programming include Anderheggen & Knopfel (1972), Bottero et al. (1980). Notable more recent work has also been undertaken by Andersen et al. (1998), who showed that a limit analysis problem which has a quadratic yield function can be reduced to the problem of minimizing a sum of Euclidean vector norms. Recent developments in mathematical programming allows the Mohr-Coulomb constraints to be tackled directly. In a similar manner Makrodimopoulos & Martin (2005)applied the technique of Second Order Cone Programming (SCOP) to limit analysis problems. However, the application of this method is restricted to yield functions

that can be expressed in a conic form.

Casciaro & Cascini (1982); Capsoni & Corradi (1997) proposed a 'mixed' finite element model. The solution obtained is neither a true lower-bound nor a true upper-bound on the collapse load. Recently, a new numerical procedure for lower-bound limit analysis was presented by Chen et al. (2008). In the paper, a self-equilibrium stress basis vector at each Gaussian point is computed using the element-free Galerkin (EFG) method. Although this does not guarantee a strict lower-bound, a reliable estimate of the limit load factor can be obtained when the discretisation is sufficiently fine. At the same time, the EFG method has been used to obtain upper bounds on the limit loads of plates by Canh et al. (2008). The upper and lower bound solutions obtained by this approach are promising. Although, the EFG method has been applied successfully to obtain highly accurate solutions for problems involving stress discontinuities and/or for problems prone to volumetric locking when using finite element method (Belytschko et al. (1994); Dolbow & Belytschko (1999); Askes et al. (1999)), both Chen et al. and Canh et al. have not yet applied this new approach to problems involving strong singularities and locking in 2D-plane strain or 3D.

During the course of this research, a novel computational limit analysis method has been developed by Smith & Gilbert (2007). This method overcomes both the volumetric locking and stress/velocity singularity problems associated with finite element limit analysis. The method is called *Discontinuity Layout Optimization* (DLO) and involves determining the critical layout of discontinuities, and associated upper-bound limit load, for plane plasticity problems. This method has already been developed into a commercial software application for geotechnical applications.

2.8.3 Computational mechanics issues

Many investigations have been carried out to provide more robust and efficient procedures to solve practical engineering problems. There are two well-known issues involve FE discretization and these will be discussed below.

Locking in the fully plastic range

The so-called 'locking' problem was first pointed out by Nagtegaal et al. (1974). This results from the excessive number of kinematic constraints imposed on an incremental displacement field as collapse is approached. This may make certain plane strain and three dimensional limit analysis problems impossible to solve. This problem stems from the fact that the deformed state of an elastic-perfectly plastic material is highly constrained at the limit load; with a standard material idealization, deformation increments at the limit load will be strictly incompressible. In a standard finite element formulation, posed in terms of kinematically admissible displacement fields, the same condition will have to be satisfied. Many methods have been proposed to overcome this problem. These include: the use of higher order elements (Sloan & Randolph, 1982); the use of a mesh of crossed linear triangular elements (Nagtegaal et al., 1974). The most robust and effective method is to use higher order elements; however this leads to increased problem size. Recently, Tin-Loi & Ngo (2003) demonstrated that the locking problem can be overcome by using p-version finite elements. In contrast to a model involving traditional h-version elements, where solution errors are reduced by refining the mesh size, in a model involving p-version elements the error is reduced by increasing the degree p of the polynomials used. Interestingly Tin-Loi & Ngo (2003) expected that this work could potentially be applied to 3D problems (as such problems are very difficult to solve (Sloan & Randolph, 1982)). However, all provided examples involve plane strain problems. In terms of FEA analysis, various methods have been developed to overcome this issue. For instance the reduced-integration method Zienkiewicz et al. (1971, 1976) has been used to circumvent the problem of incompressibility constraints in finite element schemes. The idea of this technique is to use a limiting number of sampling points in evaluating the element matrices and load vectors. One major effect of this method is to decrease the number of incompressibility constraints on the nodal velocities. Yu et al. (1991) proposed a new displacement interpolation function for a six-noded triangular element to overcome locking in axisymmetric problems.

Adaptive mesh refinement

Mesh dependency is a well known problem which affects the finite element method. Various adaptive mesh refinement strategies have been developed over the years to overcome this issue. In soil mechanics problem, the role of discontinuities between elements can be crucial since their arrangement and distribution has a dramatic influence on the accuracy of the lower bound solution (Chen, 1975). In the lower bound analysis this restriction means that the geometry of the mesh needs to be refined in a specific manner (i.e. it is not sufficient simply to reduce the size of elements). Thus an adapted mesh might have a maximum density of discontinuities in the direction of the maximum rate of change in the stress field. Work by Peraire et al. (1987) and Borges (2001) has provided solutions which address this restriction. Following the work of Peraire, the creation of fan-like zones in the region of singularity points can be generated automatically in the re-meshing procedure. However the origin of the singularity, the density of the element fan and the distance that the fan will extend must be specified. Borges presented an anisotropic mesh adaptation strategy for a mixed limit analysis formulation which focused on the use of a directional error estimator. Combining these works, Lyamin et al. (2005) constructed a number of suitable adaptive meshes for various geomechanics problem (e.g. rigid strip footing and vertical cut problems). Christiansen & Pedersen (2001) proposed a technique based on the deformations and the slack in the yield condition to obtain improved results for classical limit analysis problems. using their technique, elements should not be refined if they are not close to yield (lower-bound) or if they have a zero strain tensor.

2.9 Structural layout optimization

2.9.1 Introduction

Conventional design procedures aim to identify an acceptable or adequate design which merely satisfies the functional and other requirements of the problem. In general there will be more than one acceptable design. The purpose of design

synthesis, or optimization, is therefore to choose the best one of the many accept-
able designs available. To allow this to happen a criterion has to be chosen for
comparing the different alternative acceptable designs and for selecting the best
one. This criterion, when expressed as a function of the design variables, is known
as the objective function and its choice is governed by the nature of problem. In
structural design, the objective function is usually taken as the minimization of
cost, often represented by the minimization of material volume, with the variables
being element forces. The restrictions that must be satisfied to produce an accept-
able design are collectively called design constraints. Optimization may therefore
be defined as:

*the process of generating a structural arrangement that achieves the most desirable
value of a given characteristic objective function by altering one or more design
variables, whilst complying with a given set of geometrical and/or behavioral limi-
tations constraints.*

Sigmund (2000) conducted a comprehensive review on the different forms that
structural design optimization problems can take and his findings are summarized
below:

Sizing optimization : Involves the optimal sizing of members within a structure
of fixed geometry and topology. In a sizing optimization problem, the layout
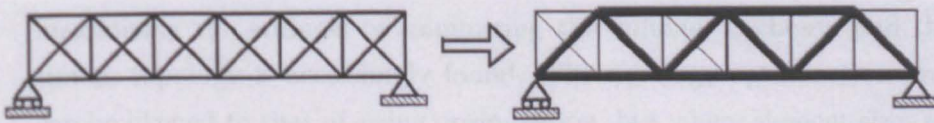
FIGURE 2.9: Sizing optimization of a truss structure (Sigmund 2000)

of the structure is prescribed. Figure 2.9 shows a truss structure optimized
by modifying the cross-sectional areas of the individual elements, such that
the stiffness of the truss structure is maximized for a given total weight.

Shape optimization : Involves the optimal sizing and geometry of a known
structural layout by selectively reducing material density in areas of low
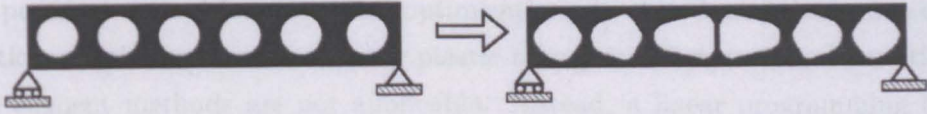
stress (and possibly also increasing it in areas of high stress). Figure 2.10 shows a beam containing holes to reduce its self-weight; however, if the holes are made too big, the structure may be unsafe when subjected to load. Using *shape optimization*, the structure is modified such that it just carries the load using the lowest amount of material possible.

Topology optimization : Involves determination of the optimal layout of a structure. With topological optimization, the general form of the structure
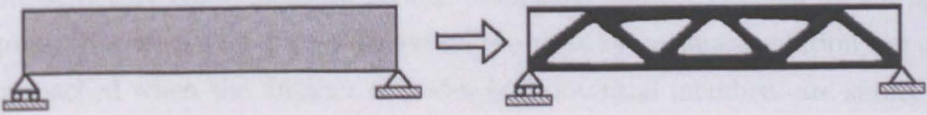
FIGURE 2.11: Topology optimization of a beam for maximum stiffness (Sigmund 2000)

is unknown before the optimization takes place. In the simplest of problems, the only prescribed aspects of the structure are the loading conditions, support position and material properties. The objective function, such as maximizing the stiffness or minimizing the volume, is chosen and the optimum topology is accordingly found. The topology optimization problem can be likened to that of sizing optimization, but where element sizes can be reduced to zero.

2.9.2 Layout optimization of gridlike structures

In his paper, Sigmund (2000) presented a number of optimization examples using an elastic Finite Element Analysis (FEA) approach. However, FEA is not the

only popular method for structural optimization. In this thesis, the layout optimization of gridlike structures using plastic theory is of interest, and traditional finite element methods are not applicable. Instead, a linear programming (LP) technique is adopted.

The structural layout problem was originally cast as a (linear) mathematical programming algorithm in the 1960's by Dorn et al. (1964) and Hemp & Chan (1966), probably as a direct result of the availability of the Simplex optimization technique, pioneered by Dantzig (1963). In these, the problem is posed as a having 'ground-structure', where the domain is filled with a finite number of nodes coincide with the positions of supports, points loads and structural joints. A set of potential members connecting all the nodes to each other and the optimum layout is some subset of these, which the optimization looks to identify.

Ground-structure based methods produce solutions that are optimal for the specified group of potential members. However, the globally optimum solution can often be approached when the number of nodes and potential members are sufficiently fine.
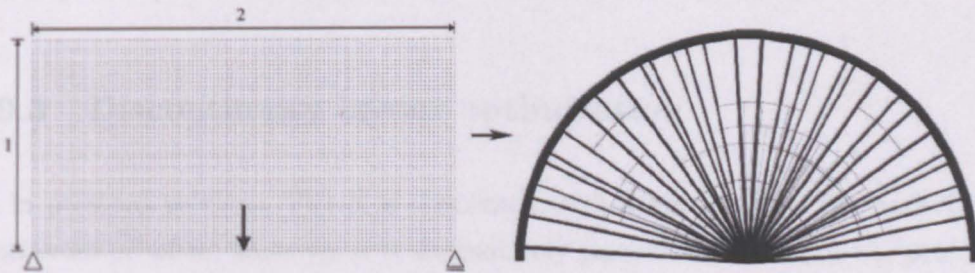
FIGURE 2.12: Example of a layout optimization problem (Gilbert & Tyas 2003)

One of the challenges with the ground structure approach lies in the fact that a large number of potential members are often required and finding the optimum subset of these can be computationally expensive. For a structure that has n nodes, the number of potential members will be $n(n-1)/2$. Thus, for example, an apparently modest 40×40 node problem with a fully connected ground structure includes 1600 nodes and over one million potential members, which equates to several thousand LP constraints and well over 2 million LP problem variables. To

overcome this issue, it would seem sensible to start with a smaller structure and subsequently adding new potential members. However, a comprehensive review by Topping (1984) pointed out that there 'were no rigorous methods of introducing new members during optimization procedure'. Subsequently, Rozvany et al. (1995) indicated that 'no simple methods are available at present for finding the optimal position of additional members'. Thankfully, Gilbert & Tyas (2003) proved that this issue can overcome by starting with a reduced ground structure, where not all potential members are present, then adaptively adding selected members by checking against a criterion associated to their virtual strain. This procedure can be used to tackle problems with several billions of potential members. More details and applications of the method, normally referred to as the *member adding technique*, can be found in Pritchard (2004).

Another challenge with the layout optimization is the stability problem of resulting optimum structures. Figure 2.12 shows an optimum structure that contains many slender compression members, which would be at risk of buckling if constructed. Inclusion of buckling behavior would result in a non-linear optimization problem and at present, there is no efficient method to overcome this issue.

2.9.3 Discontinuity layout optimization

As in previous sections, FELA is concerned with approximating the underlying *continuum* problem. However it is alternatively possible to formulate the problem in terms of the *discontinua* which forms at collapse. Previous workers (e.g. Alwis (2000)) have had only moderate success with this approach, finding that solutions were governed by the initial mesh of rigid elements defined. In fact a successful discontinuous limit analysis procedure must be able to identify the critical arrangement of discontinuities in a problem from a wide, preferably near infinite, number of possibilities. The problem is thus became similar to the problem of identifying the optimum layout of gridlike structures. The DLO procedure was first introduced by Smith & Gilbert (2007) following identification of the similarity between layout optimization of gridlike structure with finding of slip-lines in

(a) Truss layout problem: loading & supports, ground
structure and locations of pre-existing bars (at $y = 4$)

(b) Optimal layout of truss bars for problem (a)

(c) Discontinuity layout problem: imposed displacement
conditions and optimal layout of slip-lines, i.e. as (b)

(d) Truss problem fully analogous to (c)
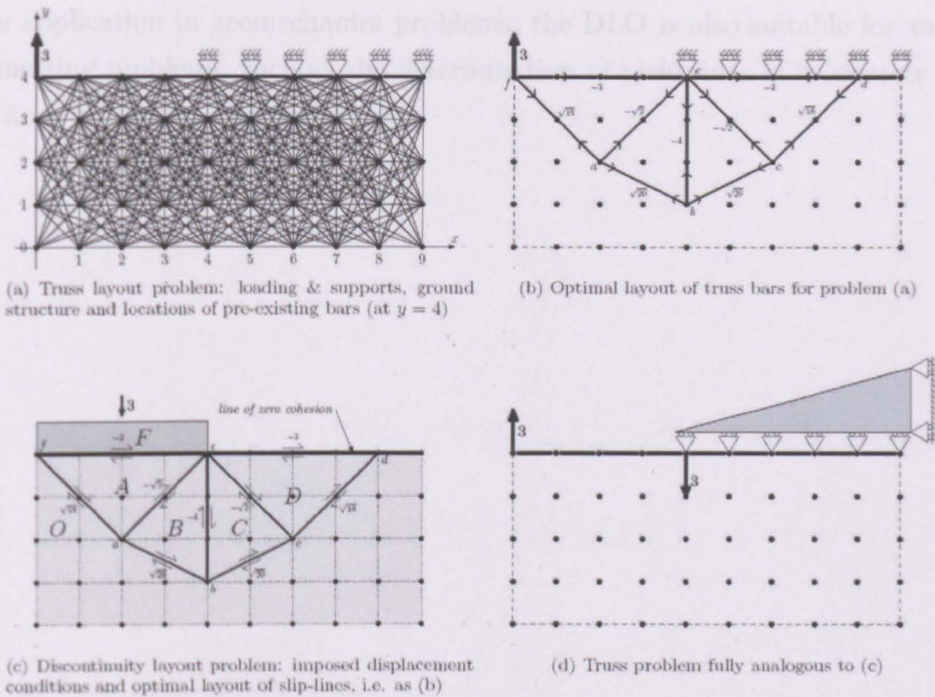
FIGURE 2.13: Analogy between truss and discontinuity layout optimization
(Smith & Gilbert 2007)

a plastic plane-strain problem. Figure 2.13 shows the similarity of a truss layout
optimization with a strip footing bearing capacity problem in geomechanics. Re-
sulting optimum bars are perfectly matched with slip lines of a strip footing. A
DLO problem is formulated in terms of potential discontinuities (lines) intercon-
necting nodes laid out across the body under consideration, rather than in terms
of (solid) elements. This means that discontinuities can be allowed to freely cross-
over one another, considerably increasing the search space and hence the ability
of the procedure to identify complex failure mechanisms. Benefits of this are that
singularities are identified without difficulty (ensuring that high accuracy upper
bound solutions are obtained) and, as failure mechanisms are explicitly identified,
output is easy to interpret as in figure 2.13. It should be noted that the DLO
would not be so successful without the *member adding technique* described in the
previous section. Perhaps, the DLO is even more useful in engineering practical
point of view compared to the layout optimization of gridlike structures. Apart

from application in geomechanics problems, the DLO is also suitable for various engineering problems, such as the determination of yield lines in a concrete slab, slip lines in a metal forming process.

Chapter 3

Numerical limit analysis model of masonry-soil interaction

3.1 Preface

In this chapter, a numerical limit analysis which can subsequently be applied to masonry arch bridge structures is presented in detail. Solutions obtained from the soil model developed are also validated against benchmark literature solutions. Furthermore, in this chapter a mathematical formulation which can be applied to the layout optimization of grid-like structures is established.

3.2 Model of masonry elements

The low tensile strength of masonry makes it prone to crack at or prior to failure. Masonry joints are planes of weakness, and cracks are often focussed here. This means that at the limit state a masonry structure can be considered as an assemblage of clearly defined blocks, with rocking or sliding at cracked joints lying between them. In a rigid-perfectly plastic model, this means that there are displacement (or 'velocity') jumps located at cracks whilst the masonry between them

remains rigid. This section deals with general limit analysis formulations, useful for any rigid block assemblage, in contrast to those applicable only for arch-like structures or specially simplified to make hand calculations easier. These formulations are also suitable for computer implementation. As the specific bonding pattern of masonry structures often influences the failure mode and load factor, so there is certainly some justification for modelling masonry structures as assemblages of discrete blocks. The limit analysis formulation for a rigid block assemblage presented here assumes Heyman's hypotheses, but sliding failures are also allowed. The constituent masonry blocks are assumed to be rigid, with failure (hinging and/or sliding) occurring only in the joints between units; no tension may be transmitted across interfaces.
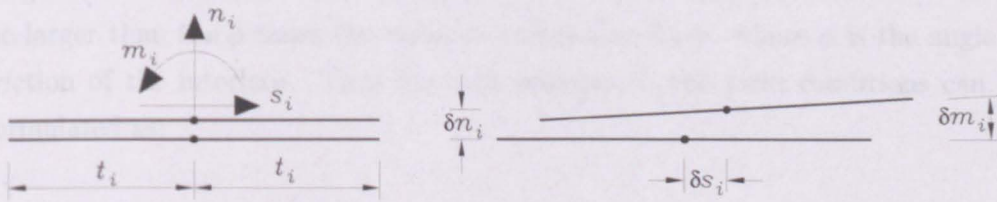
FIGURE 3.1: Block interface
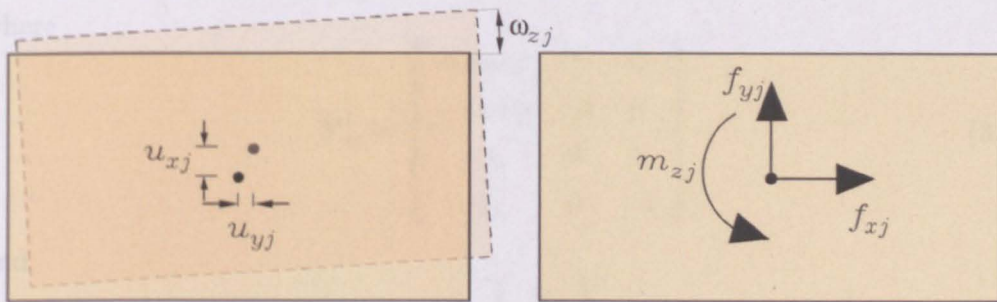
FIGURE 3.2: Block degrees of freedom and loads

Figure 3.1 shows the stress resultants or forces acting at an interface i; these are the normal force n_i, the shear force s_i and the moment m_i, all acting at the centroid of the interface. The corresponding displacement jumps are the relative normal displacement δn_i, tangential displacement δs_i and angular displacement δm_i at the interface center. Each block as shown on figure 3.2 has three degrees of

freedom, namely u_{xj}. u_{yj} and ω_{zj}, which are the displacements in the x, y direction and the angular rotation of the block respectively. Similarly, the external loads applied at the centroid of block are denoted f_{xj}, f_{yj} and m_{zj}.

Yield condition

The yield condition is imposed on every interface where there is contact between adjacent blocks. The relevant yield conditions correspond to: (i) hinging and (ii) sliding failure modes. The hinging condition can be enforced by ensuring that the eccentricity of the normal force at interface i cannot be greater than half the length t_i of the interface. The sliding condition requires that the shear force cannot be larger than $\tan \phi$ times the normal compressive force, where ϕ is the angle of friction of the interface. Thus for each interface i, the yield conditions can be formulated as:

$$\mathbf{Y}_m^i \mathbf{q}_m^i \leq \mathbf{0} \tag{3.1}$$

where

$$\mathbf{Y}_m^i = \begin{bmatrix} -\tan \phi & 1 & 0 \\ -\tan \phi & -1 & 0 \\ -t_i & 0 & 1 \\ -t_i & 0 & -1 \end{bmatrix} \tag{3.2}$$

and

$$\mathbf{q}_m^i = \left\{ \begin{array}{c} n_i \\ s_i \\ m_i \end{array} \right\} \tag{3.3}$$
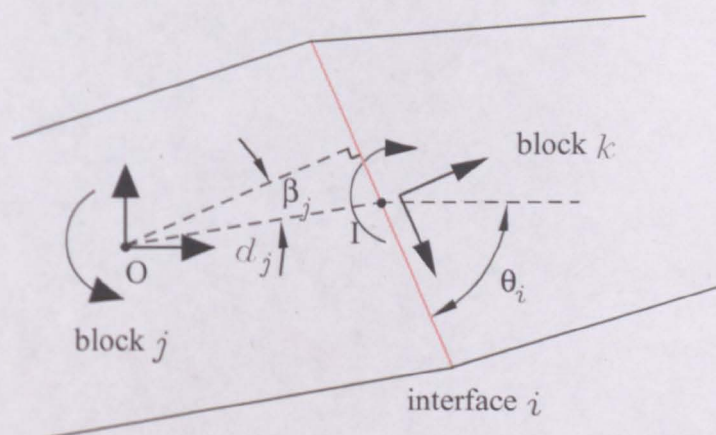
FIGURE 3.3: Block and interface equilibrium

Equilibrium formulation

The necessary equilibrium conditions can be established by formulating free-body relationships for each block. Thus as shown on figure 3.3, the equilibrium relationship for block j can be formulated as:

$$\mathbf{E}_m^i \mathbf{q}_m^i = \mathbf{f}_m^i = \mathbf{f}_{mD}^i + \lambda \mathbf{f}_{mL}^i \tag{3.4}$$

or

$$\mathbf{E}_m^i \mathbf{q}_m^i - \lambda \mathbf{f}_{mL}^i = \mathbf{f}_{mD}^i \tag{3.5}$$

where

$$\mathbf{E}_m^i = \begin{bmatrix} \sin\theta_i & \cos\theta_i & 0 \\ \cos\theta_i & -\sin\theta_i & 0 \\ -d_j\sin\beta_j & d_j\cos\beta_j & 1 \end{bmatrix} \tag{3.6}$$

and

$$\mathbf{f}_m^i = \left\{ \begin{array}{c} f_{xj} \\ f_{yj} \\ m_{zj} \end{array} \right\} \tag{3.7}$$

where d_i is the distance from block centroid $\mathbf{O}$ to mid-point $\mathbf{I}$ of interface i, θ_i is the interface angle made to the x-axis, and β_j is defined as shown on figure 3.3.

$\mathbf{f}_{mL}$, $\mathbf{f}_{mD}$ are the external live and dead loads respectively..

Flow rule and compatibility conditions
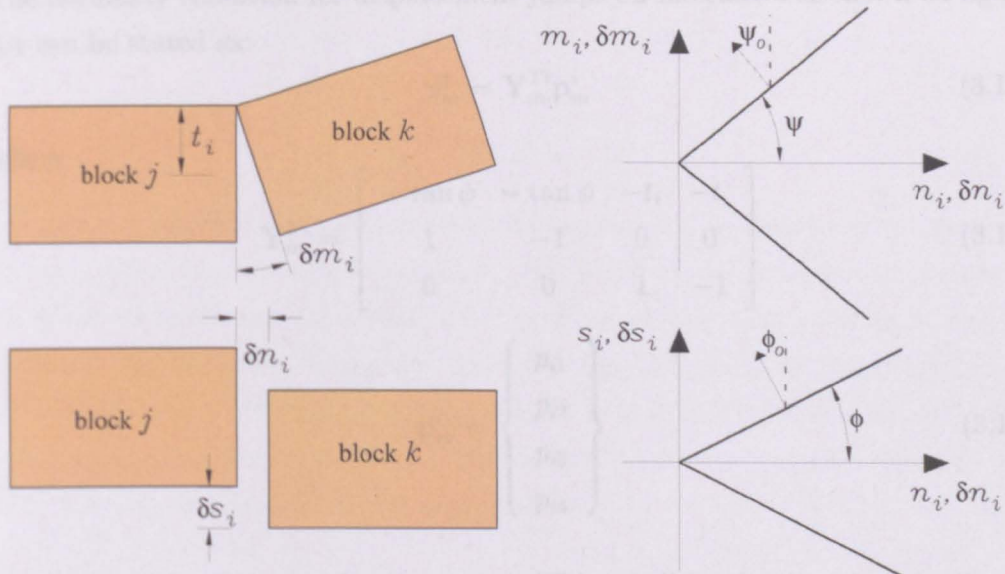
FIGURE 3.4: Failure modes and yield conditions

The displacement jump at interface i produced by the displacements of block j is expressed in equation 3.8, whilst equation 3.11 defines the compatibility matrix $\mathbf{E}_m^{Ti}$ for interface i and block j.

$$\delta_m^i = \mathbf{E}_m^{Ti}\mathbf{u}_m^j \tag{3.8}$$

where

$$\delta_m^i = \left\{ \begin{array}{c} \delta n_i \\ \delta s_i \\ \delta m_i \end{array} \right\} \tag{3.9}$$

$$\mathbf{u}_m^j = \left\{ \begin{array}{c} u_{xj} \\ u_{yj} \\ \omega_{zj} \end{array} \right\} \tag{3.10}$$

$$\mathbf{E}_m^{Ti} = \begin{bmatrix} \sin\theta_i & \cos\theta_i & -d_j\sin\beta_j \\ \cos\theta_i & -\sin\theta_i & d_j\cos\beta_j \\ 0 & 0 & 1 \end{bmatrix} \tag{3.11}$$

The normality condition for displacement jumps on interface i as shown on figure 3.4 can be stated as:

$$\delta_m^i = \mathbf{Y}_m^{Ti}\mathbf{p}_m^i \tag{3.12}$$

where

$$\mathbf{Y}_m^{Ti} = \begin{bmatrix} -\tan\phi & -\tan\phi & -t_i & -t_i \\ 1 & -1 & 0 & 0 \\ 0 & 0 & 1 & -1 \end{bmatrix} \tag{3.13}$$

$$\mathbf{p}_m^i = \begin{Bmatrix} p_{i1} \\ p_{i2} \\ p_{i3} \\ p_{i4} \end{Bmatrix} \tag{3.14}$$

where $\mathbf{p}_m^i$ is the plastic multiplier vector. This condition implies the adoption of an associated material so that $\phi_o = \phi$ and $\psi_o = \psi$. Substituting equation 3.8 into equation 3.12, leads to the following associated flow rule condition for interface i:

$$\mathbf{E}_m^{Ti}\mathbf{u}_m^j - \mathbf{Y}_m^{Ti}\mathbf{p}_m^i = 0 \tag{3.15}$$

Mathematical programming formulations

With the basic relationships already established, it is possible to formulate the limit analysis problem for problems involving assemblages of rigid blocks separated by frictional interfaces. This is achieved by simply imposing all necessary conditions (static equilibrium, kinematic, constitutive relations, and positivity of dissipated work) that describe the collapse of such systems. Thus, from the relations developed in the previous section, after some rearrangement, the following

relationship can be established:

$$
\begin{bmatrix} \cdot & \cdot & \dot{\mathbf{f}}_{mL}^T & \cdot \\ \cdot & \mathbf{E}_m^T & -\mathbf{Y}_m^T \\ -\mathbf{f}_{mL} & \mathbf{E}_m & \cdot & \cdot \\ \cdot & \mathbf{Y}_m & \cdot & \cdot \end{bmatrix} \left\{ \begin{matrix} \lambda \\ \mathbf{q}_m \\ \mathbf{u}_m \\ \mathbf{p}_m \end{matrix} \right\} - \left\{ \begin{matrix} \cdot \\ \cdot \\ \cdot \\ -\mathbf{s} \end{matrix} \right\} = \begin{bmatrix} 1 \\ 0 \\ \mathbf{f}_{mD} \\ 0 \end{bmatrix} \quad (3.16)
$$

and

$$
\mathbf{p}_m \geq 0 \text{ and } \mathbf{s} \geq 0 \quad (3.17)
$$

in which $\mathbf{s}$ is a vector of slack variables that can be used to transform the inequality constraints into equality constraints. When the above static equilibrium and kinematic variables are uncoupled, a LP problem can be recognized as being the necessary and sufficient optimality Karush-Kuhn-Tucker conditions of a pair of dual LP problems with unique optimal values of a λ. Mechanically, the LPs are well-known expressions of the bound theorems of plasticity. The LP related to the static theorem is given by the following section.

3.2.1 Static (equilibrium) formulation
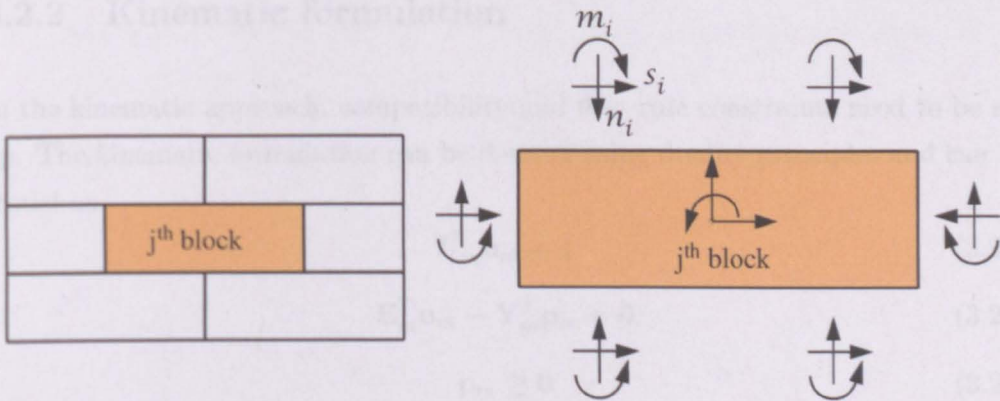
FIGURE 3.5: Typical block assemblage

The static (equilibrium) approach of classic limit analysis theory requires that both equilibrium and yield function constraints be met. Within this framework

the variables are the stress resultants and the load factor. Contact and block forces, dimensions and frictional properties are shown on figure 3.5. The problem variables are the contact forces: n_i, s_i, m_i (where $n_i \geq 0$; s_i, m_i are unrestricted 'free' variables), and the unknown collapse load factor λ. Assuming there are b blocks and c contact surfaces, the equilibrium and yield constraint equations may be stated for the problem as follows:

$$E_m q_m - \lambda f_{mL} = f_{mD} \qquad (3.18)$$

and

$$Y_m q_m \leq 0 \qquad (3.19)$$

where E_m is a suitable $(3b \times 3c)$ equilibrium matrix for the masonry containing direction cosines and can be worked out from equation 3.6. q_m and f_m are respectively vectors of contact forces and block loads, $q_m = \{n_1, s_1, m_1, \ldots, n_c, s_c, m_c\}^T$ and $f_m = f_{mD} + \lambda f_{mL}$ where f_{mD} and f_{mL} are respectively vectors of dead and live loads, which applied at the block centroid. Y_m is a suitable yield constraint matrix that can be derived from equation 3.1.

3.2.2 Kinematic formulation

In the kinematic approach, compatibility and flow rule constraints need to be set up. The kinematic formulation can be derived using duality principles and can be stated as

$$f_{Lm}^T u_m = 1 \qquad (3.20)$$

$$E_m^T u_m - Y_m^T p_m = 0 \qquad (3.21)$$

$$p_m \geq 0 \qquad (3.22)$$

where u_m is a $3b$-vector of nodal unconstrained displacements corresponding to the nodal loads f_m and p_m is plastic multiplier vector.

3.2.3 Extension of masonry model for crushing failure

This model is introduced by Orduna (2003) and it takes into account crushing failure between blocks. In figure 3.7, t_i is half the length of a interface i and w_i is the width of the joint normal to the plane of the model. The stress value y_c given in equation 3.23 is the compressive strength of material, $\alpha = 0.67$ is the factor allows from the difference between the bending strength and the cube crushing strength of concrete (see e.g Mosley et al. (1999)). The constant stress distribution hypothesis leads to a hinge yield function given by equations:

$$|m_i| + n_i(t_i + \frac{n_i}{2\alpha y_c w_i}) \leq 0 \qquad (3.23)$$

However, the constraints in equation 3.23 are non-linear; thus if a LP solver is still to be used to obtain a solution to the global problem, then these constraints need to be approximated as a series of linear constraints. In order to minimise the number of constraints in the problem (and to maximise computational efficiency) an iterative solution algorithm which involves only refining the representation of the failure envelope where required is used. The algorithm of the adaptive linearization of masonry crushing yield surface is described as below:

1. For each contact i, initially add three linear constraints (i.e. OA, OB and AB on figure 3.6)

2. Obtain a solution to the global LP problem

3. For each contact i, calculate the violation factor v_i as

$$v_i = \frac{|m_i|}{n_i(t_i + \frac{n_i}{2\alpha y_c w_i})}$$

4. For each contact with $v_i > 1$ (i.e. violation), add an additional linear constraint (e.g. in the case of point X_0 on figure 3.6, introduce a new linear constraint tangential to the true non-linear constraint at X_1).
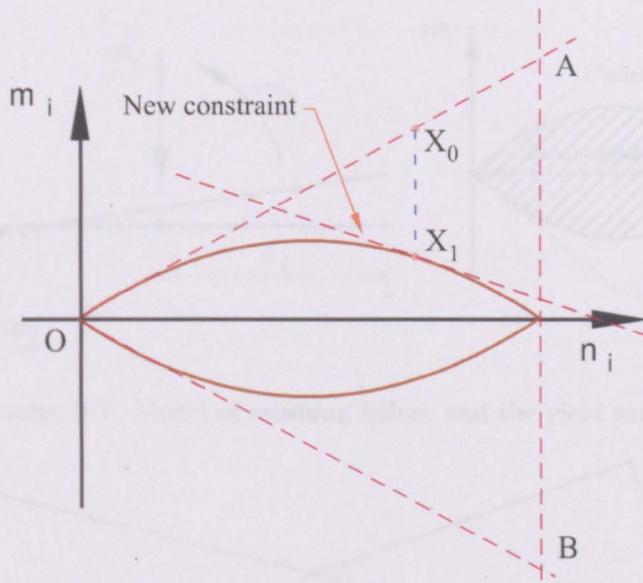
FIGURE 3.6: Adaptive linearization of masonry crushing yield surface

5. Repeat from step (2) until the maximum value of $v_i < 1 + $ tol, where tol is taken as a suitably small value.

The kinematic formulation requires that flow corresponding to hinging satisfies the normality rule. Thus from figure 3.7, the flow rule can be stated as:

$$\left\{ \begin{array}{c} \delta n_i \\ \delta m_i \end{array} \right\} = \left[\begin{array}{cc} l_i(1 + \frac{n_i}{\alpha y_c w_i}) & l_i(1 + \frac{n_i}{\alpha y_c w_i}) \\ 1 & -1 \end{array} \right] \left\{ \begin{array}{c} p_1 \\ p_2 \end{array} \right\} \tag{3.24}$$

3.3 Formulation of strengthening element

Metallic reinforcing elements are often used to strengthen ancient masonry structures. These structural elements endow parts of the structure with tensile capacity, but, due to their high slenderness, have low compressive strength. Tie elements are therefore usually assumed to have tensile strength but zero compressive strength. The tensile force provided by a tie element resists the crack opening between
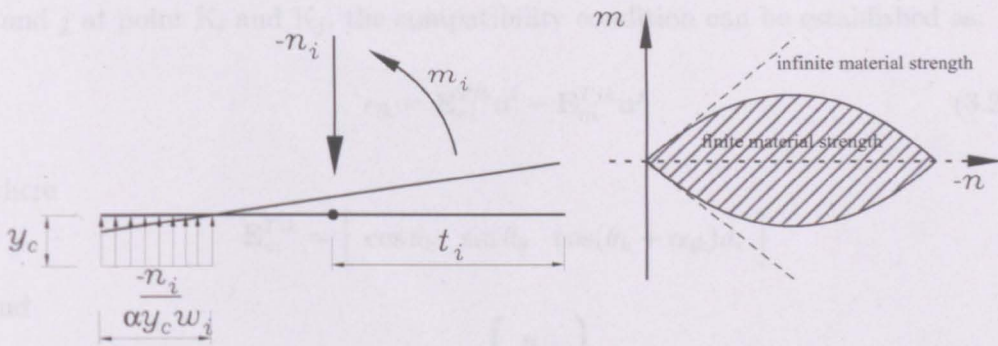
FIGURE 3.7: Model of crushing failure and the yield surface
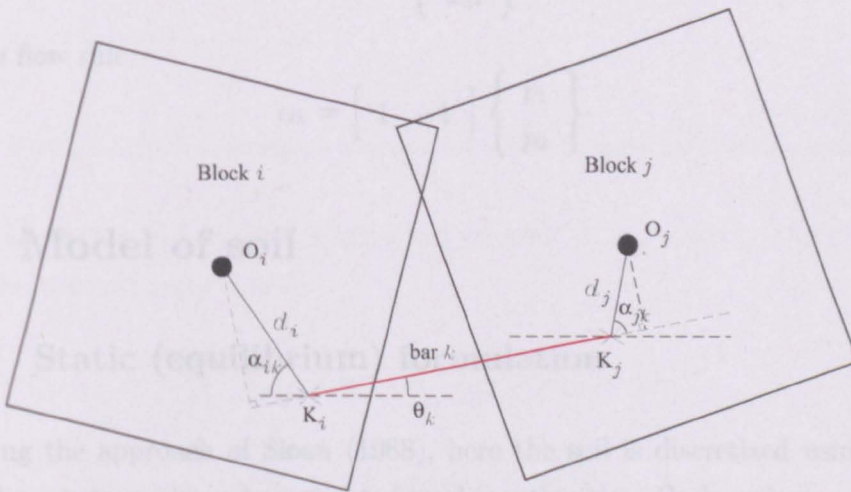
FIGURE 3.8: Strengthening element geometry

blocks. Denoting the yield stress of a tie element i as y_{sti}, the yield function is defined by equation 3.25.

$$q_{sti}^+ \leq a_i y_{sti} \tag{3.25}$$

$$q_{sti}^+ \geq 0 \tag{3.26}$$

in which, tensile member force $q_{sti}+$ is a LP variable and a_i is the cross-sectional area of element i. In the kinematic formulation, the strain rate ϵ_{lk} of bar k in figure 3.8 needs to comply with the normality condition. For a tie bar k, connecting block

i and j at point K_i and K_j, the compatibility condition can be established as:

$$\epsilon_{lk} = \mathbf{E}_m^{Tik}\mathbf{u}^i - \mathbf{E}_m^{Tjk}\mathbf{u}^j \qquad (3.27)$$

where

$$\mathbf{E}_m^{Tik} = \begin{bmatrix} \cos\theta_k & \sin\theta_k & \cos(\theta_k + \alpha_{ik})d_i \end{bmatrix}$$

and

$$\mathbf{u}^i = \begin{Bmatrix} u_{xi} \\ u_{yi} \\ \omega_{zi} \end{Bmatrix}$$

and the flow rule

$$\epsilon_{lk} = \begin{bmatrix} 1 & -1 \end{bmatrix} \begin{Bmatrix} p_1 \\ p_2 \end{Bmatrix} \qquad (3.28)$$

3.4 Model of soil

3.4.1 Static (equilibrium) formulation

Following the approach of Sloan (1988), here the soil is discretized using three-noded linear-stress elements separated by discontinuities. Each node in a triangular element therefore has three unknown stresses, which are constrained so as to satisfy (linear) equilibrium and (non-linear) yield constraints. Linear programming (LP) can however be applied if the Mohr-Coulomb failure envelope is approximated by a polygon. Unlike Sloan, here the yield surface is instead approximated with an exterior polygon and then adaptively refined using an efficient iterative LP solution scheme which terminates when no stresses violate yield, thereby ensuring the true 'nonlinear' yield surface is enforced.

The assumed stress field

The soil is discretized into a number of triangular elements and separated by discontinuities. The variation of the stress throughout each element is linear and
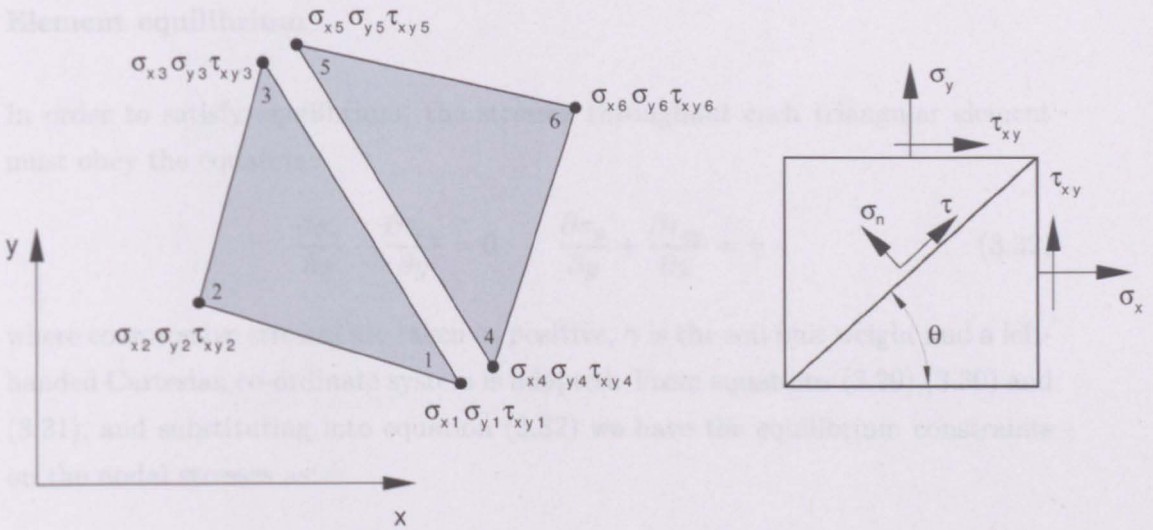
FIGURE 3.9: Linear stress triangle with discontinuity and nodal stress

each node is associated with 3 unknown stresses σ_x, σ_y and τ_{xy}. Stresses vary across an element according to:

$$\sigma_x = \sum_{i=1}^{3} N_i \sigma_{xi} \; ; \; \sigma_y = \sum_{i=}^{3} N_i \sigma_{yi} \; ; \; \tau_{xy} = \sum_{i=1}^{3} N_i \tau_{xyi} \tag{3.29}$$

where σ_{xi}, σ_{yi} and τ_{xyi} are the nodal stresses and N_i are linear shape functions. The latter are given by:

$$N_1 = (\xi_1 + \eta_1 x + \zeta_1 y)/2A; \; N_2 = (\xi_2 + \eta_2 x + \zeta_2 y)/2A; \; N_3 = (\xi_1 + \eta_1 x + \zeta_1 y)/2A \tag{3.30}$$

where

$$\begin{aligned}
\xi_1 &= x_2 y_3 - x_3 y_2 & \eta_1 &= y_2 - y_3 & \zeta_1 &= x_3 - x_2 \\
\xi_2 &= x_3 y_1 - x_1 y_3 & \eta_2 &= y_3 - y_1 & \zeta_2 &= x_1 - x_3 \\
\xi_3 &= x_1 y_2 - x_2 y_1 & \eta_3 &= y_1 - y_2 & \zeta_3 &= x_2 - x_1
\end{aligned} \tag{3.31}$$

and $2A = |\eta_1 \zeta_2 - \eta_2 \zeta_1|$ is twice the element area.

Element equilibrium

In order to satisfy equilibrium, the stresses throughout each triangular element must obey the equation:

$$. \frac{\partial \sigma_x}{\partial x} + \frac{\partial \tau_{xy}}{\partial y} = 0 \qquad \frac{\partial \sigma_y}{\partial y} + \frac{\partial \tau_{xy}}{\partial x} = \gamma \qquad (3.32)$$

where compressive stresses are taken as positive, γ is the soil unit weight and a left-handed Cartesian co-ordinate system is adopted. From equations (3.29),(3.30) and (3.31), and substituting into equation (3.32) we have the equilibrium constraints on the nodal stresses as:

$$\frac{1}{2.4} \begin{bmatrix} \eta_1 & 0 & \zeta_1 & \eta_2 & 0 & \zeta_2 & \eta_3 & 0 & \zeta_3 \\ 0 & \zeta_1 & \eta_1 & 0 & \zeta_2 & \eta_2 & 0 & \zeta_3 & \eta_3 \end{bmatrix} \begin{Bmatrix} \sigma_{x1} \\ \sigma_{y1} \\ \tau_{xy1} \\ \sigma_{x2} \\ \sigma_{y2} \\ \tau_{xy2} \\ \sigma_{x3} \\ \sigma_{y3} \\ \tau_{xy3} \end{Bmatrix} = \begin{bmatrix} 0 \\ \gamma \end{bmatrix} \qquad (3.33)$$

or in short, for each element i, the equilibrium can be written as

$$\mathbf{E}_s^i \sigma_s^i = \mathbf{b}_e^i \qquad (3.34)$$

Therefore, the equilibrium condition for each triangular element generates two equality constraints on the nodal stresses.
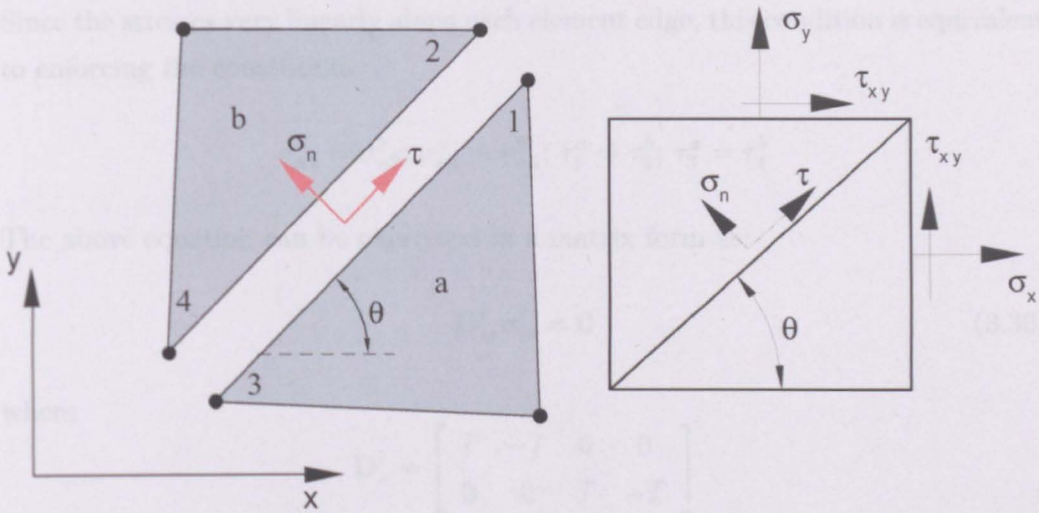
FIGURE 3.10: Statically admissible stress discontinuity between triangles

Equilibrium at discontinuities

It is necessary to impose additional constraints on the nodal stress at the edges
of adjacent triangles in order to permit statically admissible discontinuities. The
condition requires the continuity of the corresponding shear and normal stresses
to be maintained. The normal and shear stresses acting on a plane inclined at an
angle θ to the x-axis (anticlockwise = positive) are given by:

$$\sigma_n = \sin^2\theta\sigma_x + \cos^2\theta\sigma_y - \sin 2\theta\tau_{xy} \tag{3.35}$$

$$\tau = -\frac{1}{2}\sin 2\theta\sigma_x + \frac{1}{2}\sin 2\theta\sigma_y + \cos 2\theta\tau_{xy}$$

Figure 3.10 illustrates two triangles, a and b, which share a side i defined by the
nodal pairs (1,2) and (3,4). Equilibrium at the discontinuity requires that at every
point along i:

$$\sigma_n^a = \sigma_n^b \qquad \tau^a = \tau^b$$

Since the stresses vary linearly along each element edge, this condition is equivalent to enforcing the constraints:

$$\sigma^a_{n1} = \sigma^b_{n2}; \ \sigma^a_{n3} = \sigma^b_{n4}; \ \tau^a_1 = \tau^b_2; \ \tau^a_3 = \tau^b_4$$

The above equation can be expressed in a matrix form as:

$$\mathbf{D}^i_{ss}\sigma^i_{ss} = 0 \tag{3.36}$$

where

$$\mathbf{D}^i_s = \begin{bmatrix} T & -T & 0 & 0 \\ 0 & 0 & T & -T \end{bmatrix}$$

in which

$$T = \begin{bmatrix} \sin^2\theta & \cos^2\theta & -\sin 2\theta \\ -0.5\sin 2\theta & 0.5\sin 2\theta & \cos 2\theta \end{bmatrix}$$

and

$$\sigma^i_{ss} = \{\sigma^a_{x1}, \sigma^a_{y1}, \tau^a_{xy1}, \sigma^b_{x2}, \sigma^b_{y2}, \tau^b_{xy2}, \sigma^a_{x3}, \sigma^a_{y3}, \tau^a_{xy3}, \sigma^b_{x4}, \sigma^b_{y4}, \tau^b_{xy4}\}^T$$

Boundary conditions

In order to enforce prescribed boundary conditions, it is necessary to impose additional constraints on the nodal stresses at boundaries. For each element on the boundary, the equilibrium necessary constraint is:

$$\sigma_{n1} = n_1; \ \sigma_{n2} = n_2; \ \tau_1 = t_1; \ \tau_2 = t_2$$

where n_1, n_2, t_1, t_2 are the external normal and shear stresses acting on the boundary at node 1, 2. In a matrix form, the boundary condition for boundary i can be stated as:

$$\mathbf{B}^i_b\sigma^i_b = \mathbf{b}^i_b \tag{3.37}$$

where

$$\sigma^i_b = \{\sigma_{x1}, \sigma_{y1}, \tau_{xy1}, \sigma_{x2}, \sigma_{y2}, \tau_{xy2}\}^T$$

and

$$B_b = \begin{bmatrix} T & 0 \\ 0 & T \end{bmatrix} \text{ with } T = \begin{bmatrix} \sin^2 \theta & \cos^2 \theta & -\sin 2\theta \\ -0.5 \sin 2\theta & 0.5 \sin 2\theta & \cos 2\theta \end{bmatrix}.$$

Yield condition
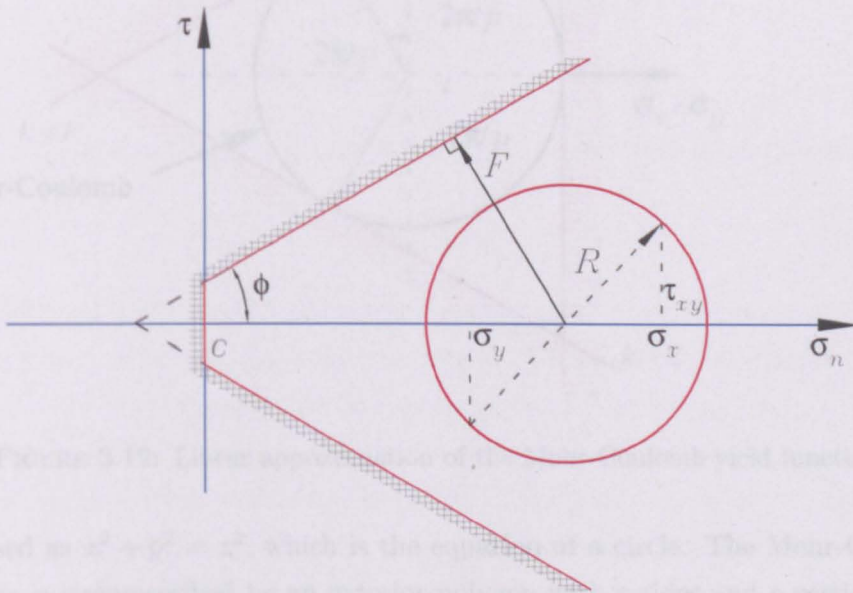
FIGURE 3.11: Mohr-Coulomb yield criterion with a tension cut-off

The plane strain Mohr-Coulomb criterion can be modified by introducing a tension cut-off. The Mohr-Coulomb admissible domain is expressed by the inequality:

$$Y = \sqrt{(\sigma_x - \sigma_y)^2 + (2\tau_{xy})^2} - (2c \cos \phi + (\sigma_x + \sigma_y) \sin \phi) \leq 0 \qquad (3.38)$$

The tension cut-off (σ_t) admissible domain is expressed by the inequality

$$Y_t = \sqrt{(\sigma_x - \sigma_y)^2 + (2\tau_{xy})^2} - (\sigma_x + \sigma_y) - \sigma_t \leq 0 \qquad (3.39)$$

Since linear programming is to be employed, it is necessary to approximate the Mohr-Coulomb cone by a piecewise linear yield surface. By letting $x = \sigma_x - \sigma_y, y = 2\tau_{xy}$ and $z = 2c \cos \phi + (\sigma_x + \sigma_y) \sin \phi$, the Mohr-Coulomb criterion may be
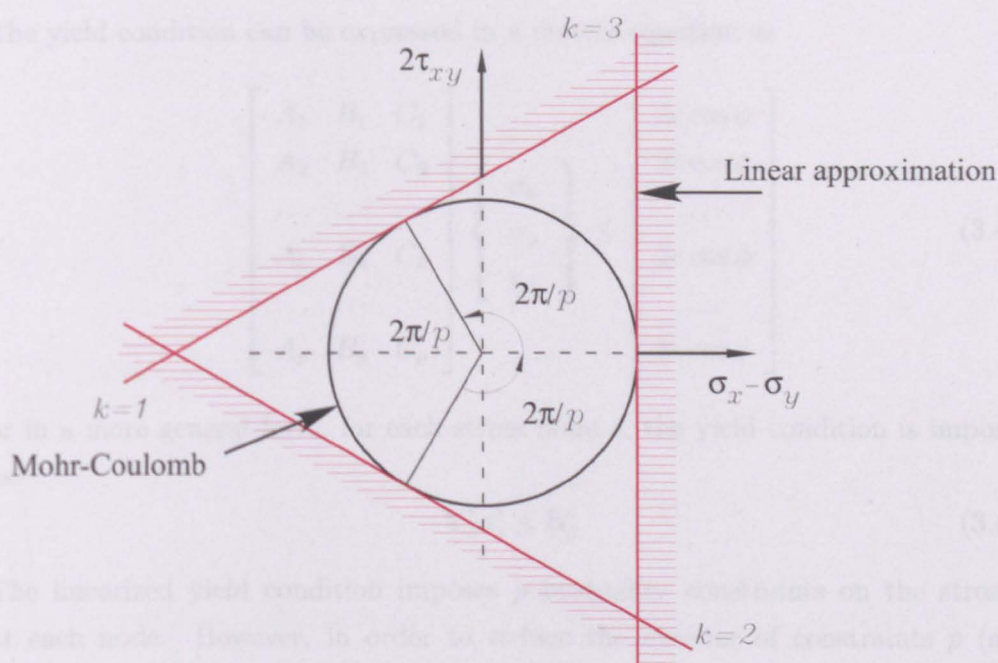
FIGURE 3.12: Linear approximation of the Mohr-Coulomb yield function

expressed as $x^2 + y^2 = z^2$, which is the equation of a circle. The Mohr-Coulomb criterion is circumscribed by an exterior polygon with p sides and p vertices. The x and y co-ordinates of the kth and $(k+1)$th vertices are

$$x_k = z\cos(\alpha_k - \beta)/\cos\beta \qquad y_k = z\sin(\alpha_k - \beta)/\cos\beta$$
$$x_{k+1} = z\cos(\alpha_k + \beta)/\cos\beta \qquad y_{k+1} = z\sin(\alpha_k + \beta)/\cos\beta$$

where $\beta = \pi/p$ and $\alpha_k = 2k\beta$. Thus for the kth linearized plane, the yield function can be written as:

$$Y_k = A_k\sigma_x + B_k\sigma_y + C_k\tau_{xy} - 2c\cos\phi \leq 0 \qquad (3.40)$$

where

$$A_k = \cos\alpha_k + \sin\phi; \ B_k = \sin\phi - \cos\alpha_k; \ C_k = 2\sin\alpha_k; \ k = 1, 2, \ldots, p \qquad (3.41)$$

The yield condition can be expressed in a matrix equation as

$$
\begin{bmatrix}
A_1 & B_1 & C_1 \\
A_2 & B_2 & C_2 \\
\cdots & \cdots & \cdots \\
A_k & B_k & C_k \\
\cdots & \cdots & \cdots \\
A_p & B_p & C_p
\end{bmatrix}
\begin{Bmatrix}
\sigma_x \\
\sigma_y \\
\tau_{xy}
\end{Bmatrix}
\leq
\begin{bmatrix}
2c\cos\phi \\
2c\cos\phi \\
\cdots \\
2c\cos\phi \\
\cdots \\
2c\cos\phi
\end{bmatrix}
\tag{3.42}
$$

or in a more general form, for each stress point i, the yield condition is imposed as:

$$
\mathbf{Y}_s^i \sigma_s^i \leq \mathbf{b}_y^i
\tag{3.43}
$$

The linearized yield condition imposes p inequality constraints on the stresses at each node. However, in order to reduce the number of constraints p (and hence also the total number of constraints in the LP problem), the yield surface can be approximated using a small number for p and by then adaptively refining the yield surface using an efficient iterative LP solution scheme which terminates when no stresses violate yield, thereby ensuring the true (nonlinear) yield surface is enforced. The algorithm of the adaptive linearization of the Mohr-Coulomb yield criterion is described as below:

1. For each stress point i, initially add three linear constraints (i.e. OA, OB and AB on figure 3.13)

2. Obtain a solution to the global LP problem

3. For each stress point i, calculate the violation factor v_i as

$$
v_i = \frac{\sqrt{(\sigma_{xi} - \sigma_{yi})^2 + (2\tau_{xyi})^2}}{2c\cos\phi + (\sigma_{xi} + \sigma_{yi})\sin\phi}
$$
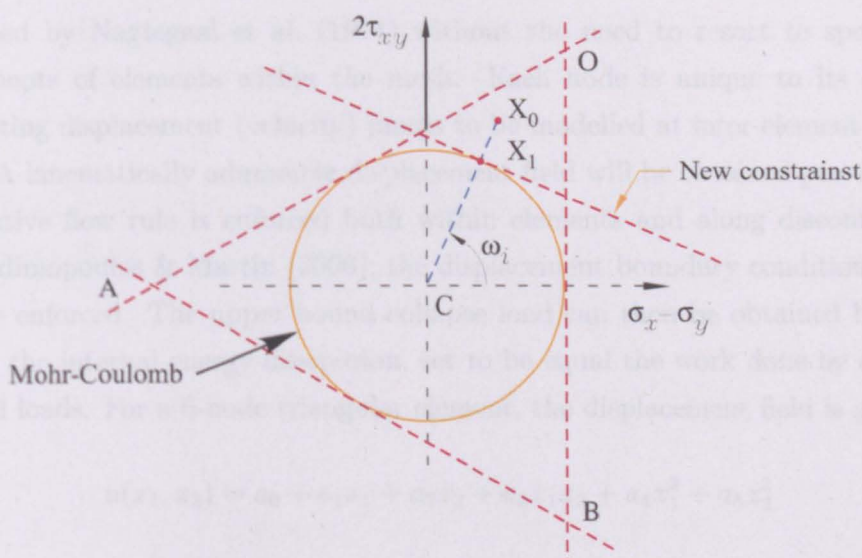
FIGURE 3.13: Adaptive linearization of the Mohr-Coulomb yield criterion

4. For each stress point with $v_i > 1$ (i.e. violation), for example point X_0 in figure 3.13, work out the angle as

$$\tan(\omega_i) = \frac{(\sigma_{xi} - \sigma_{yi})}{2\tau_{xyi}}$$

and thus point X_1 can be determined. Introduce a new linear constraint tangential to the true non-linear yield surface at point X_1.

5. Repeat from step (2) until the maximum value of $v_i < 1 + \text{tol}$, where tol is taken as a suitably small value.

3.4.2 Kinematic formulation

The soil is discretized using six-noded linear strain elements with straight sides. The apex of each triangular element is associated with a specified number of plastic multipliers. This allows the soil behavior to be modelled more accurately than when using lower order elements, e.g. the three-noded constant strain elements used by Cavicchi & Gambarotta (2005). It also avoids the locking problem

discussed by **Nagtegaal** et al. (1974) without the need to resort to special arrangements of elements within the mesh. Each node is unique to its element permitting displacement (velocity) jumps to be modelled at inter-element boundaries. A kinematically admissible displacement field will be obtained provided the associative flow rule is enforced both within elements and along discontinuities Makrodimopoulos & Martin (2006); the displacement boundary condition should also be enforced. The upper bound collapse load can then be obtained by minimizing the internal energy dissipation, set to be equal the work done by external applied loads. For a 6-node triangular element, the displacement field is given by

$$u(x_1, x_2) = a_0 + a_1 x_1 + a_2 x_2 + a_3 x_1 x_2 + a_4 x_1^2 + a_5 x_2^2 \qquad (3.44)$$

This means that any strain component varies according to

$$\epsilon(x_1, x_2) = b_0 + b_1 x_1 + b_2 x_2 \qquad (3.45)$$

and thus the strain at any point within the area of the element can be expressed as a linear combination of the strains at the three vertices. If the sides are straight, the strains at any point in the triangle can be defined by the strain tensors at the vertices. Moreover, the strains of an interior point is a convex combination of the strains at the vertices. Therefore, it is then sufficient to enforce the flow rule at the vertices only, since for a convex yield function, the corresponding set of plastically admissible strains is also convex. Considering the side i, k, j of element shown in
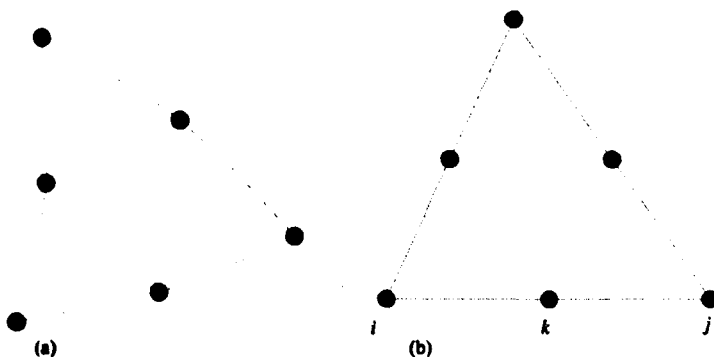
FIGURE 3.14: (a)General 6-node element. (b)6-node element with straight sides

figure 3.14, the side is straight if the following condition is satisfied

$$\mathbf{x}_k = \frac{1}{2}(\mathbf{x}_i + \mathbf{x}_j) \tag{3.46}$$

Assuming ξ is the reference coordinates where $-1 \leq \xi \leq 1$, the coordinates along the side are given by:

$$\mathbf{x} = N_i \mathbf{x}_i + N_k \mathbf{x}_k + N_j \mathbf{x}_j \tag{3.47}$$

where

$$N_i = \frac{1}{2}\xi(\xi - 1), \qquad N_k = 1 - \xi^2, \qquad N_j = \frac{1}{2}\xi(1 + \xi) \tag{3.48}$$

This leads to

$$\mathbf{x} = \frac{1}{2}(\mathbf{x}_i + \mathbf{x}_j - 2\mathbf{x}_k)\xi^2 + \frac{1}{2}(\mathbf{x}_j - \mathbf{x}_i)\xi + \mathbf{x}_k \tag{3.49}$$

from which, it is clear that equation 3.46 must hold in order for the quadratic term to be zero.

The assumed displacement field
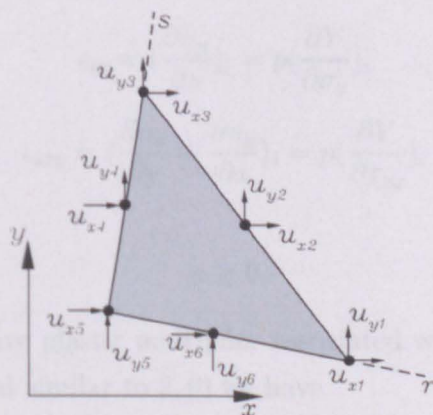
FIGURE 3.15: The six-noded linear strain triangles for upper bound limit analysis

The displacements (velocities) are assumed to vary throughout each triangle according to:

$$u_x = \sum_{i=1}^{6} N_i u_{xi} \; ; \; u_y = \sum_{i=1}^{6} N_i u_{yi} \tag{3.50}$$

where u_{xi} and u_{yi} are the nodal velocities in the x and y directions respectively and N_i are quadratic shape functions. The latter are defined as:

$$N_1 = (1 - r - s)(1 - 2r - 2s) \quad N_2 = r(2r - 1) \quad N_3 = s(2s - 1)$$
$$N_4 = 4r(1 - r - s) \qquad N_5 = 4rs \qquad N_6 = 4s(1 - r - s) \tag{3.51}$$

in which r and s are reference coordinates as shown on figure 3.15.

Flow rule constraints in triangles

In the upper bound theorem, a rigid-perfectly plastic material model with an associated flow rule is assumed. The plastic strain varies linearly throughout each triangle. It can be shown that the plastic flow rule will be satisfied everywhere within an element if the flow rule is applied at each apex of the element. The plastic flow rule at each apex i can be written as:

$$\epsilon_{ix} = \left(\frac{\partial u_x}{\partial x}\right)_i = p\left(\frac{\partial Y}{\partial \sigma_x}\right)_i \tag{3.52}$$

$$\epsilon_{iy} = \left(\frac{\partial u_y}{\partial y}\right)_i = p\left(\frac{\partial Y}{\partial \sigma_y}\right)_i \tag{3.53}$$

$$\epsilon_{ixy} = \left(\frac{\partial u_x}{\partial y} + \frac{\partial u_y}{\partial x}\right)_i = p\left(\frac{\partial Y}{\partial \tau_{xy}}\right)_i \tag{3.54}$$

and

$$p \geq 0 \tag{3.55}$$

where p is a non-negative plastic multiplier associated with the corner node i. Y is the yield function and similar to 3.40 we have

$$Y_k = A_k \sigma_x + B_k \sigma_y + C_k \tau_{xy} - 2c \cos \phi = 0 \tag{3.56}$$

Thus, from equations 3.56 to 3.53, the plastic strain can be expressed as

$$\epsilon_{ix} = \sum_{k=1}^{\mu} p_{ik} \frac{\partial Y_k}{\partial \sigma_x} = \sum_{k=1}^{\mu} p_{ik} A_k$$

$$\epsilon_{iy} = \sum_{k=1}^{\mu} p_{ik}\frac{\partial Y_k}{\partial \sigma_y} = \sum_{k=1}^{\mu} p_{ik}B_k$$

$$\epsilon_{ixy} = \sum_{k=1}^{\mu} p_{ik}\frac{\partial Y_k}{\partial \tau_{xy}} = \sum_{k=1}^{\mu} p_{ik}C_k$$

where p_{ik} is the plastic multiplier of node i and kth side of the yield surface. By using the displacement interpolation and differentiating the shape functions, the flow rule can be formed as a set of equality constraints of the form:

$$\mathbf{G}_s^i\mathbf{u}_s^i + \mathbf{Y}_s^{T^i}\mathbf{p}_s^i = 0 \qquad (3.57)$$

where

$$\mathbf{G}_s^i = \begin{bmatrix} (\frac{\partial N_1}{\partial x})_i & 0 & \dots & (\frac{\partial N_6}{\partial x})_i & 0 \\ 0 & (\frac{\partial N_1}{\partial y})_i & \dots & 0 & (\frac{\partial N_6}{\partial y})_i \\ (\frac{\partial N_1}{\partial y})_i(\frac{\partial N_1}{\partial x})_i & & \dots & & (\frac{\partial N_6}{\partial y})_i(\frac{\partial N_6}{\partial x})_i \end{bmatrix} \qquad (3.58)$$

and

$$\frac{\partial N_j}{\partial_x} = \frac{N_j}{\partial r}\frac{\partial r}{\partial x} + \frac{N_j}{\partial s}\frac{\partial s}{\partial x}$$

$$\frac{\partial N_j}{\partial_y} = \frac{N_j}{\partial r}\frac{\partial r}{\partial y} + \frac{N_j}{\partial s}\frac{\partial s}{\partial y}$$

$$\mathbf{u}_s^i = \{u_{x1}, u_{y1}, \dots, u_{x6}, u_{y6}\}^T$$

$$\mathbf{p}_s^i = \{p_{i1}, p_{i2}, \dots, p_{ip}\}^T$$

with $i = 1 \rightarrow 3, j = 1 \rightarrow 6$. The flow rule imposes nine equality constraints on the nodal velocities and plastic multiplier for each triangle. Each plastic multiplier is also subject to non-negativity constraints.

Flow rule constraint in discontinuities

As shown on figure 3.16, at the interface between elements a and b, the displacement jump at node $(3, 3')$ can be expressed as:

$$\Delta u_{n33'} = (u_{x3} - u_{x3'})\cos\theta + (u_{y3} - u_{y3'})\sin\theta$$
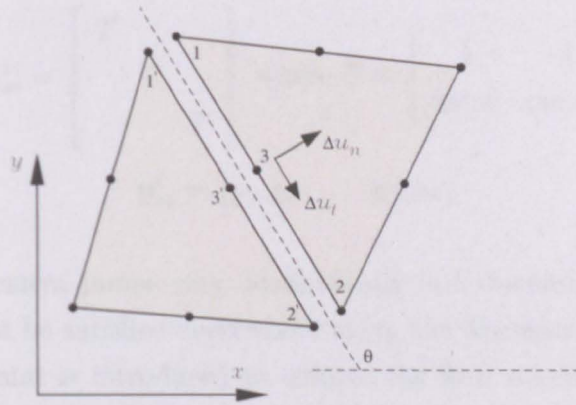
FIGURE 3.16: Velocity discontinuity

$$\Delta u_{t33'} = (u_{x3} - u_{x3'}) \sin\theta + (u_{y3} - u_{y3'}) \cos\theta$$

where $\Delta u_{n33'}$ and $\Delta u_{t33'}$ are displacement jumps, θ is the angle of discontinuity to the x-axis.

The flow rule condition at node $(3, 3')$ can be expressed as:

$$\begin{bmatrix} 1 & -1 \\ \tan\phi & \tan\phi \end{bmatrix} \begin{Bmatrix} p_1 \\ p_{1'} \end{Bmatrix}$$

Thus flow rule for the discontinuity i can be expressed as

$$\mathbf{H}_{ss}^i \mathbf{u}_{ss}^i - \mathbf{K}_{ss}^i \mathbf{p}_{ss}^i = 0 \qquad (3.59)$$

in which

$$\mathbf{H}_{ss}^i = \begin{bmatrix} T & & \\ & T & \\ & & T \end{bmatrix} \quad \text{where } T = \begin{bmatrix} \cos\theta & \sin\theta & -\cos\theta & -\sin\theta \\ \sin\theta & \cos\theta & -\sin\theta & -\cos\theta \end{bmatrix}$$

and

$$\mathbf{u}_{ss}^i = \left\{ u_{x1}, u_{y1}, u_{x1'}, u_{y1'}, \ldots, u_{x3}, u_{y3}, u_{x3'}, u_{y3'} \right\}^T$$

$$\mathbf{K}^i_{ss} = \begin{bmatrix} T & & \\ & T & \\ & & T \end{bmatrix} \quad \text{where } T = \begin{bmatrix} 1 & -1 \\ \tan\phi & \tan\phi \end{bmatrix}$$

$$\mathbf{p}^i_{ss} = \{p_1, p_{1'}, \ldots, p_3, p_{3'}\}$$

· Since the displacement jumps vary quadratically in a discontinuity, the flow-rule condition may not be satisfied everywhere along the discontinuity. Therefore, an additional constraint is introduced to enforce the flow condition by forcing the displacement jumps to vary linearly.

$$\Delta u_{33'} - \frac{1}{2}(\Delta u_{11'} + \Delta u_{22'}) = 0 \tag{3.60}$$

This condition can simply reduce to:

$$p_1 - p_{1'} + p_2 - p_{2'} - 2(p_3 - p_{3'}) = 0$$

$$p_1 + p_{1'} + p_2 + p_{2'} - 2(p_3 + p_{3'}) = 0$$

or in a matrix form, it can be written as:

$$\mathbf{Q}^i \mathbf{p}^i_{ss} = 0 \tag{3.61}$$

Boundary conditions

To be kinematically admissible, the computed velocity field must satisfy the prescribed boundary conditions. Consider a node i on a boundary which is inclined at an angle θ to the x-axis, where the boundary is subject to a prescribed tangential velocity $\bar{v}$ and normal velocity $\bar{u}$; the condition can be expressed as:

$$\begin{bmatrix} \cos\theta & \sin\theta \\ -\sin\theta & \cos\theta \end{bmatrix} \begin{Bmatrix} u_{xi} \\ u_{yi} \end{Bmatrix} = \begin{Bmatrix} \bar{u}_x \\ \bar{u}_y \end{Bmatrix} \tag{3.62}$$

Thus in a general matrix form, the boundary conditions can be stated as:

$$\mathbf{Z}^i \mathbf{u}_b^i = \mathbf{t}_b^i \tag{3.63}$$

Power dissipations

Plastic flow may occur in both the continuum and at discontinuities. The total power dissipated constitutes the objective function. The power dissipated by plastic deformation throughout each triangle i may be written as:

$$\mathbf{W}_t^i = \int_A (\sigma_x \epsilon_x + \sigma_y \epsilon_y + \tau_{xy} \gamma_{xy}) dA \tag{3.64}$$

where A is element area. After substituting equations 3.52, 3.53 and 3.54, the dissipation can be expressed as:

$$\mathbf{W}_t^i = 2Ac \cos \phi \sum_{k=1}^{\mu} p_k \tag{3.65}$$

Similarly, the power dissipated by plastic shearing along a discontinuity i is given by:

$$\mathbf{W}_d^i = \int_l c u_t^i dl \tag{3.66}$$

in which

$$u_t^i = \mathbf{H}_{ss}^i \mathbf{u}_{ss}^i$$

l is the length of discontinuity and c is soil cohesion.

3.5 Model of soil-masonry interface

3.5.1 Static formulation

Given that the aforementioned soil model is most conveniently formulated in terms of stresses whereas the masonry block model is most conveniently formulated in

terms of stress-resultants (i.e. forces), all that remains is to define a suitable equilibrium relationship to impose at the soil-masonry interface. For each soil to masonry interface i, with length l, the requisite equilibrium constraint can be written as:

$$
\begin{bmatrix}
\frac{l}{2} & \frac{l}{2} & 0 & 0 \\
0 & 0 & \frac{l}{2} & \frac{l}{2} \\
\frac{l^2}{12} & \frac{l^2}{12} & 0 & 0
\end{bmatrix}
\left\{
\begin{array}{c}
\sigma_{ni1} \\
\sigma_{ni2} \\
\tau_{i1} \\
\tau_{i2}
\end{array}
\right\}
-
\left\{
\begin{array}{c}
n_i \\
s_i \\
m_i
\end{array}
\right\}
=
\left\{
\begin{array}{c}
0 \\
0 \\
0
\end{array}
\right\}
$$

or in more general form:

$$
\mathbf{D}_{sm}^i \sigma_{sm}^i - \mathbf{q}_{sm}^i = 0 \tag{3.67}
$$

For each soil to masonry contact i, the requisite yield constraint can be written as:

$$
n_i \tan \phi_i + |s_i| \leq c_i
$$

where c_i and ϕ_i are cohesion and friction of the interface, n_i, s_i, m_i are stress resultants and $\sigma_{ni1}, \sigma_{ni2}, \tau_{i1}, \tau_{i2}$ are normal and shear stress acting on the interface. Thus in a matrix form, the yield constraint for the interface can be written as

$$
\mathbf{Y}_{sm}^i \mathbf{q}_{sm}^i \leq \mathbf{c}^i \tag{3.68}
$$

3.5.2 Kinematic formulation

Flow rule constraints for displacement jumps of a masonry block and a soil element at the interface i can be defined as:

$$
\mathbf{C}_m^i \mathbf{u}_m^i - \mathbf{H}_{sm}^i \mathbf{u}_{sm}^i - \mathbf{K}_{sm}^i \mathbf{p}_{sm}^i = 0 \tag{3.69}
$$

$$
\mathbf{p}_{sm}^i \geq 0 \tag{3.70}
$$
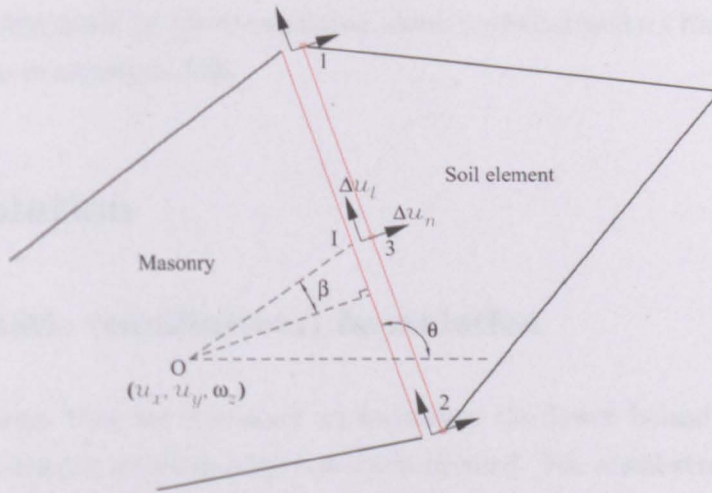
FIGURE 3.17: Soil-masonry discontinuity (kinematic approach)

where $\mathbf{u}_m^i = \{u_x, u_y, \omega_z\}^T$, $\mathbf{u}_{sm}^i = \{u_{x1}, u_{y1}, u_{x2}, u_{y2}, u_{x3}, u_{y3}\}^T$ and $\mathbf{p}_{sm}^i = \{p_1, p_2, p_3, p_4, p_5, p_6\}^T$. θ is the discontinuity angle made to the x-axis and β is defined as on figure 3.17.

$$\mathbf{C}_m^i = \begin{bmatrix} \sin\theta & \cos\theta & -\frac{l}{2} + d_i \cos\beta \\ -\cos\theta & \sin\theta & d_i \sin\beta \\ \sin\theta & \cos\theta & \frac{l}{2} + d_i \cos\beta \\ -\cos\theta & \sin\theta & d_i \sin\beta \\ \sin\theta & \cos\theta & d_i \cos\beta \\ -\cos\theta & \sin\theta & d_i \sin\beta \end{bmatrix}$$

$$\mathbf{H}_{sm}^i = \begin{bmatrix} T & & \\ & T & \\ & & T \end{bmatrix} \quad \text{where } T = \begin{bmatrix} \cos\theta & -\sin\theta \\ \sin\theta & \cos\theta \end{bmatrix}$$

In order to ensure that the flow-rule condition is satisfied everywhere along the discontinuity, an additional constraint is imposed to ensure the displacement jump varies linearly. Similar to equations 3.61, the condition can be stated as

$$\mathbf{Q}^i \mathbf{p}_{sm}^i = \mathbf{0} \tag{3.71}$$

The power dissipated by plastic shearing along a discontinuity i has been defined previously as in equation 3.66.

3.6 Solution

3.6.1 Static (equilibrium) formulation

All of the steps that are necessary to formulate the lower bound theorem as a linear programming problem have now been covered. For a soil-structure interaction (SSI) problem, assume that the masonry parts are discretized into m rigid block elements with n contact interfaces, and there are sm soil-masonry interface elements. Now assume that the soil mass is discretized into s finite elements with d discontinuities. The problem has b boundary conditions and y stress evaluation points in the soil mass. Application of the requisite yield conditions, element equilibrium, discontinuity equilibrium and boundary conditions will lead to the formulation of a LP problem. Thus the load factor λ can be found when the following LP problem is solved:

$$\textbf{max } \lambda \qquad (3.72)$$

subject to:

$$\mathbf{E}_m \mathbf{q}_m - \lambda \mathbf{f}_{mL} = \mathbf{f}_{mD}$$

$$\mathbf{Y}_m \mathbf{q}_m \leq 0$$

$$\mathbf{E}_s \sigma_s = \mathbf{b}_e$$

$$\mathbf{Y}_s \sigma_s \leq \mathbf{b}_y$$

$$\mathbf{D}_{ss} \sigma_{ss} = 0$$

$$\mathbf{D}_{sm} \sigma_{sm} - \mathbf{q}_{sm} = 0$$

$$\mathbf{Y}_{sm} \mathbf{q}_{sm} \leq \mathbf{c}$$

$$\mathbf{B}_b \sigma_b = \mathbf{b}_b$$

In the above equation, $\mathbf{E}_m, \mathbf{q}_m, \mathbf{Y}_m$ have been defined in section 3.2.1, where $\mathbf{E}_m$ is a suitable $(3m \times 3n)$ equilibrium matrix of the masonry, $\mathbf{q}_m$ is a vector of contact forces and $\mathbf{q}_m = \{n_1, s_1, m_1, ..., n_n, s_n, m_n\}^T$. $\mathbf{E}_s$ is a $(9s \times 2s)$ equilibrium matrix of soil elements, obtained from equation 3.34. $\mathbf{Y}_s, \mathbf{Y}_{sm}$ are yield matrices for stress evaluation points and soil-masonry interfaces respectively, and can be derived from equations, 3.43, 3.68. $\mathbf{D}_s$ is a suitable $(12d \times 4d)$ compatibility matrix of soil-soil discontinuities. The boundary conditions are applied using equation 3.37, where $\mathbf{B}_b$ is a $(6b \times 4b)$ matrix, and $\sigma_s, \sigma_{ss}, \sigma_{sm}$ are $(3 \times y)$, $(12 \times d)$, $(4 \times sm)$ vectors of stresses respectively. $\mathbf{q}_{sm}$ is a $(3 \times sm)$ vector of stress resultants at soil-masonry interfaces and $\mathbf{b}_e, \mathbf{b}_y, \mathbf{b}_b$ are vectors of constants which depend on the prescribed material properties and boundary conditions of the soil.

3.6.2 Kinematic formulation

All the equations necessary to formulate an upper bound limit finite element limit analysis problem which can be solved using linear programming have been developed in the preceding sections. For a given SSI problem the upper bound LP problem can be formulated as:

$$\text{min} \quad \mathbf{f}_D^T \mathbf{u}_m + \mathbf{W}_t + \mathbf{W}_d \tag{3.73}$$

subject to:

$$\mathbf{f}_{Lm}^T \mathbf{u}_m = 1$$

$$\mathbf{E}_m^T \mathbf{u}_m - \mathbf{Y}_m^T \mathbf{p}_m = 0$$

$$\mathbf{G}_s \mathbf{u}_s + \mathbf{Y}_s^T \mathbf{p}_s = 0$$

$$\mathbf{C}_m \mathbf{u}_m - \mathbf{H}_{sm} \mathbf{u}_{sm} - \mathbf{K}_{sm} \mathbf{p}_{sm} = 0$$

$$\mathbf{H}_{ss} \mathbf{u}_{ss} - \mathbf{K}_{ss} \mathbf{p}_{ss} = 0$$

$$\mathbf{Q} \mathbf{p}_{sm} = 0$$

$$\mathbf{Q} \mathbf{p}_{ss} = 0$$

$$\mathbf{Z}\mathbf{u}_b = \mathbf{t}_b$$

$$\mathbf{p}_m, \mathbf{p}_{sm}, \mathbf{p}_s, \mathbf{p}_{ss} \geq 0$$

In the above formulation, $\mathbf{W}_t$ is the total power of dissipation of soil elements, whereas $\mathbf{W}_d$ is the total dissipated power within all discontinuities. $\mathbf{W}_t, \mathbf{W}_d$ can respectively be obtained from equations 3.65 and 3.66. $\mathbf{K}_{ss}$ and $\mathbf{K}_{sm}$ are flow matrices representing soil-soil and soil-masonry discontinuities. $\mathbf{H}_{sm}, \mathbf{H}_{ss}$ and $\mathbf{C}_m$ are compatibility matrices connecting the displacements with displacement jumps. $\mathbf{G}_s$ is also a compatibility matrix that connects the displacements with strain-like quantities and is defined in equation 3.58. $\mathbf{p}_m, \mathbf{p}_{sm}, \mathbf{p}_s, \mathbf{p}_{ss}$ are one-dimensional vectors of plastic multipliers. Finally, $\mathbf{Q}$ is a constraint matrix that ensures linear variation of the displacement jumps.

3.7 Layout optimization of grid-like structure: mathematical formulation

To date the focus has been on formulating suitable analysis problems. Now consider the truss design problem, and in particular a potential planar design domain which is discretized using n nodes and m potential connections. The classical 'equilibrium' plastic layout optimization formulation for a single load case is defined in the following equation:

$$\min V = \mathbf{c}^T \mathbf{q}_r$$

subject to:

$$\mathbf{E}_r \mathbf{q}_r = \mathbf{f} \tag{3.74}$$

$$\mathbf{q}_r \geq 0$$

Where V is the total volume of the structure, $\mathbf{q}_r^T = \{q_{r1}^+; q_{r1}^-; q_{r2}^+; q_{r2}^- \dots q_{rm}^-\}$; q_{ri}^+ and q_{ri}^- are the tensile and compressive internal forces in bar $i(i = 1 \dots m)$; $\mathbf{c}^T = \{l_1/\sigma_1, l_1/\sigma_1, l_2/\sigma_2 \dots l_m/\sigma_m\}$ where l_i and σ_i are respectively the length

and yield stress of bar i. $\mathbf{E}_r$ is a suitable $2n \times 2m$ equilibrium matrix and $\mathbf{f}^T = \{f_1^x, f_1^y, f_2^x, f_2^y \ldots f_n^y\}$ where f_j^x and f_j^y are the x and y components of the external load applied to node $j(j = 1 \ldots n)$. The presence of supports at nodes can be accounted for by omitting the relevant terms from $\mathbf{f}$, together with the corresponding rows from $\mathbf{E}_r$. This problem is in a form which can be solved using linear programming (LP), with the member forces in $\mathbf{q}_r$ being the LP variables.

3.7.1 Formulation of the problem of identifying optimal arrangements of reinforcement in masonry structures
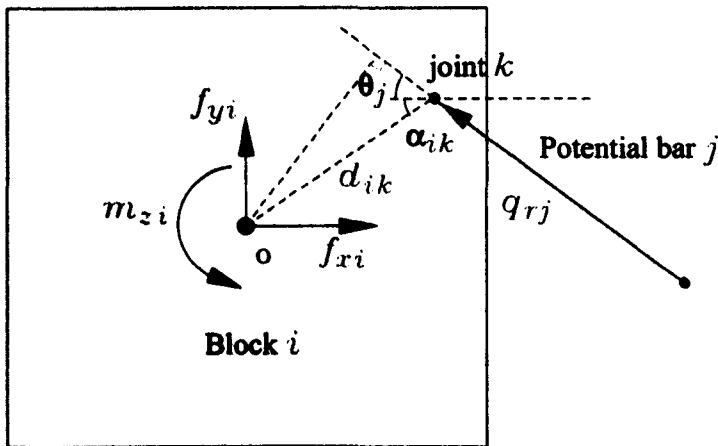
FIGURE 3.18: Design reinforcement for masonry structures

Figure 3.18 shows a potential bar j is connected to block j across joint k. Potential bar j can provide either compressive or tensile force, q_{rj}^+, q_{rj}^-. This magnitude of this force is unknown and will contribute to the equilibrium of block j. Thus equilibrium matrix 3.6 can be modified to take into account the presence of bar j

, leading to the following block equilibrium relationship:

$$
\begin{bmatrix}
\cdots & \cos\theta_j & -\cos\theta_j \\
\cdots & \sin\theta_j & -\sin\theta_j \\
\cdots & \cos(\theta_j + \alpha_{ik})d_{ik} & -\cos(\theta_j + \alpha_{ik})d_{ik}
\end{bmatrix}
\begin{Bmatrix}
\cdot \\
\cdot \\
\cdot \\
q_{rj}^{+} \\
q_{rj}^{-}
\end{Bmatrix}
=
\begin{Bmatrix}
f_{xj} \\
f_{yj} \\
m_{zj}
\end{Bmatrix}
\tag{3.75}
$$

In the above formulation θ_j is the angle potential bar j makes to the x-axis, α_{ik} is the angle of line **Ok** to the x-axis, d_{ik} is the distance from block centroid **O** to joint k. Now the key parts of the formulation needed to design reinforcement in a masonry structure have been derived. This is potentially very useful as after a standard limit analysis has been performed, the structure may well be found to be under strength. This allows the additional reinforcement required to be determined. The goal is to determine the least volume of material needed to strengthen the structure. The full mathematical formulation for this problem requires that equations 3.75,3.74 and 3.72 are used in combination, though noting that the objective function is to minimize the volume of the reinforcing bars. The constraints in equation 3.72 apply with the exception of the equilibrium relationship now governed by equation 3.75.

3.8 Comparison and validation

3.8.1 Strip footing bearing capacity on single layered soil

Generally speaking, foundation bearing capacity problems pose a difficult test for finite element methods because of the singularities that exist at the edges of the footing. In order to obtain good lower bound solutions, particularly with a piecewise linear stress field, it is desirable to have a very fine fan of elements around the singularity point. Also, the accuracy of the solution obtained depends on the soil frictional strength. Due to complex nature of the backfill material in

masonry arch bridge, an additional test has been carried out on a multi-layered soil problem.

Considering a weightless Mohr-Coulomb soil ($c \geq 0, \phi \geq 0, \gamma = 0$) and without surcharge, the bearing capacity of a rigid footing of width B is given by:

$$\frac{Q}{B} = cN_c \tag{3.76}$$

where Q is the limit load and N_c is a dimensionless bearing capacity factor and it depends on ϕ. The exact value of N_c is given by Prandtl (1921):

$$N_c = \left[e^{\pi \tan \phi} \tan^2 \left(\frac{\pi}{4} + \frac{\phi}{2}\right)\right] \tag{3.77}$$

thus $N_c = 2 + \pi$ for weightless cohesive soil. For a cohesionless soil with selfweight, $c = 0, \phi > 0, \gamma > 0$ with no surcharge, the bearing capacity is traditionally expressed as:

$$\frac{Q}{B} = \frac{1}{2}\gamma B N_\gamma \tag{3.78}$$

where N_γ is a dimensionless factor that depends on ϕ. At present, there is no closed-form analytical solution for N_γ; however it can be evaluated by number of numerical methods. The benchmark N_γ using in this study are from Martin (2003), which reports highly accurate solutions based on the method of characteristics (Sokolovskii, 1965). In the initial set of analyses documented in table 3.1, mesh $1 \to 3$ were used to determine lower and upper bound solutions (denoted LB, UB respectively) for the bearing capacity factors N_c ($c = 10kPa$, $\phi = 0$), N_γ ($c = 0$, $\phi = 35°$). All analyses were run on a Dell desktop computer equipped with Intel Core 2 Quad-core 2.4 GHz processor and 2GB of memory. In order to obtain a good solution for N_γ in table 3.2, a fine mesh of 20126 elements (*not shown*) with a manual fan zone contained 80 discontinuity was used. The latter analyses were run on a machine with a 2.4 GHz AMD Opteron (PC technology) processor and 4Gb of memory and running 64-bit Scientific Linux. Table 3.1 shows that close bounds on the exact solution were obtained for a cohesive soil, with the difference between lower and upper bound solutions being generally less than 2%. In the case of a purely frictional soil, the bounds on the exact solution tend to widen as

Mesh	$N_c(5.14)$		$N_\gamma(17.58)$	
	LB (s)	UB (s)	LB (s)	UB (s)
No elements	error%	error%	error%	error%
1	5.108(63)	5.201(65)	15.5(71)	19.7(73)
1057	0.65	1.15	11.8	12.05
2†	5.117(217)	5.183(202)	16.57(232)	19.34 (223)
4327	0.47	0.8	5.74	10.01
3	5.132(389)	5.170(352)	17.01(461)	18.53 (421)
8024	0.22	0.55	3.24	5.4

†see Figure 3.19

TABLE 3.1: Bearing capacity factors N_c, N_γ with different meshes

$\phi°$	Smooth			Rough		
	LB	Martin (2003)	UB	LB	Martin (2003)	UB
	error%		error%	error%		error%
15	0.692	0.699	0.712	1.15	1.182	1.2
	1.05		1.7	2.57		1.57
25	3.395	3.461	3.5	6.29	6.4909	6.71
	1.89		1.1	3.01		2.86
35	17.30	17.58	17.92	33.6	34.47	35.37
	1.57		1.9	2.51		2.34
40	42.49	43.20	44.37	82.64	85.569	89.65
	1.64		2.7	3.42		4.75
45	115.22	117.59	120.9	226.0	234.3	247.59
	2.01		2.81	3.51		5.67

TABLE 3.2: Bearing capacity N_γ with fine mesh

the angle of friction of the soil increases. When a very fine mesh is adopted, the bounds are within 10% of each other provided the angle of friction is less than 45°. The average percentage error in bracketing the exact solution is calculated as follow:

$$\text{error} = \frac{\text{UB} - \text{LB}}{\text{UB} + \text{LB}} \times 100 \qquad (3.79)$$
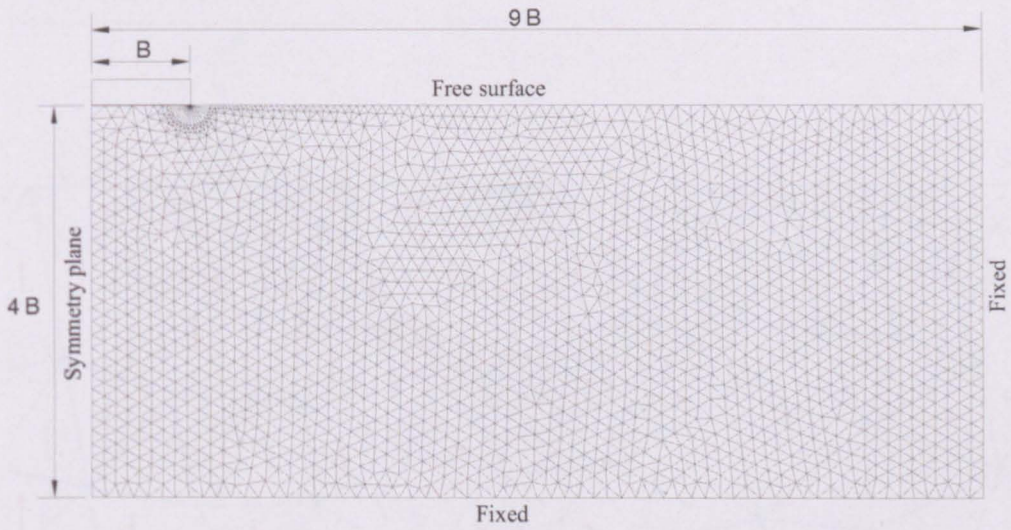
FIGURE 3.19: Strip footing bearing capacity: mesh 2 with 4327 elements
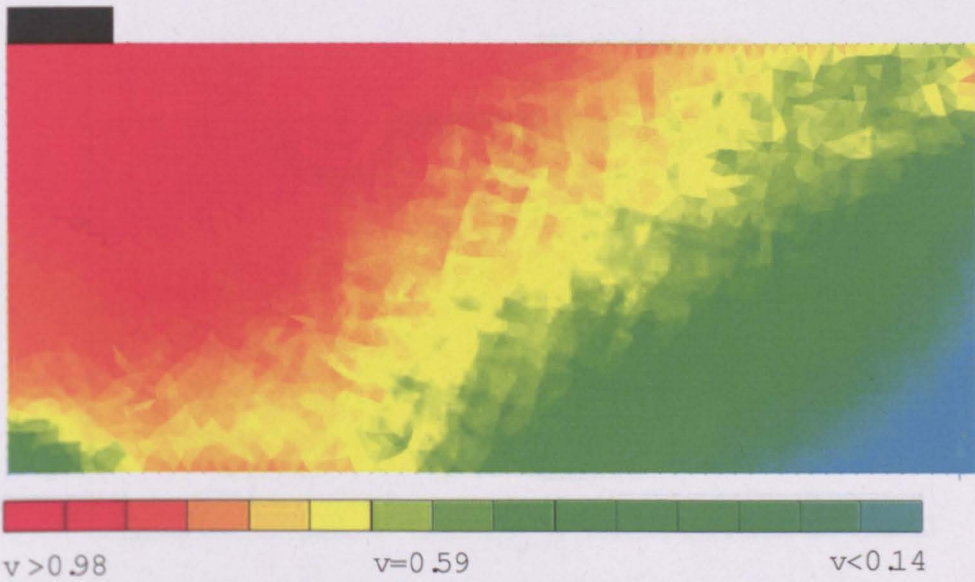
FIGURE 3.20: Proximity to yield: half strip footing resting on a cohesive soil
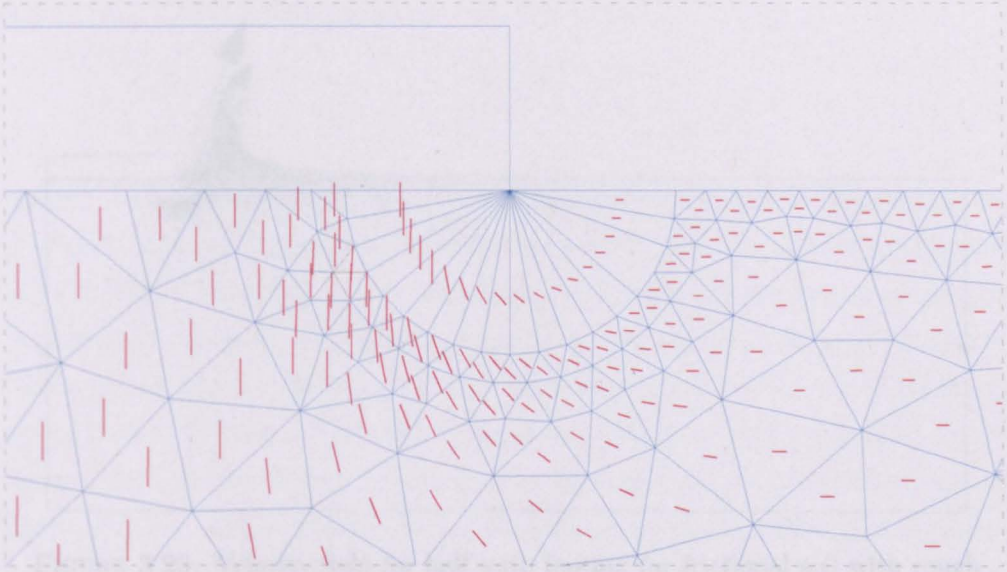
FIGURE 3.21: Principal stress directions: half strip footing on cohesive soil
(around singularity point)
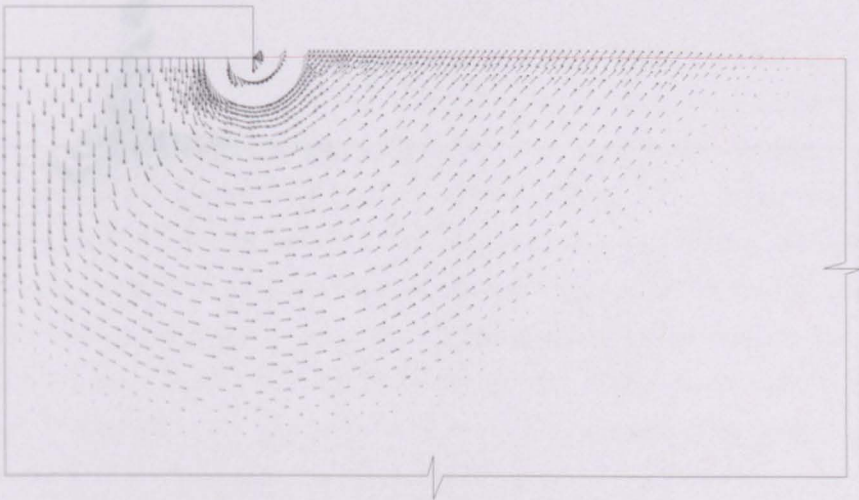
FIGURE 3.22: Velocity field for half strip footing on cohesive soil with rough
footing
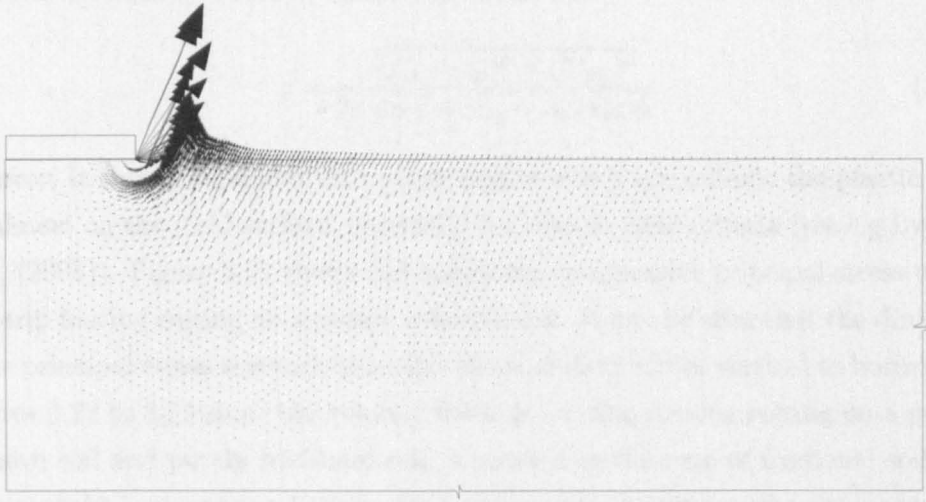
FIGURE 3.23: Velocity field for half strip footing for frictional soil with rough footing ($\phi = 35, \gamma = 5$)
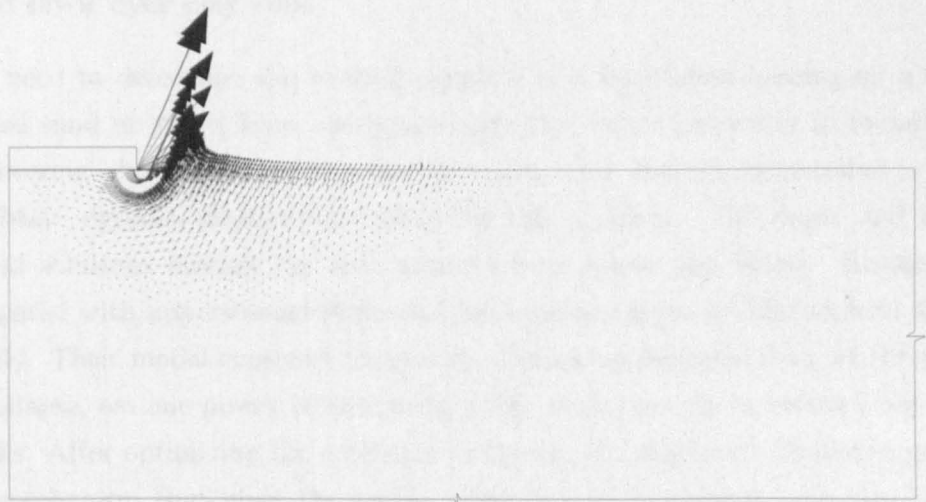
FIGURE 3.24: Velocity field for half strip footing for frictional soil with smooth footing ($\phi = 35, \gamma = 5$)

Figure 3.20 shows the proximity to yield v for a half strip footing resting on a cohesive soil with $c = 10\text{kPa}$, where v is defined as:

$$v = \frac{\sqrt{(\sigma_x - \sigma_y)^2 + (2\tau_{xy})^2}}{2c\cos\phi + (\sigma_x + \sigma_y)\sin\phi} \qquad (3.80)$$

However, it should be noted that many points which are outside the plastic zone are almost on the yield surface, especially for conical yield criteria (see e.g Lyamin et al. (2005)). Figure 3.21 shows the maximum compressive principal stress under the strip footing resting on a purely cohesive soil. It can be seen that the direction of the principal stress is rotating around the singularity from vertical to horizontal. Figures 3.22 to 3.24 show the velocity fields for a strip footing resting on a purely cohesive soil and purely frictional soil. Considering the case of frictional soil, the velocity field is deeper and wider for footing with rough interface compared to footing smooth interface.

3.8.2 Strip footing bearing capacity on two layered soil

Sand layer over clay soils

The need to determine the bearing capacity of a foundation bearing on a compacted sand or gravel layer overlying a soft clay arises frequently in foundation engineering. In this section the finite element limit analysis formulation is used to obtain rigorous plasticity solutions for this problem. The upper and lower bound solutions bracket the true solution from above and below. Results are compared with upper-bound limit analysis solutions given by Michalowski & Shi (1995). Their model considers various rigid block mechanisms that, at the point of collapse, assume power is dissipated solely at the interfaces between adjacent blocks. After optimizing the geometry to furnish the minimum dissipated power, the mechanism that gives the lowest value is used to compute the best upper bound on the limit load. The mesh shown in Figure 3.25 is used for all lower bound and upper bound analyses. The mesh comprises 4192 elements, with a fan-like zone at the singularity. The 'rough footing' case is modelled in all cases. The

normalized bearing capacity $\frac{p}{\gamma B}$ is plotted against the 'shear strength' of clay $\frac{c}{\gamma B}$ as shown in Figure 3.26. Figure 3.26 indicates that the obtained lower and upper bound solutions agree well with results from Michalowski & Shi. It is also worth also commenting on the effect of footing roughness. As discussed by Chen (1975), approximate estimates for the frictional bearing capacity factor N_γ are reduced by a factor of around two when the footing is taken as smooth instead of rough. For the problem under investigation, it is expected that this parameter will have the most influence when most of the failure mechanism lies inside the sand layer and there is no surcharge. When the angle of friction is large (e.g. 40° or 45°), the failure mechanism becomes deeper and wider and the effect of the footing rough-ness diminishes as the influence of the clay dominates. For the results presented here, the footing roughness has a negligible influence on the strip footing bearing capacity. Figures 3.27 to 3.30 show the velocity field for a sand layer over clay with different strengths. As can be seen in these figures, the deformation of the sand layer increases when the shear strength of the clay increases.
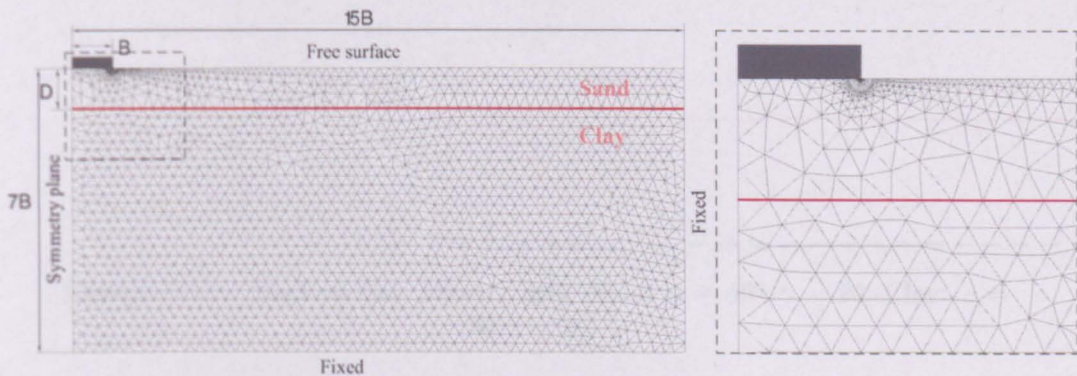
FIGURE 3.25: Finite element mesh for sand over clay

3.8.3 Comparison between constant strain element and linear strain element for the upper-bound solution

This section compares the N_γ solutions obtained when using constant strain (CST) elements and linear strain (LST) elements . Solutions are obtained using a uniform
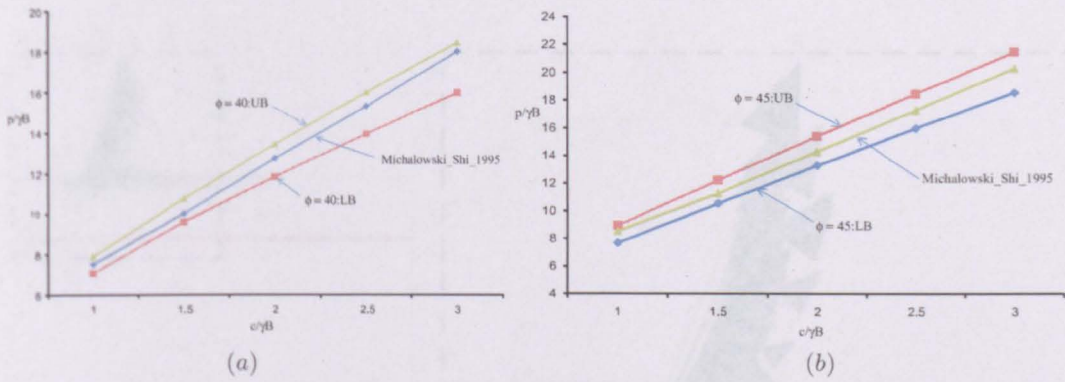
FIGURE 3.26: Dimensionless limit pressure on Sand-Clay foundation soil: (a) $\phi = 40^o$, (b) $\phi = 45^o$)
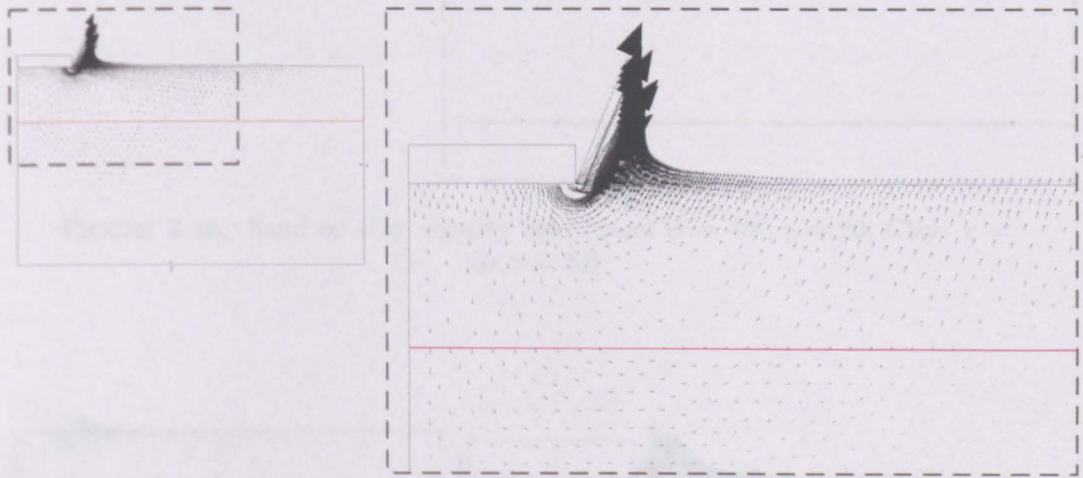
FIGURE 3.27: Sand on clay velocity field (Sand $\phi = 40^o, \gamma = 20$, Clay: $c = 30, \gamma = 20$)

mesh comprising 6000 elements and discontinuities. As illustrated in table 3.3, with the use of 6-noded elements, the use of LST leads to much improved results. e.g. for $\phi = 35^o$, the CST element error is over 18%, while the error when LST elements are used is less than 7%.
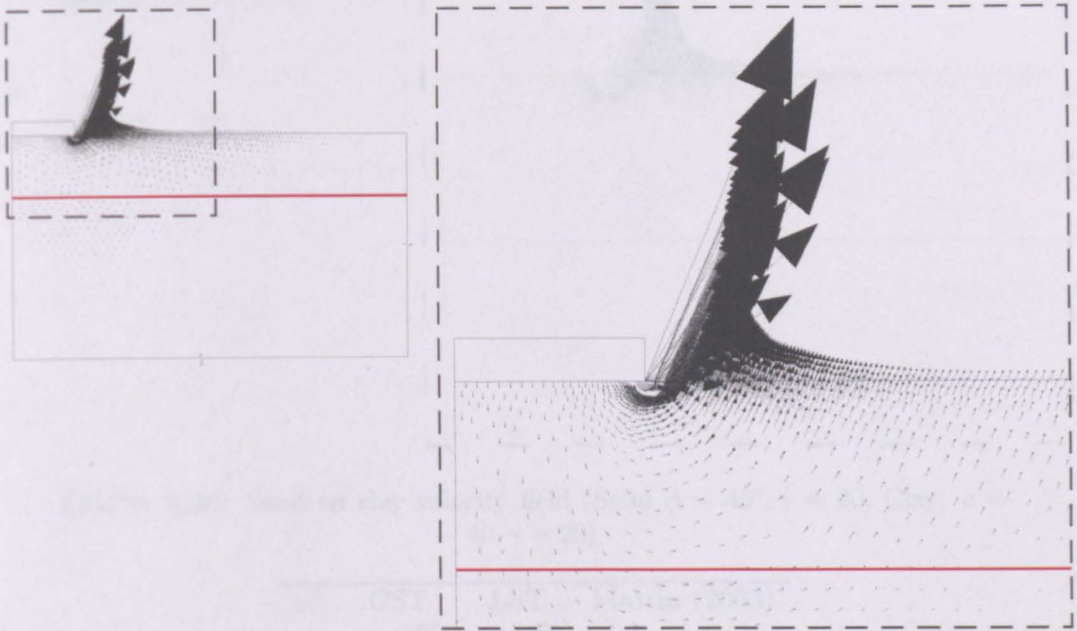
FIGURE 3.28: Sand on clay velocity field (Sand $\phi = 40^o, \gamma = 20$, Clay: $c = 60, \gamma = 20$)
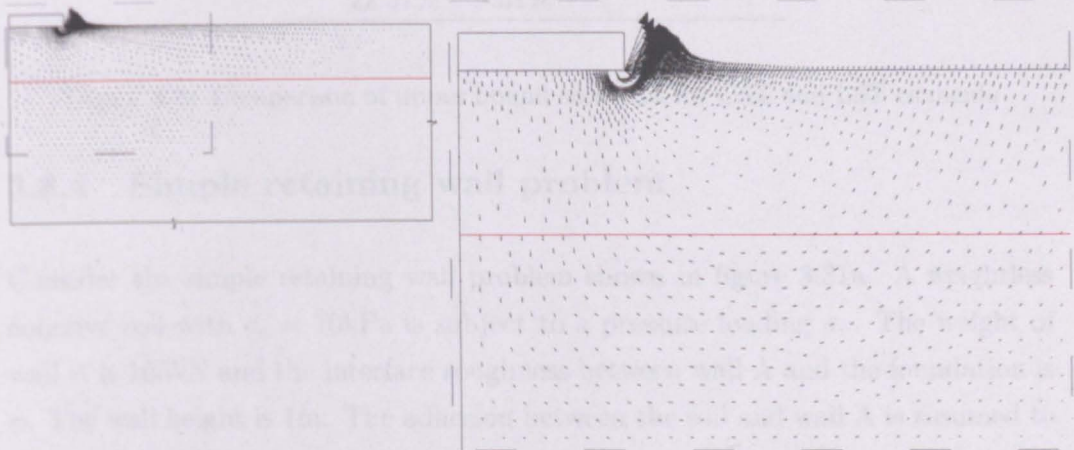
FIGURE 3.29: Sand on clay velocity field (Sand $\phi = 45^o, \gamma = 20$, Clay: $c = 20, \gamma = 20$)

FIGURE 3.30: Sand on clay velocity field (Sand $\phi = 45^\circ, \gamma = 20$, Clay: $c = 40, \gamma = 20$)

ϕ°	CST error%	LST error%	Martin (2003)
25	3.652	3.58	3.461
	5.23%	3.4%	
35	21.5	18.75	17.58
	18.23%	6.65%	
40	55.78	47.3	43.19
	22.57%	9.51%	

TABLE 3.3: Comparison of upper bound solutions for CST and LST elements

3.8.4 Simple retaining wall problem

Consider the simple retaining wall problem shown in figure 3.31a. A weightless cohesive soil with $c_u = 10$kPa is subject to a pressure loading σ_v. The weight of wall A is 105kN and the interface roughness between wall A and the foundation is ϕ. The wall height is 1m. The adhesion between the soil and wall A is assumed to be $c_w = 0.5c_u$. The problem is to find the σ_v that causes the structure to collapse. Table 3.4 shows the results of σ_v for various ϕ and c_w. Analytical results obtained using a limit equilibrium method are provided by Powrie (1997). The active limit to the horizontal total stress for active retaining wall with soil-wall adhesion is
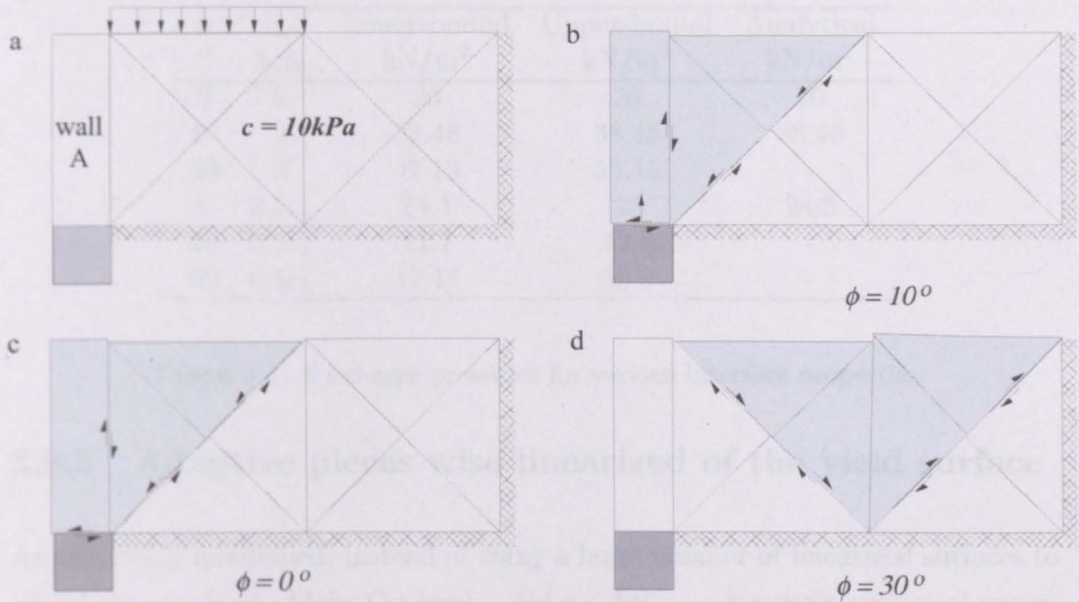
FIGURE 3.31: Simple retaining wall problem

given by:

$$\sigma_v - \sigma_h = 2c_u\sqrt{(1 + c_w/c_u)} \tag{3.81}$$

and

$$\sigma_v - \sigma_h = 2c_u \tag{3.82}$$

for the case when soil-wall adhesion is not taken into account. Figure 3.31b,c,d show the collapse mechanism for cases $\phi = 10, 0, 30°$ respectively. In the case $\phi = 0, c_w = 0$, applying equation 3.82 with $\sigma_h = 0$ gives $\sigma_v = 20$. In the case where $\phi = 10, c_w = 0$, the mechanism involves the sliding of wall A on the interface. The frictional interface between wall A and the foundation provides horizontal pressure which will act to resist collapse. The magnitude of horizontal pressure is $\sigma_h = 1 \times 105 \times \tan(10) = 18.48\text{kN/m}^2$ so that $\sigma_v = \sigma_h + 2c_u = 38.48\text{kN/m}^2$. For the case $\phi = 0, c_w = 0.5c_u$, applying equation 3.81 with $\sigma_h = 0$ and $c_w = 5$, the analytical result is 24.5kN/m^2. Figure 3.31d shows the mechanism which involves failure of the soil only. It is indeed as expected since the horizontal pressure is large enough to resist the load that causes the soil failure.

ϕ ^{o}	c_w kPa	Lower-bound kN/m^2	Upper-bound kN/m^2	Analytical kN/m^2
0	0	20	20	20
10	0	38.48	38.48	38.48
30	0	47.13	55.15	-
0	$0.5c_u$	24.1	25	24.5
10	$0.5c_u$	41.7	42.6	-
30	$0.5c_u$	47.14	55.9	-

TABLE 3.4: Surcharge pressures for various interface properties

3.8.5 Adaptive pieces wise linearized of the yield surface

As previously mentioned, instead of using a large number of linearized surfaces to model the non-linear Mohr-Coulomb yield condition, a heuristic numerical procedure is adopted. This is described below:

- Input problem data

- Solve problem using very low number of linearized surfaces $p = 3$

- Check the yield condition.

- Add additional constraint if the stress point lies outside the true yield surface.

- Terminate if the yield is satisfied everywhere in the domain.

Table 3.5 shows the ultimate surcharge pressure obtained for a frictionless soil with a finite element mesh comprising 4327 linear stress elements (as in figure 3.19). As shown in the table, when using the procedure the total number of constraints at iteration 10 is about 60% less than the number of constraints when $p = 15$, and 80% less when $p = 32$. When $p = 48$, the number of linearized surface is so great that there is not enough memory to solve the LP problem. Table 3.5 also shows that adaptive result was closer to the exact value $((2 + \pi)c)$ compared to the case when $p = 32$. This clearly demonstrates that this heuristic approach allows much larger problems to be solved. However, the time taken to solve a problem using

	Adaptive approach			Traditional approach		
Iter	Surcharge kN/m^2	No of added cons (No of constraints)	Total time(s)	p	Surcharge kN/m^2	No of constraints	Total time(s)
1	69.2953	- (73559)	22.87	15	44.372	229331	37.18
2	51.7095	7966 (81525)	46.38	18	46.589	268274	30.87
3	50.4409	1587(83112)	68.94	24	48.53	346160	35.81
4	50.4295	782 (83894)	91.47	32	50.01	450008	41.85
5	50.4291	411 (84305)	114.48	48	-	-	-
6	50.4289	235 (84540)	138.05				
7	50.4288	59 (84599)	160.65				
8	50.4288	13 (84612)	183.35				
9	50.4288	0 (84612)	205.77				

TABLE 3.5: Comparing adaptive approach to traditional approach for a frictionless soil

the adaptive approach might be longer than when using the traditional approach. Figure 3.32 shows the ultimate surcharge pressure for 1m footing width obtained when using the adaptive procedure for different soil types. The results indicate that the final solution is obtained very quickly, but that more iterations are needed to assure that there is no stress point that violates yield.

3.9 Conclusions

In this chapter, a two-dimensional computational limit analysis procedure has been developed for soil-arch interaction problems. Use of quadratic displacement elements with discontinuities to model the soil improves upper bound predictions, and reasonably close bounds on the theoretical 'exact' collapse load have been obtained. The adaptive piecewise linearization of the yield surface is found to be capable of reducing the size of the underlying LP problem, thus permitting larger problems to be solved. For the simple retaining wall problem considered, results from the numerical method developed were found to be in good agreement with available analytical solutions. The above upper and lower bound model will
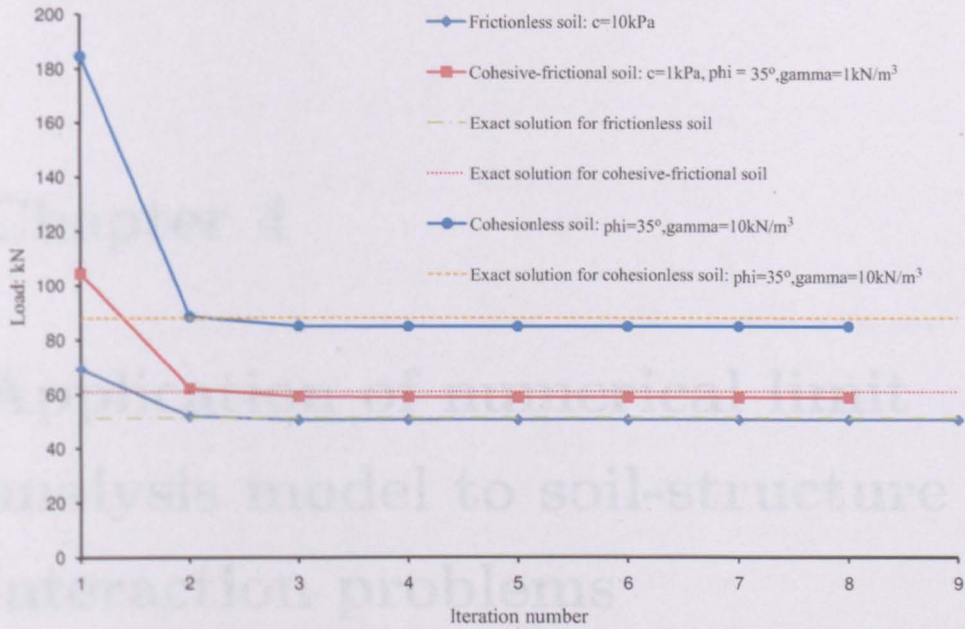
FIGURE 3.32: Adaptive approach: Load converge vs iteration for different type
of soil for 1m footing width

be used to analyse a series of bridges recently load tested to collapse at Salford
University.

Chapter 4

Application of numerical limit analysis model to soil-structure interaction problems

4.1 Introduction

Finite element limit analysis is becoming an established computational means by which upper and lower-bound strength estimates can be rapidly obtained for problems with complex geometry and/or loading and boundary conditions. Advantages are that only soil strength parameters and details of the mesh geometry are required in order to obtain solutions, which also have clear status (in contrast to the solutions obtained using incremental elastic-plastic methods for example). Whilst several finite element limit analysis studies of soil-structure interaction problems are already described in the literature (e.g. for bearing capacity and anchor pullout problems), interest has typically focussed on soil performance only. For particular classes of problems it is desirable to perform a coupled analysis of the soil and adjacent structural elements. This study describes how such problems can be formulated and explores some of the challenges and issues involved, including that of relative soil and structure strength mobilization. Illustrative example problems

	$c\ (kN/m^2)$	ϕ (degrees)	$\gamma\ (kN/m^3)$
Soil	5	40	14
Masonry	0	31	20
Soil-Masonry	0	20	-

TABLE 4.1: Material properties

are described, including backfilled masonry arch bridge and retaining wall problems, and results are compared with those from simple analyses and large scale experiments.

Theoretical developments presented in Chapter 3 have been implemented in computer software **fem** to carry out the lower and upper-bound limit analysis. **fem** was written using the well known C++ object oriented language; further details can be found in Appendix B. With the aim that the developed numerical model could be used in future commercial software, C++ seems to be an obvious choice rather than Matlab. However, it means that the level of understanding of the C++ language must be high to be able to work in a software development team. Unlike the usual finite element method, where many free C++ libraries can be incorporated, there is no C++ library for FELA. The author has therefore spent a significant period of time developing **fem**.

The basic procedure is briefly described as follows: Finite element meshes are generated using a third party mesh generator, Gid9. Mesh data from Gid9 is output to a text file and then read into **fem**. In **fem** boundary, equilibrium, yield or flow rule conditions are imposed, leading to a mathematical programming problem formulation. The optimization problem is then solved by using a third party LP solver, Mosek. Finally the solution is interpreted using software such as AutoCad and Microsoft Excel.
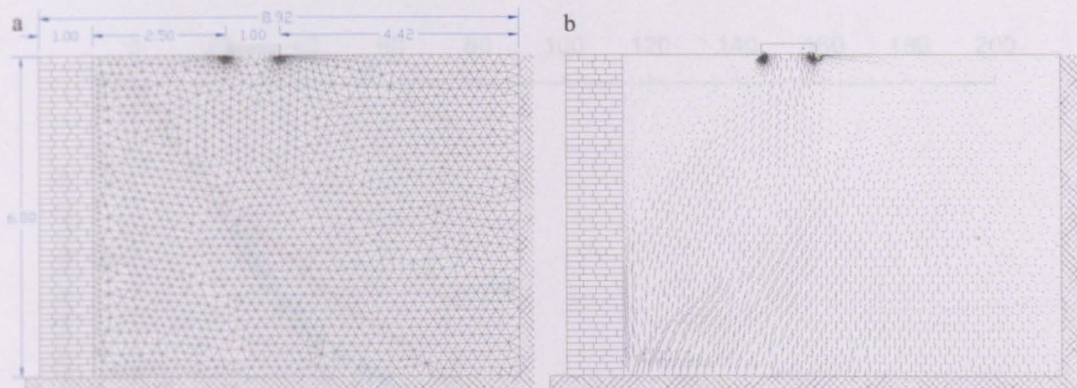
FIGURE 4.1: Retaining wall geometry (a) and Maximum compressive stress vectors (b)
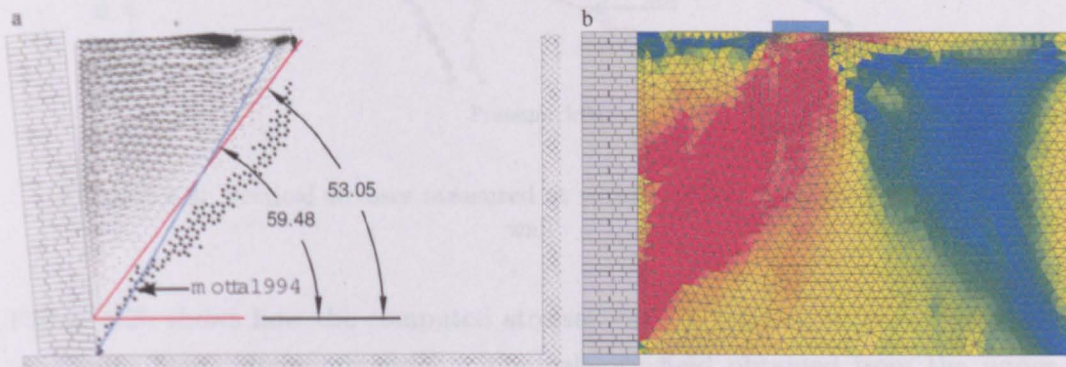
FIGURE 4.2: Soil velocity field and wall deformation (a) and Variation in stresses in relation to the yield stress (b)

4.2 Analysis of a brickwork retaining wall

This example illustrates application of the model to the analysis of a masonry block retaining wall retaining soil with a discrete surface load. Material properties are provided in table 4.1 and the geometry is shown in figure 4.1a. Lower and upper-bound predictions of the surface load required to cause collapse were 58.6kN/m and 65.4kN/m respectively. To obtain these values the mesh was manually refined around the base of the surface surcharge, though further improved predictions could be achieved with a finer mesh (for this example a single relatively coarse mesh comprising 3831 elements was used for both lower and upper bound analyses).
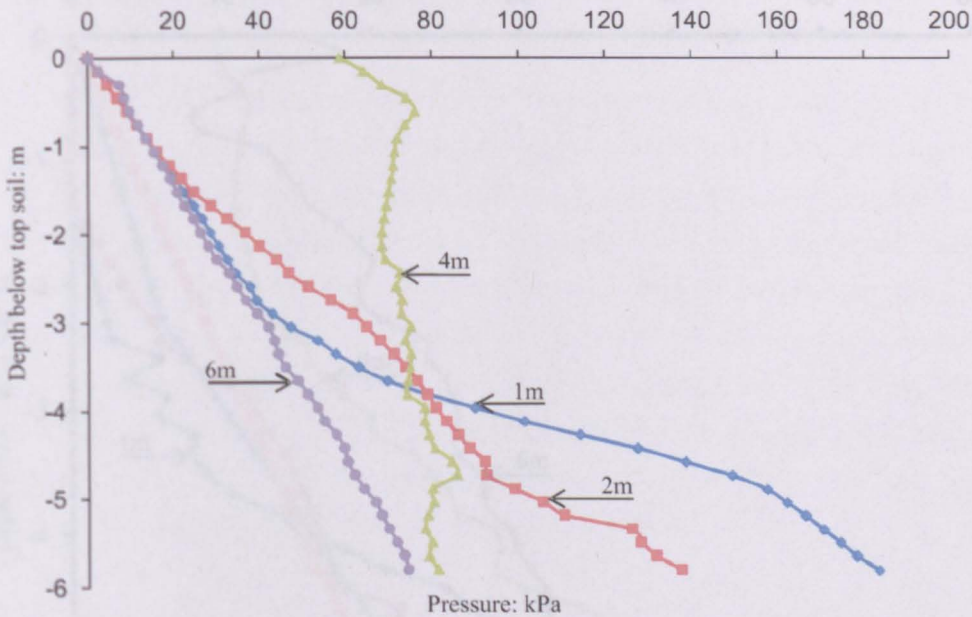
FIGURE 4.3: Vertical stresses measured at various offsets from the front of the wall

Figure 4.2b shows how the computed stresses vary in relation to the yield stress (red areas being closest to yield). The velocity field obtained from the upper bound analysis shown in figure 4.2a indicates the presence of a crack between the wall and soil and also that the wall fails by rotating near its base. In figure 4.3 the predicted vertical stresses 6m behind the wall vary approximately linearly with depth, the values being close to γh as expected. In contrast, the vertical stresses immediately behind the wall are significantly above this level below a depth of approx 2.5m. The low horizontal stresses 1m behind the wall in figure 4.4 indicate the potential presence of cracking down to a depth of ≈ 1.6m. The wall fails because of the increasing horizontal stresses below this depth, acting to overturn the wall.

No directly comparable benchmarks are available in the literature for this type of problem; however the horizontal stress distribution on the wall due to the surface load can be compared with that derived using a procedure due to Pappin et al.
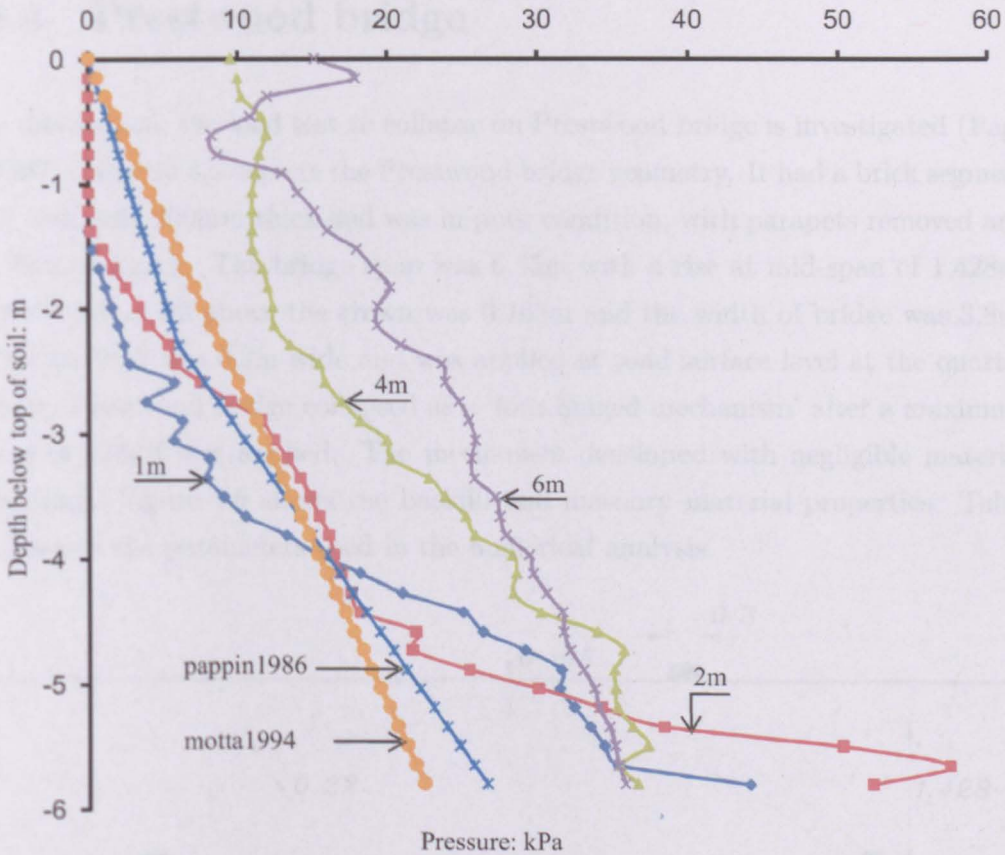
FIGURE 4.4: Horizontal stresses measured at various offsets from the front of the wall

(1986) and Motta (1994). It is evident from figure 4.4 that the results do not correlate well. In figure 4.2, the critical plane predicted by the upper bound method is approx. $53.1°$ compared with $59.48°$ suggested by Motta. This is probably reasonable since in Motta's model the wall is assumed rigid and the critical plane is derived from the bottom right of the wall. Note that for this example it has been implicitly assumed that peak soil and structural strength will be mobilized simultaneously; this may not always hold true, as will be demonstrated in the following examples.

4.3   Prestwood bridge

In this section, the load test to collapse on Prestwood bridge is investigated (Page (1987)). Figure 4.5 depicts the Prestwood bridge geometry. It had a brick segmental arch only 200mm thick and was in poor condition, with parapets removed and a distorted arch. The bridge span was 6.55m with a rise at mid-span of 1.428m. The depth of fill above the crown was 0.165m and the width of bridge was 3.8m. The live load was 0.3m wide and was applied at road surface level at the quarter point. Prestwood bridge collapsed as a 'four hinged mechanism' after a maximum load of 228kN was applied. The mechanism developed with negligible material crushing. Figure 4.6 shows the backfill and masonry material properties. Table 4.2 shows the parameters used in the numerical analysis.
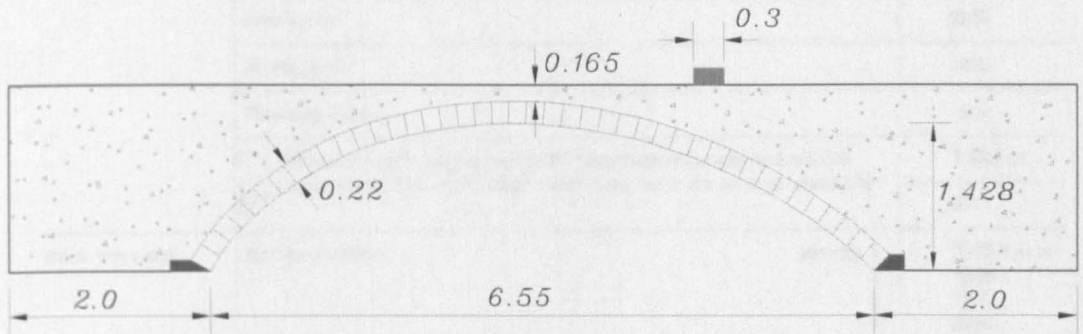
FIGURE 4.5: Prestwood bridge geometry

	$c(kN/m^2)$	$\phi\,(o)$	$\gamma\,(kN/m^3)$
Soil	7	37	20
Masonry	0	31	20

TABLE 4.2: Material properties of Prestwood bridge

Figure 4.7 shows the finite element mesh used for the numerical analysis. The mesh comprised 5096 triangular elements and 42 rigid-block elements. The same mesh was used for both upper and lower bound analyses. In this test, there is also no information on soil-arch interface properties, however, taking $\delta/\phi = 2/3$, the predicted collapsed load given by the lower and upper bound solutions are

TABLE 4

Prestwood bridge: measurements on arch and fill samples

Sample	Measurement		Result
Fill from west abutment (sample 1)	Maximum dry density	(From compaction tests on reconstituted samples)	1.76 Mg/m³
	Optimum moisture content		13%
	In-situ moisture content		6.0%
Fill from east abutment (sample 2)	Maximum dry density	(From compaction tests on reconstituted samples)	1.80 Mg/m³
	Optimum moisture content		11.5%
	In-situ moisture content		10.5%
	Liquid limit		23%
	Plastic limit		14%
	Plasticity index		9%
	C' (Shear strength parameters from consolidated undrained triaxial compression test (multistage) with measurement of pore pressure)		7 kN/m²
	Ø'		37°
Brick from arch	Natural density: sample 1 2 3 4 5		2010 Kg/m³ 1940 1960 2070 1770
	Specific gravity (sample 1)		2.68
	Secant modulus	(From 54.5 mm diameter and 129.2 mm long core)	2200 N/mm²
	Crushing strength		7.7 N/mm²
Brick and mortar block (2 bricks mortared together on their top and bottom faces)	Secant modulus		4140 N/mm²
	Crushing strength		4.5N/mm²

FIGURE 4.6: Prestwood bridge material properties (Page 1987)
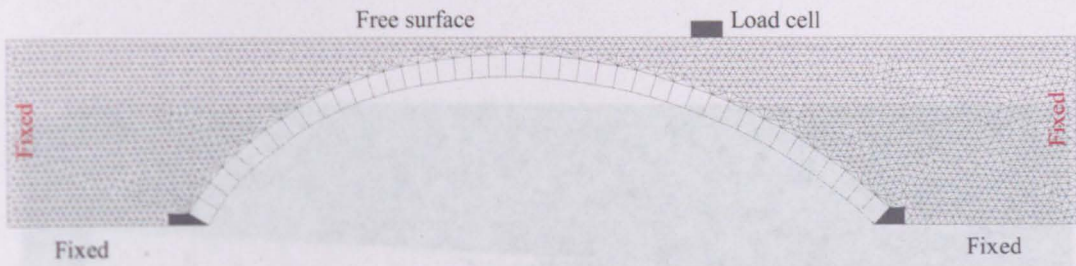
FIGURE 4.7: Finite element mesh of Prestwood bridge
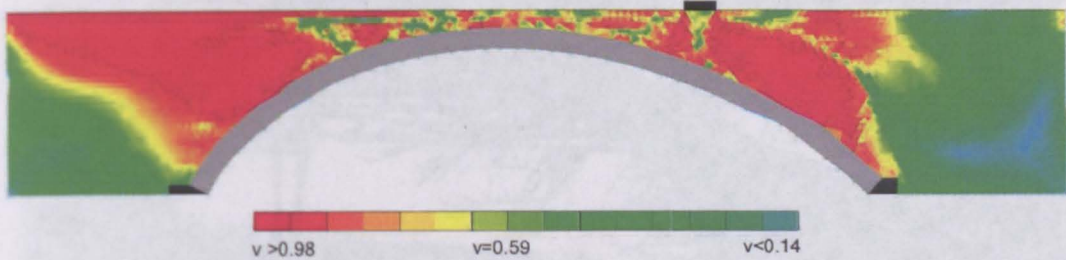
FIGURE 4.8: Prestwood Bridge: variation in maximum shear stress relative to the yield stress
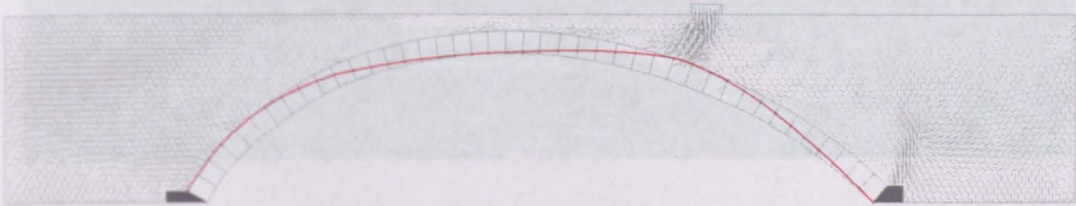
FIGURE 4.9: Prestwood Bridge: maximum compressive principal stress vectors

195kN and 236kN respectively. The model predicted the arch will fail in a four hinges mechanism as shown on figure 4.11, and the predicted hinge locations are found to be similar to those observed in the test (see figure 4.10). Figure 4.12 shows the variation of the shear strain rate predicted by the upper bound. In this example, the predicted loads provide 'good' bounds on the actual collapse load of 228kN. Although the predicted collapse load was close to the actual collapse load of the bridge, it should be noted that kentledge used as part of the collapse load test loading system were not modelled. Figure 4.13 shows that the kentledge is supported vertically above the arch springings and this may have influenced the strength of the bridge. There is also uncertainty about material properties
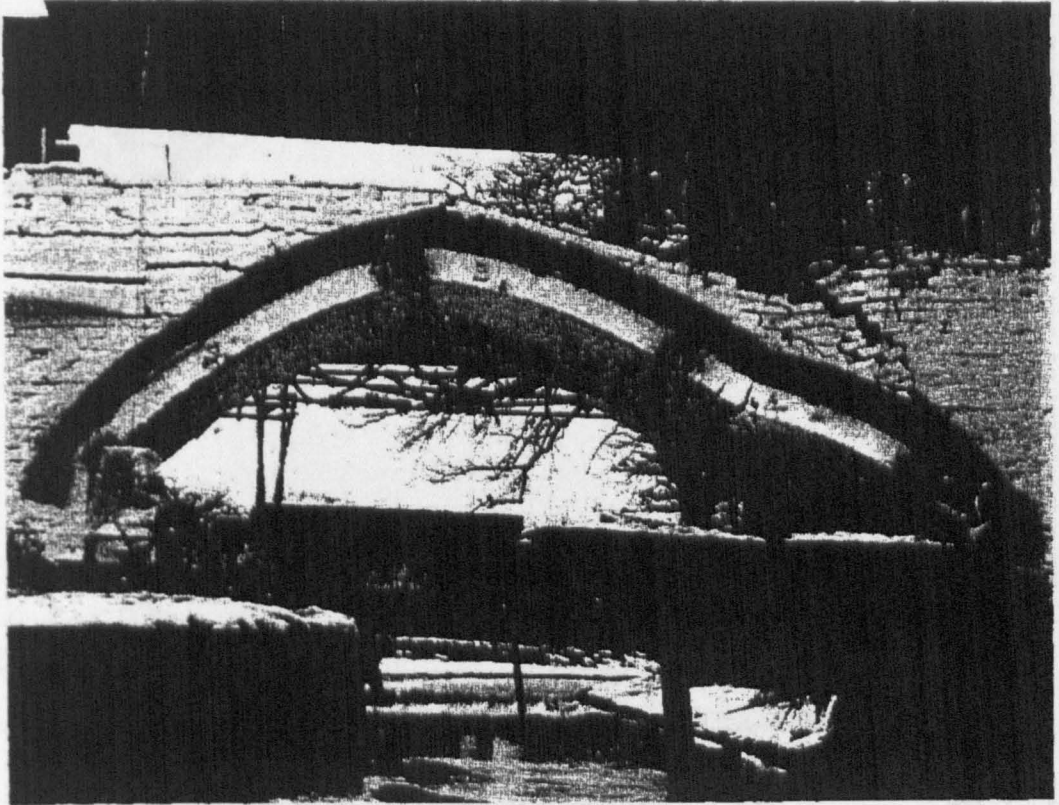
FIGURE 4.10: Prestwood bridge immediately before collapse (Page 1987)
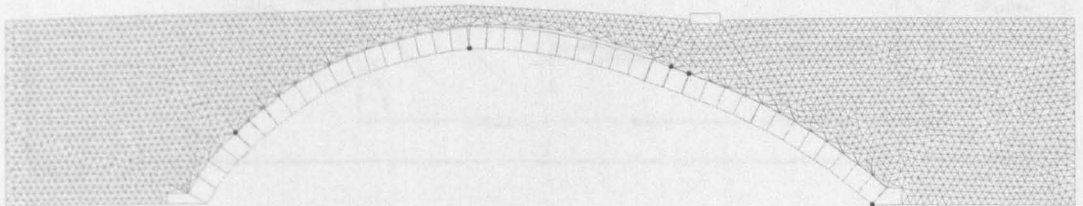
FIGURE 4.11: Prestwood Bridge: deformed shape of soil and arch
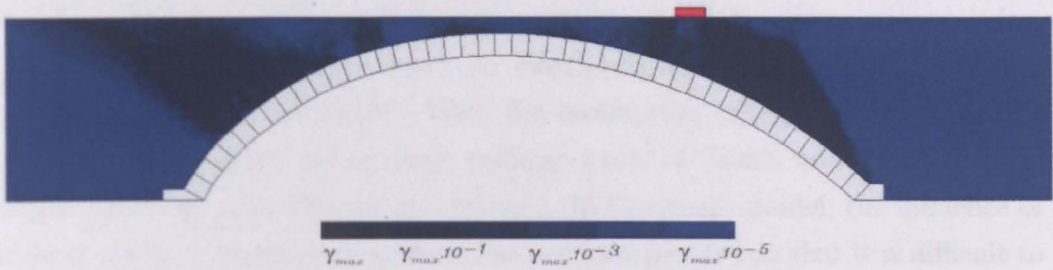
FIGURE 4.12: Prestwood Bridge: variation in shear strain rate
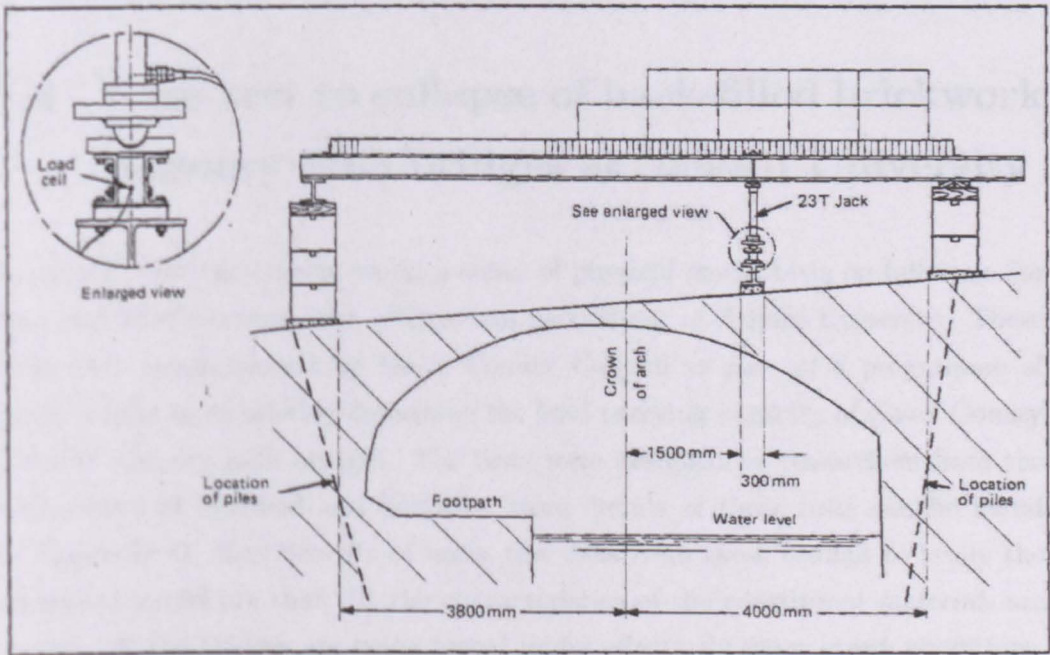
FIGURE 4.13: Prestwood Bridge: loading system (Page 1987)

used in the analysis. For example, in Cavicchi & Gambarotta (2005, 2007), the close bounds (210kN and 250kN) on the test load are only obtained when the soil strength is $c = 13, \phi = 37^o$ and the crushing strength of the masonry is low ($\sigma_c = 4.5$MPa). However, it has been mentioned in Page (1987) that masonry crushing failure was 'negligible'. With the assumption of high masonry crushing strength, the Cavicchi model gives collapse loads of 230kN and 280kN for the lower bound and upper bound respectively. In Cavicchi's model, the influence of the soil-masonry interface properties was not incorporated so that it is difficult to make direct comparison with results from the present model. Furthermore, here it was found that the FELA solution was very sensitive to mesh refinement, whilst in Cavicchi's papers, a very coarse mesh was used in the analysis. Therefore, it is concluded that it is not at present possible to make definitive statements about the predictive capability of FELA, based on the work of Cavicchi and the use of Prestwood bridge as a case study.

4.4 Load test to collapse of back-filled brickwork masonry arch bridges at Salford University

In parallel with the current work, a series of physical model tests on full-scale 3m span soil-filled masonry arch bridges was carried out at Salford University. These tests were commissioned by Essex County Council as part of a programme of work to help more reliably determine the load carrying capacity of Essex County Council masonry arch bridges. The tests were designed by researchers from the Universities of Sheffield and Salford. More details of these tests can be found in Appendix D. Key benefits of using test data from these bridges to verify the numerical model are that: (i) the characteristics of the constituent materials are known, (ii) the bridges are being tested under effectively plane strain conditions, replicating those in the model.

Bridge	A (m)	B (m)	Back-filled	Reinforcement (Yes/No)	Abutment (Fixed/Free)
Arch01	0.73	3.92	Limestone	No	Free
Arch02	1.93	2.72	Limestone/Clay	No	Free
Arch03	0.73	3.92	Limestone	No	Fixed
Arch04	1.34	3.31	Limestone/Hoggin	No	Free
Arch05	1.34	3.31	Limestone	Yes	Free
Arch06	1.34	3.31	Limestone/Clay	Yes	Free

TABLE 4.3: Details of Salford bridge geometry

4.4.1 Bridge geometry

The generic test geometry is shown in figure 4.14 and specific details for each test are given in table 4.3. Two bridges had near-road surface reinforcement comprising 10No. 3m long 100×50×10mm S275 parallel flange steel channels placed across the bridge width and centralized under the load. These replaced 50mm of fill. For all bridges, the loading beam was always located at the quarter span point. Bridges were backfilled with either limestone, limestone over clay, or limestone over hoggin and had either fixed or free abutments.
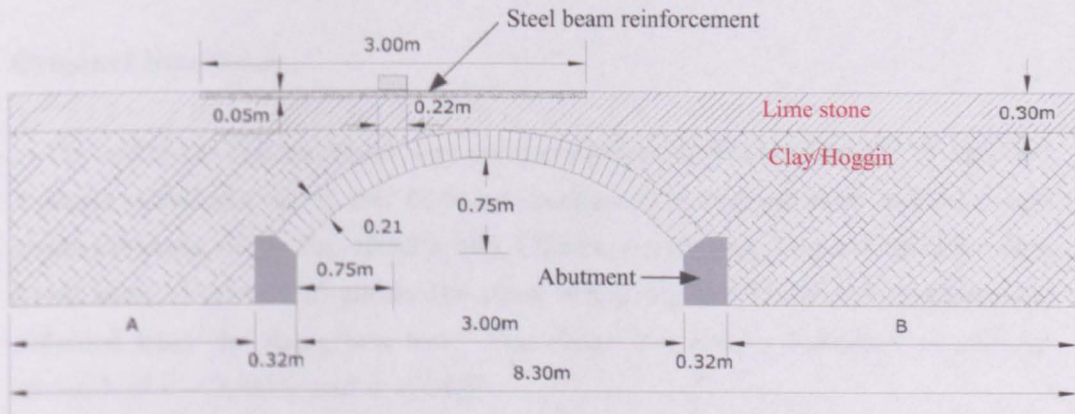
FIGURE 4.14: Salford Bridges: geometry

Material	Compressive Strength (N/mm^2)	Nominal Dimensions (mm)	Density (kg/m^3)
Class A engineering brick	154	215 x 102 x 65	2370
Mortar	1.9	-	1470-1570

TABLE 4.4: Masonry properties

4.4.2 Materials

Bricks and mortar

Properties of bricks used in the construction of the arch barrels are shown in table 4.4. The mortar $1 : 2 : 9$ (cement:lime:sand) mix by volume was used throughout the arch barrel. The mean properties as determined from five 100mm cubes are presented in table 4.4. The cubes were cured under the same conditions as the arch barrel.

Crushed limestone

In the arch tests the limestone was compacted to a typical density of 19.1kN/m^3. A series of 300mm shear box tests on compacted limestone were carried out at normal stresses of 25kPa, 100kPa and 175kPa, employing 3 repeat tests for each stress level. Figure 4.15 shows the shear stress against horizontal displacement obtained from the shear box test. The shear box results indicated an average strength of $c = 3.3$kPa and $\phi = 54.5^o$.

Clay

In the arch tests, the clay was compacted at an average moisture content of 12%. Since control over the moisture content uniformity was challenging for this type
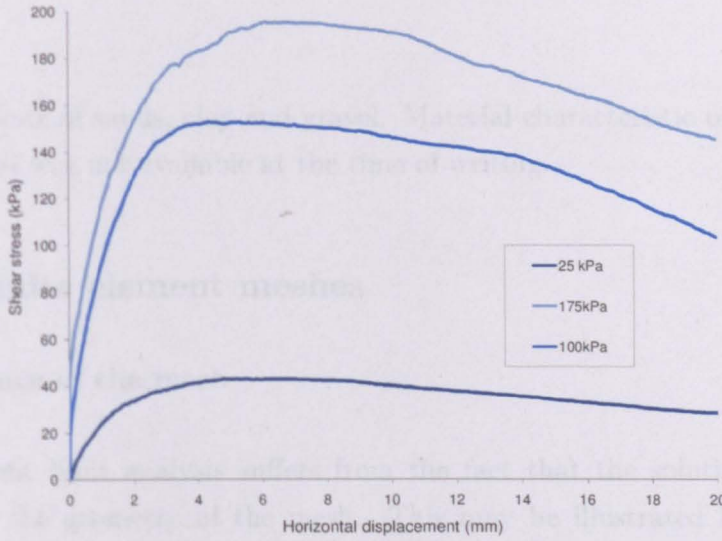
FIGURE 4.15: Crushed limestone shear box test: shear stress against horizontal displacement

of test, the actual placed moisture content varied $\sim \pm 2\%$ leading to a variation in soil strength measured on individual tube samples taken after the test. Figure 4.16 shows the typical range of triaxial test data obtained. The clay was compacted to an average density of 21.5kN/m^3.
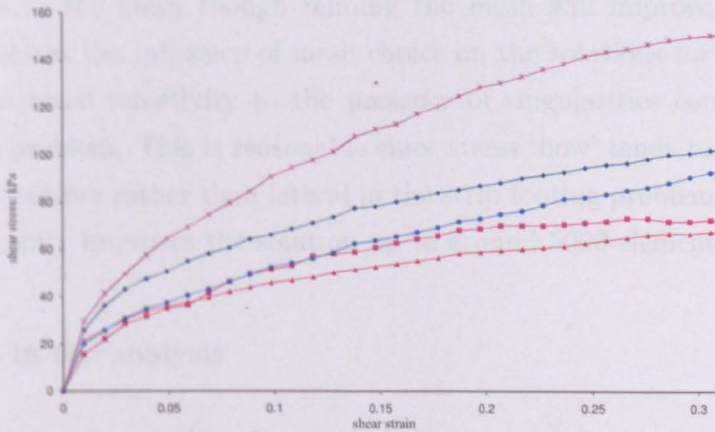
FIGURE 4.16: Clay triaxial test: shear stress against strain

Hoggin

Hoggin is a mix of sands, clay and gravel. Material characteristic of hoggin used in the Arch04 was not available at the time of writing.

4.4.3 Finite element meshes

The influence of the mesh

Finite element limit analysis suffers from the fact that the solutions are quite sensitive to the geometry of the mesh. This may be illustrated by examining mesh dependency when modelling a strip footing. From figures 4.17 and 4.18, it is evident that solutions obtained using the lower bound mesh without configuring it to account for the singularities present at the edges of the surface load are far from the exact solution. Close proximity to the exact solution is only achieved when meshes are both sufficiently fine and incorporate a manually constructed fan-like zone at the singularity. Without the fan-like zone, mesh refinement does not significantly improve the lower bound solution. Upper bound solutions are much less sensitive to the mesh though refining the mesh will improve the solution. Figure 4.19 shows the influence of mesh choice on the solutions for Arch01. This indicates a reduced sensitivity to the presence of singularities compared to the strip footing problem. This is reasonable since stress 'flow' tends to be downward for the arch problem rather than lateral in the strip footing problem. Refining the mesh significantly improves the solution up to around 5000 elements.

Mesh used in the analysis

Finite element meshes used in the analysis are shown in figures 4.20 to 4.24. The same meshes were used for the upper bound and lower bound analyses. For bridges without reinforcement, the meshes were manually refined around the base of the surface load and a relatively fine mesh was used around the arch barrel to capture the essential features of the soil-arch interaction. All meshes contain 48 rigid block
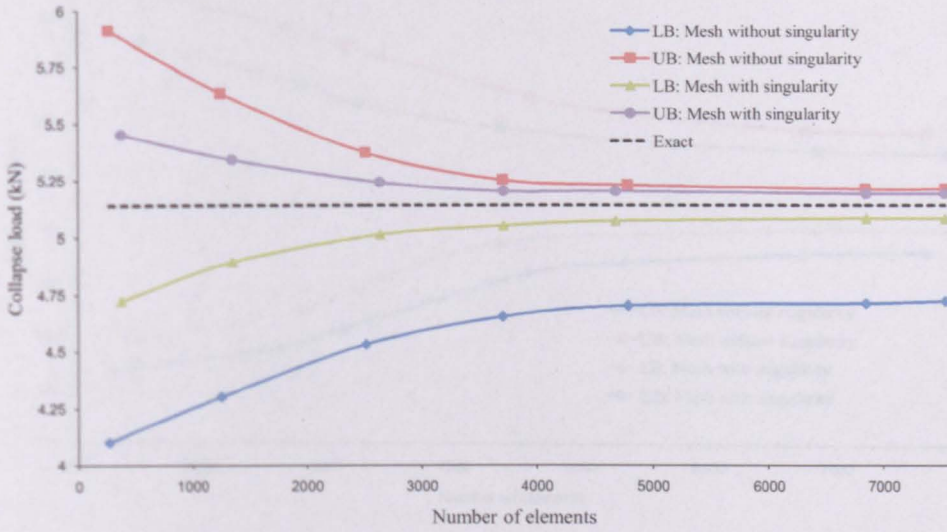
FIGURE 4.17: Ultimate limit load of a strip footing on cohesive soil for various type of meshes
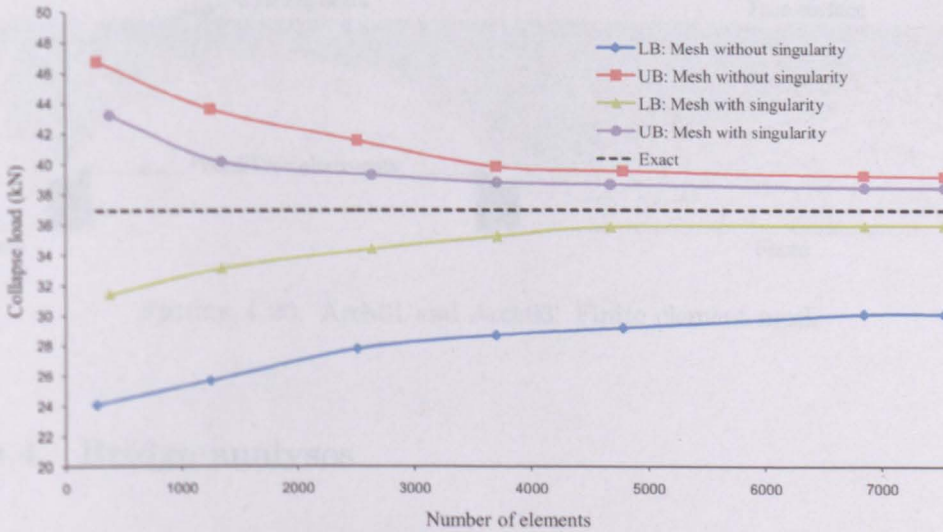
FIGURE 4.18: Ultimate limit load of a strip footing on cohesive-frictional soil for various type of meshes
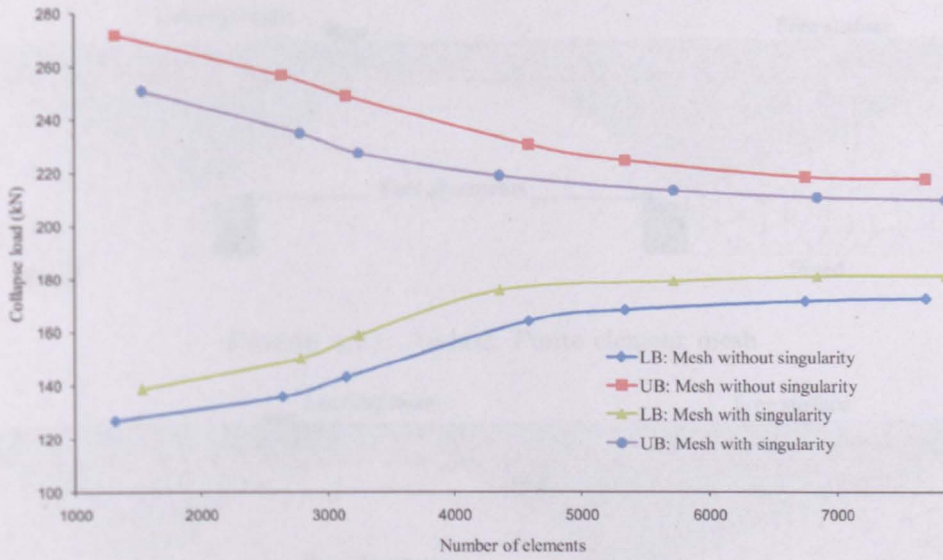
FIGURE 4.19: Ultimate limit load of Arch01 for various type of meshes

elements to represent the arch barrel. The number of triangle elements used to model the backfill varied for each test and is listed in table 4.5.
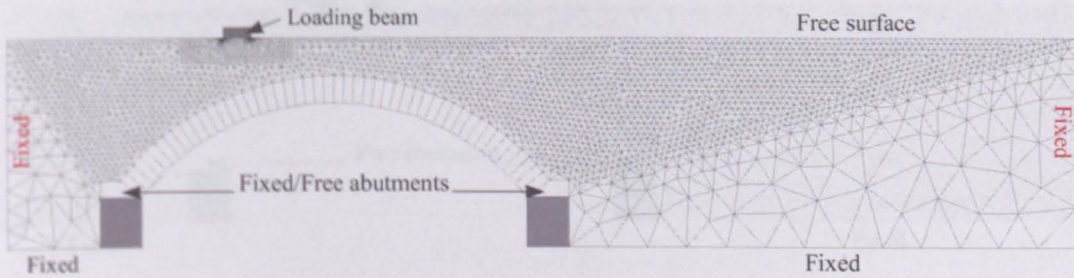
FIGURE 4.20: Arch01 and Arch03: Finite element mesh

4.4.4 Bridge analyses

For all bridges, the soil-masonry interface angle of friction δ, has not yet been measured experimentally and was initially taken as 1/3 soil strength. This is based on the Eurocode 7 recommendation of taking 2/3 ϕ_{cv} for the interface between sand/gravel and precast concrete, where ϕ_{cv} is the critical state angle of friction
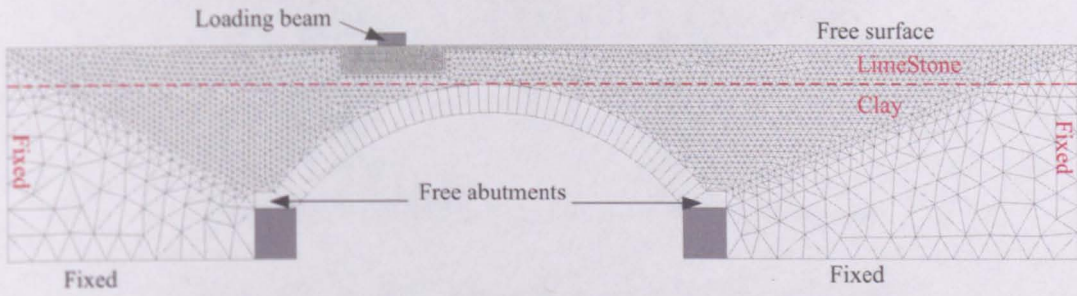
FIGURE 4.21: Arch02: Finite element mesh
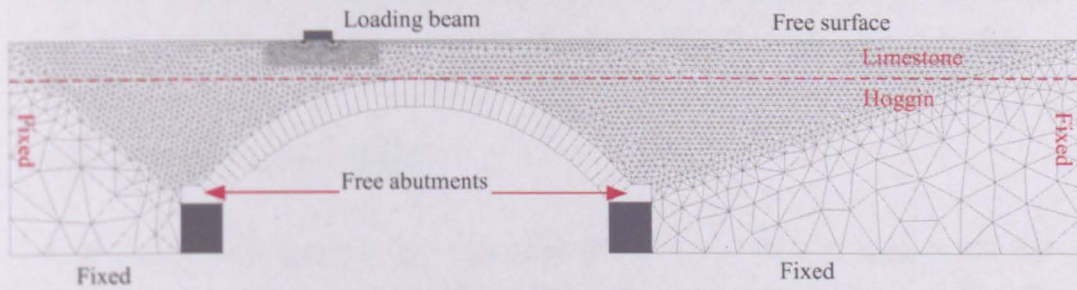
FIGURE 4.22: Arch04: Finite element mesh
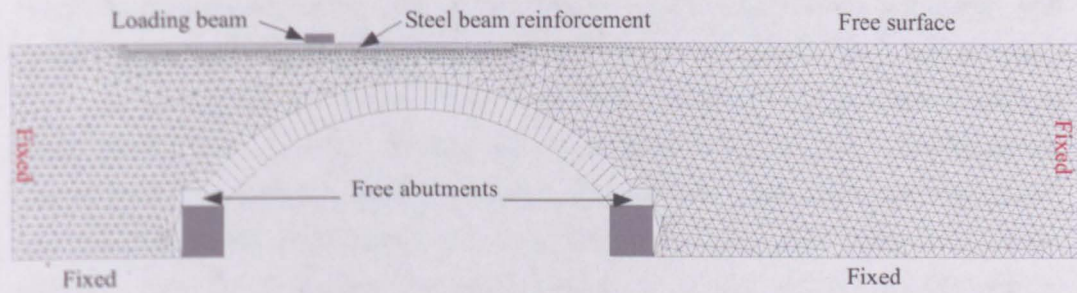
FIGURE 4.23: Arch05: Finite element mesh
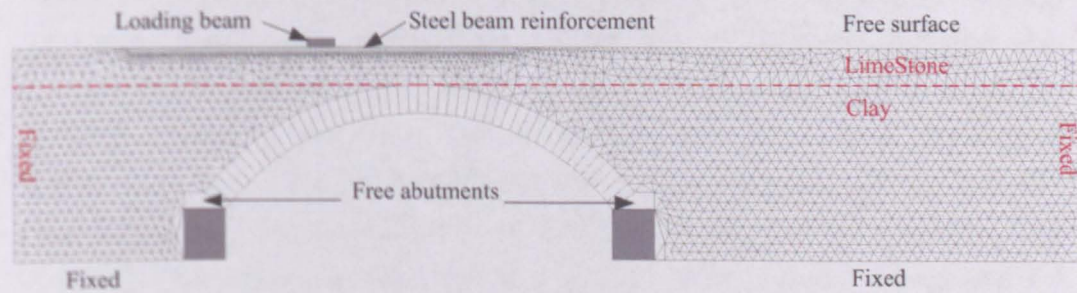
FIGURE 4.24: Arch06: Finite element mesh

Bridge	Number of triangle elements
Arch01 and Arch03	5895
Arch02	5957
Arch04	5974
Arch05	5417
Arch04 and Arch06	5390

TABLE 4.5: Number of triangle elements for the back-filled

of the soil. Although critical state values were not available from the shear box tests, they might be expected to be significantly lower than the peak strength.

Bridges Arch01 and Arch03

The numerical model described in previous chapters was used to analysis the Salford bridge test series. Bridges Arch01 and Arch03 have the same geometry, the only difference is that the abutments in Arch03 were fixed whereas in Arch01, the abutments were free to slide. The experimental collapse loads are 128kN and 145kN for Arch01 and Arch03 respectively. However, when the peak soil strength (i.e. $c = 3.3$kPa and $\phi = 54.5^o$) was used in the analysis, the predicted collapse loads are the same for these bridges as it is illustrated in table 4.6. Furthermore, the yielding stress (figure 4.29), the shear strain rate (figure 4.30) and the deformations (figure 4.32) are almost identical. Thus the numerical predictions indicate that abutment fixity does not alter bridge capacity nor deformation for this configuration. This clearly contrasts with the experimental evidence, where the bridge capacity was higher in the test with fixed abutments, and collapsed in a 4-hinge mechanism whilst Arch01 collapsed in a mode that also involved abutment sliding. The comparison of velocity fields given by PIV (Particle image velocimetry) and FELA in figure 4.33, shows that on the passive side of the arch, the slope of velocity vectors providing by the PIV (at the collapse state) are generally at 45°, whereas for the FELA, the velocity vectors are generally greater than 80°. This illustrates that using peak soil strength and/or an associated flow model may not be appropriate.

For Arch03, in both model and experiment, the arch collapsed in a classical 4 hinge mechanism, as shown in figure 4.32 (though it is evident that in some areas 'diffused' hinges form). Figure 4.29 indicates the presence of yielding soil (red shaded areas), both under the load and in the soil around the 'passive' right hand side of the arch, where the arch barrel sways into the soil mass. Figure 4.31 indicates that the stresses 'flow' in two 'streams', the right hand (short) stream focussing load directly onto the arch extrados, just to the right of the loading beam, and the left hand 'stream' taking the stresses almost parallel to the arch extrados towards the abutments. The position of the thrust line in figure 4.31 (i.e. alternately touching the intrados and extrados) indicates that the arch is at the point of collapse. The initial predicted lower-bound and upper-bound load carrying capacities were 170kN and 231kN respectively, significantly greater than the experimentally recorded peak load. Three main factors can be considered as contributing to this gross over-prediction:

- Soil/arch interface properties were estimated rather than measured.

- The loading beam friction was assumed to be smooth as a measured value was unavailable.

- Large displacements of an arch cause it to lose strength (see e.g Gilbert (1997)), whereas conversely significant soil strength is only mobilized once structural displacements become large.

To identify the relative significance of each of the first two parameters, a parametric study was performed. Taking the parameter set described previously as the benchmark, the influence of varying individual parameters was investigated. The effect of the ratio δ/ϕ (plotted as F in figure 4.25) , where δ is the soil-arch interface friction can be seen to have a very significant effect on predicted load carrying capacity. A close match between experiment and model is only achieved if an almost perfectly smooth interface is assumed, which does not seem reasonable. Conversely, taking $F = 0.33$ gives a high predicted capacity for full soil mobilization. It was found that the soil-loading beam interface friction has a negligible

Bridge	Lower-bound	Upper-bound	Experiment
Arch01	170	231	128
Arch02	80	98	90
Arch03	170	231	145
Arch05	624	842	360
Arch06	271	287	280

TABLE 4.6: Predicted collapse loads (kN) of Salford bridge tests

effect on the predicted bridge capacity, in contrast to the considerable influence of base friction in the case of ordinary foundation footings. This appears logical in that most soil movement and transfer of load is directly downwards in the arch problem, rather than laterally in the case of a foundation footing problem.
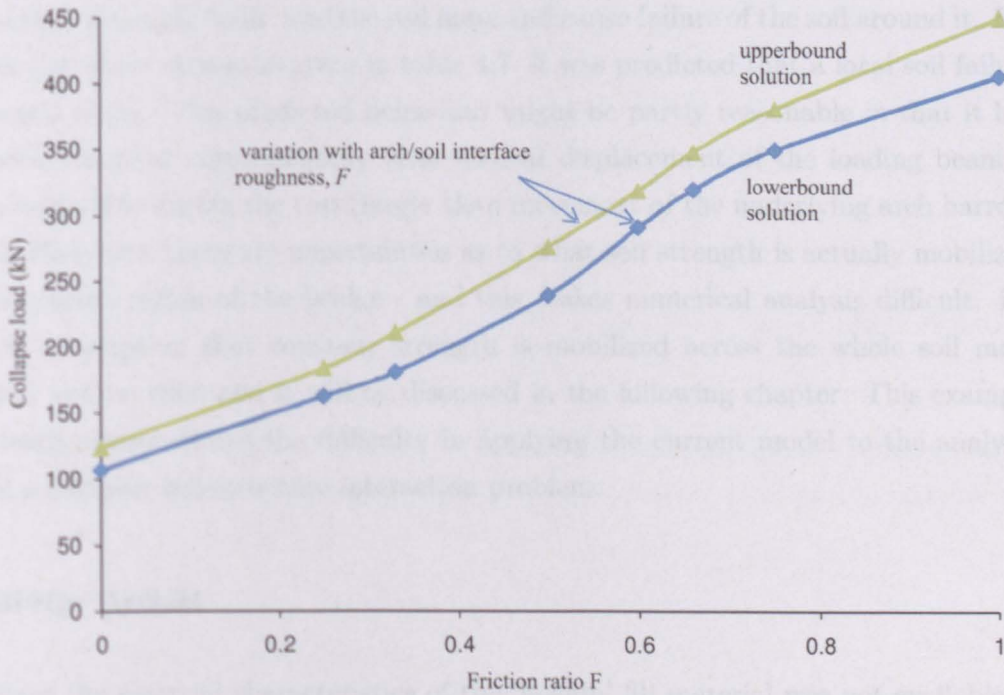
FIGURE 4.25: Arch03: variation in collapse load with different soil/arch interface properties

Bridge Arch02

Determining the shear strength of the clay is rather difficult since the data obtained from triaxial tests were quite variable, as shown on figure 4.16. In order to evaluate the effect of the clay shear strength on predicted behaviour, various clay shear strengths, ranging from $c = 30$ to $c = 100kPa$ have been used in the model. Table 4.7 shows the predicted bridge bearing capacity, illustrating that with a cohesion 30kPa, the predicted collapse load is closed to that observed experimentally (80kN and 98kN for the lower and upper-bound analyses respectively). However, as can be seen on figure 4.32, the numerical model predicted a localized failure in the soil only. Figure 4.29 also shows that the soil within the top layer appears to be yielding almost everywhere, an unexpected result. This indicates that the loading beam will simply 'sink' into the soil mass and cause failure of the soil around it. For all clay shear strengths given in table 4.7, it was predicted that a local soil failure would occur. This predicted behaviour might be partly reasonable in that it has been observed experimentally that vertical displacement of the loading beam is considerable during the test (larger than movement of the underlying arch barrel). Furthermore, there are uncertainties as to what soil strength is actually mobilized in a given region of the bridge - and this makes numerical analysis difficult. i.e. the assumption that constant strength is mobilized across the whole soil mass may not be valid and it will be discussed in the following chapter. This example clearly demonstrates the difficulty in applying the current model to the analysis of a complex soil-structure interaction problem.

Bridge Arch04

Since the material characteristics of the 'hoggin' fill material was not available, a parametric study on the contribution of the soil friction and cohesion on bridge carrying capacity was undertaken. Table 4.8 and 4.9 show the predicted collapse loads for various soil angles of friction and cohesion. It is found that when $\phi = 48^o$, the predicted collapse load is close to the experiment. Table 4.9 shows that when $c = 60kPa$, the collapse load given by the lower bound and upper bound analyses

Cohesion (kPa)	Lower-bound	Upper-bound	Experiment
30	80	98	
40	96	118	
50	110	140	
60	123	159	90
70	136	178	
80	148	195	
90	159	212	
100	170	230	

TABLE 4.7: Predicted collapse loads of Arch02 for various clay shear strengths

$\phi°$	Lower-bound	Upper-bound	Experiment
20	54	63	
25	65	77	
30	74	86	
35	90	104	
40	108	127	
45	126	149	
48	139	165	145
50	148	178	
55	171	210	

TABLE 4.8: Predicted collapse loads (kN) of Arch04 for various angles of soil friction

are 131kN and 176kN, which are quite close to the test load. However, as for Arch02, the FELA model predicted local footing failure when purely cohesive soil was present.

Bridges Arch05 and Arch06

The Arch05 and Arch06 tests in Salford University are a back-filled crushed limestone and limestone over clay with near-road surface reinforcement as described in section 4.4.1. It was originally envisaged that the reinforced concrete beam model developed in Chapter 3 would be used for these tests; however in the event a steel beam was used in the experiments. However, it can be argued that the

Cohesion (kPa)	Lower-bound	Upper-bound	Experiment
30	82	107	
35	92	120	
40	101	133	
50	116.7	157	
60	131	176	145
70	144	190	
80	157	210	

TABLE 4.9: Predicted collapse loads (kN) of Arch04 for various soil cohesion values

ϕ°	Lower-bound	Upper-bound	Experiment
20	179	214.8	
25	200	240	
30	232	278	
35	272	354	
40	335	436	375
45	420	567	
50	510	689	
54.5	624	842	

TABLE 4.10: Predicted collapse loads (kN) of Arch05 for various limestone angles of friction

Cohesion (kPa)	Lower-bound	Upper-bound	Experiment
30	271	287	280
35	292	309	
40	313	335	
50	355	375	
60	395	427	
70	435	465	
80	473	502	

TABLE 4.11: Predicted collapse loads (kN) of Arch06 for various clay strengths

	Arch05		Arch06	
Mp	Lower-bound	Upper-bound	Lower-bound	Upper-bound
3.0	514	694	233	247
4.0	570	770	253	268
4.8	624	842	271	287
5.5	672	907	286	303
6.0	706	953	297	315

TABLE 4.12: Predicted collapse loads (kN) of Arch05 and Arch06 for various beam plastic moments

numerical model developed in Chapter 3 can still be applied. The appropriateness of using this model is verified in Appendix C. As can be seen in figure 4.31, the angle of load spreading is wider in the case of bridges with reinforcement. This has a significantly beneficial effect on bridge capacity. Figure 4.30 indicates that the right-hand abutments are moving into the soil and causing a large shear band to the right of the arch. Figure 4.32 shows that the failure mechanism is not a 4-hinge mechanism. The deformation of the arch is very similar to that observed in the actual test, where a large movement of the abutment was seen. For Arch05, the predicted collapse loads were 624kN and 842kN respectively for the lower and upper bound approaches, which is a gross over-estimate (by approximately a factor of 2), compared to the actual bridge test collapse load of 375kN. In order to estimate influence of the angle of friction of the soil, a parametric study was performed. As in table 4.10, when $\phi = 40°$ the predicted collapse load is close to the experiment (335kN and 436kN for the lower bound and upper bound analyses respectively). Table 4.11 shows the predicted collapse loads of Arch06 for various clay strengths. It was found that when $c = 30$kPa, the predicted collapse loads are 271kN and 287kN, which is close to bridge test collapse load of 280kN. However, as can be seen from figures 4.35 to 4.38, for both Arch05 and Arch06, the slopes of the soil movement vectors indicated by PIV on the passive side of the arch are much less than predicted by FELA.

In order to estimate the influence of the near road-surface steel beam on bridge carrying capacity, various plastic moment values (Mp) for the beam were examined, Table 4.12. From the predicted collapse loads it can be seen that increasing the
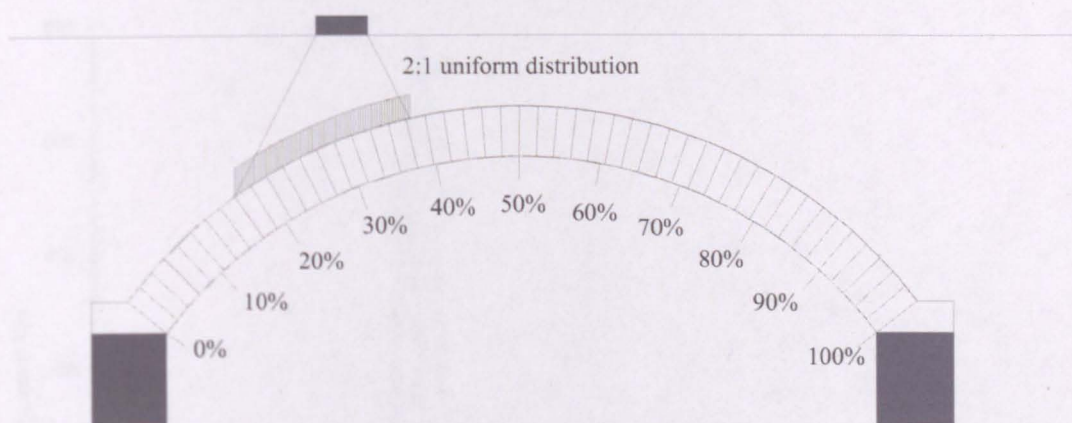
FIGURE 4.26: A 2:1 uniform distribution by BD21/01

plastic moment of the beam will result in a greater bridge capacity. For Arch05, doubling the beam plastic moment will increase the capacity by approx. 15%, whilst for Arch06, the corresponding increase is approx. 12%.

Load spreading in masonry arch bridges

The ability of the backfill to spread the load has long been considered to be important (see e.g Callaway (2007)). Figure 4.26 shows a 2:1 uniform stress distribution (2 vertical, 1 horizontal) given by BD21 (2001). In this case the load spreads from 17% to 38% of the extrados. However, it is evident from figure 4.27 that in reality the load is likely to be significantly more focused than predicted by the simple 2:1 model. In this figure, the stress is concentrated from 30% to 40% of the extrados. Figure 4.27 also indicates that the load spreading is quite insensitive to ϕ. The normal stress acting on the extrados of Arch01 and Arch05 are plotted in figure 4.28. This figure demonstrates that the load is spread over a much wider range when the near-road surface beams are present (from 30% to 45% of the extrados). The load is also less concentrated, leading to an increase in bridge strength.
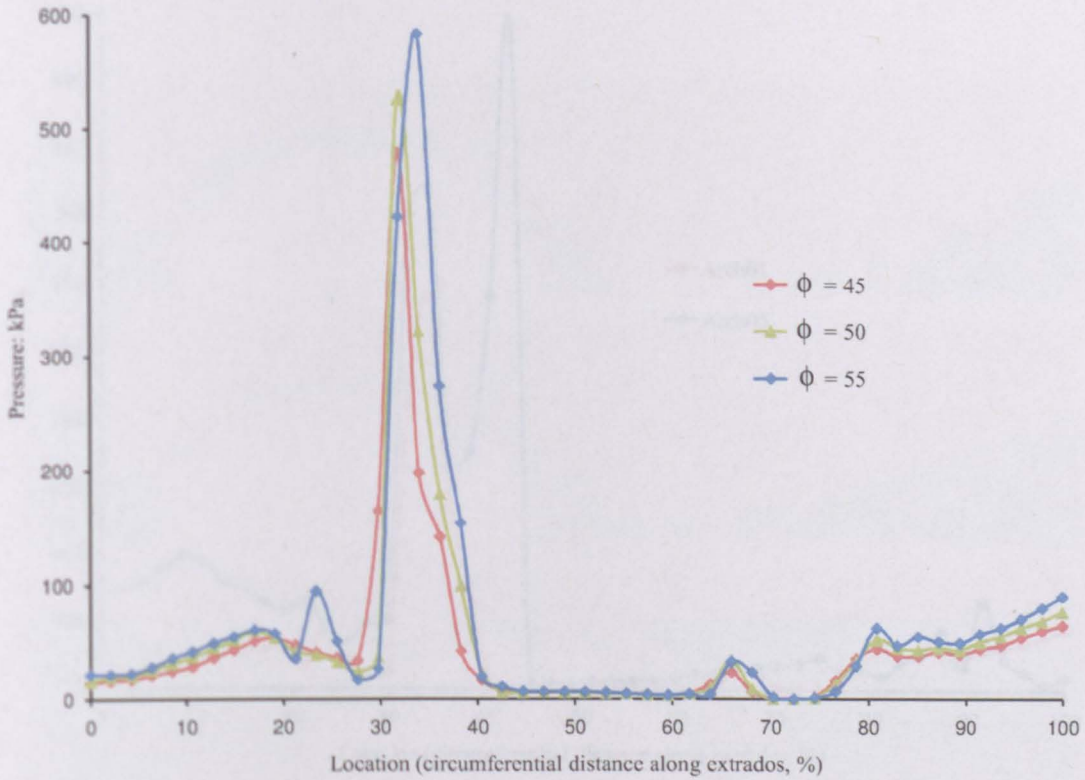
FIGURE 4.27: Arch01:normal stress on the extrados for various of ϕ

4.5   Conclusions

In this chapter, the FELA model developed in Chapter 3 has been used to analyze
the full-scale bridge tests recently conducted at Salford University. Through a
number of analyses, the following conclusions can be drawn:

- Some difficulties were initially experienced when attempting to apply the
  model to a laboratory test bridge. Although high quality soil strength data
  was generally available, since soil strength requires significant strains before
  it is fully mobilized, there were question-marks over what values should be
  used in the model, given also that large arch deformations reduce its load
  carrying capacity. Furthermore the soil-arch interface friction has not yet
  been measured, introducing further uncertainty.
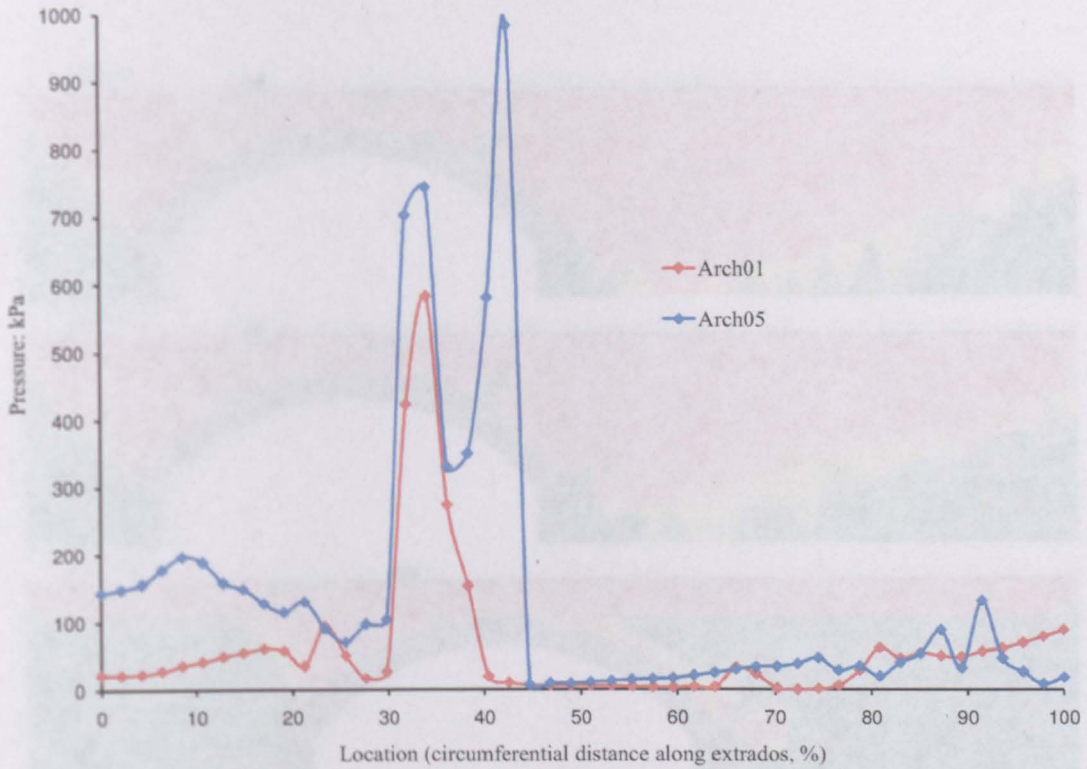
FIGURE 4.28: Arch01 and Arch05:normal stress on the extrados

- Numerical results indicate that the nature of the surface load (smooth or rough) has negligible effect on the arch load capacity, whilst in contrast the soil-arch interface properties have a significant influence on the predicted ultimate load carrying capacity.

- Though further investigations are warranted it is now clear that neglecting soil strength mobilization and/or gross displacement strength reduction may lead to significant over-prediction of the ultimate collapse load.

- The above numerical model in some cases, predicts local soil failure rather than the desired failure of the arch, depending on the nature of backfilled material.

- For the bridges considered, the model indicated that the applied load is more focused than the 2:1 uniform stress distribution given in BD21 (2001).
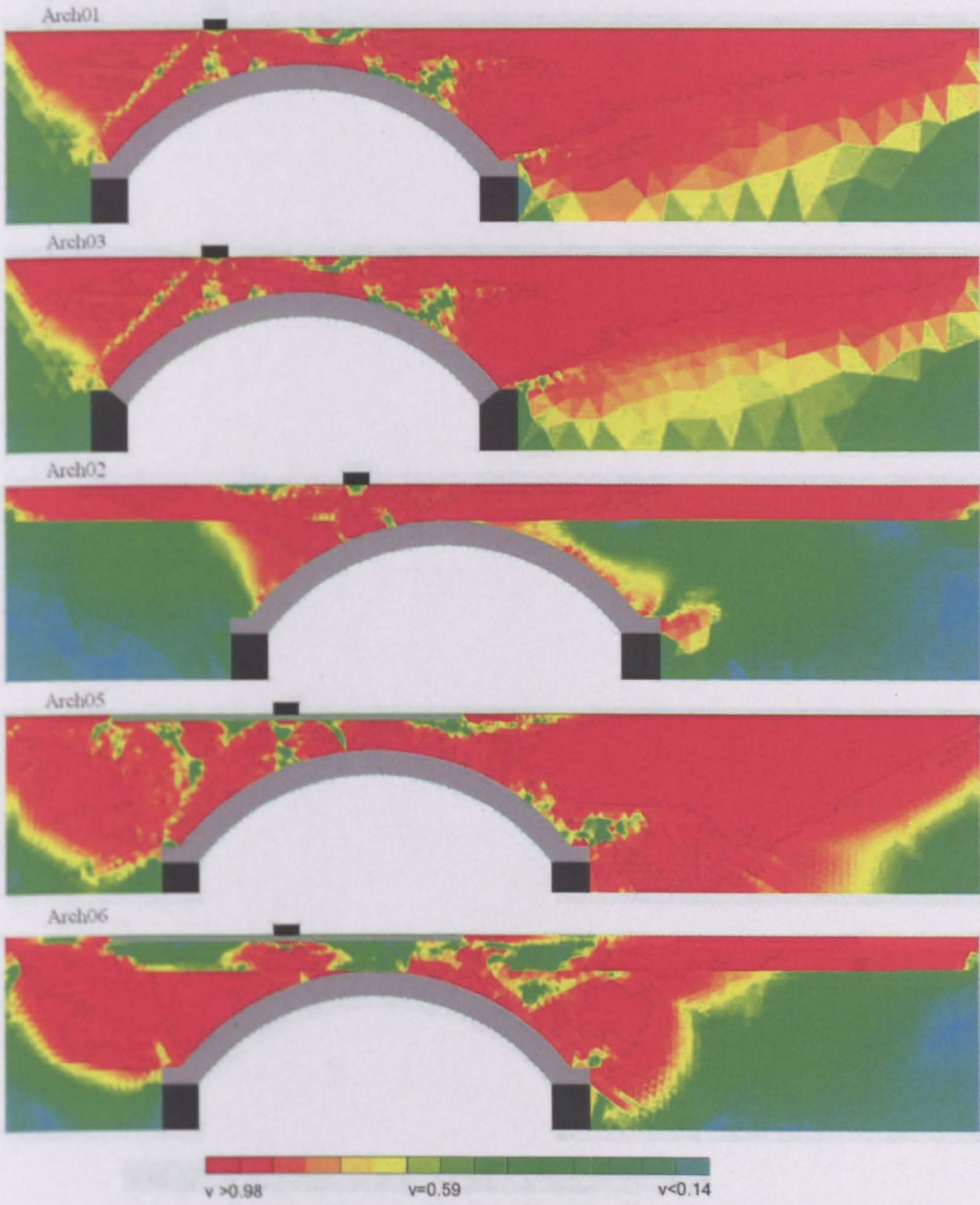
FIGURE 4.29: Variation in maximum shear stress relative to the yield stress

FIGURE 4.30: Variation in shear strain rate
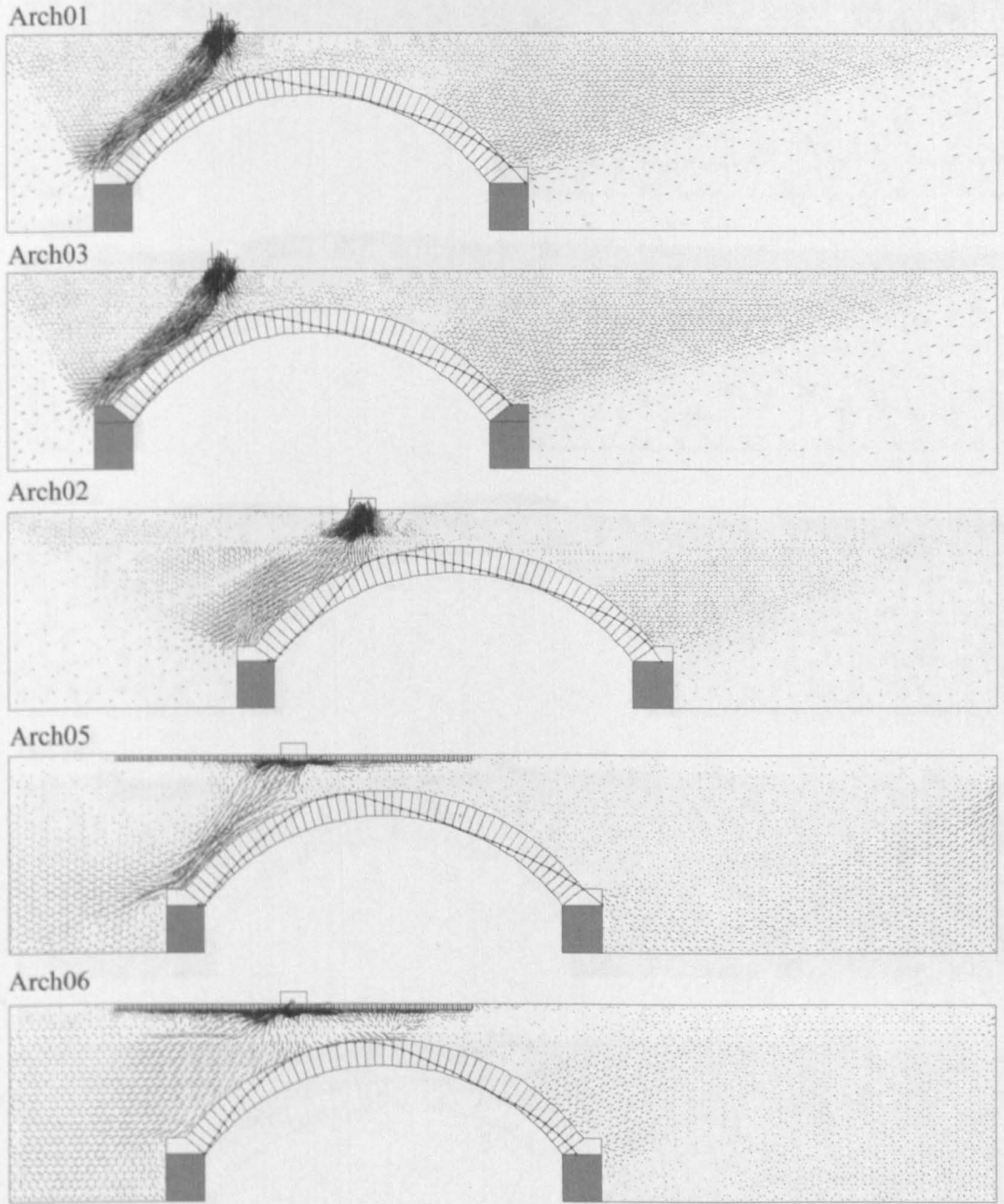
FIGURE 4.31: Maximum (compressive) principal stress vectors

Arch01

Arch03

Arch02
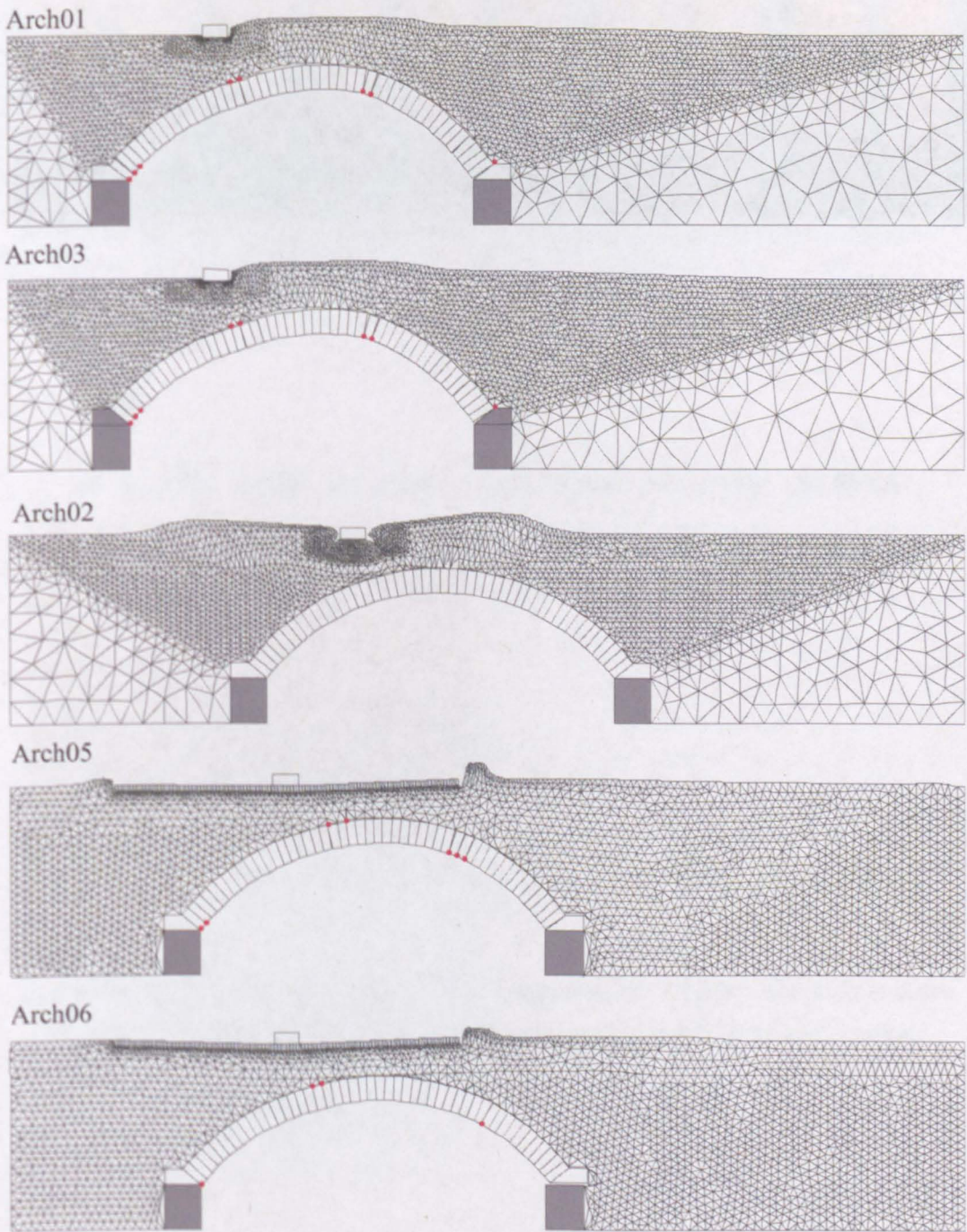
Arch05

Arch06

FIGURE 4.32: Deformed shape of soil and arch
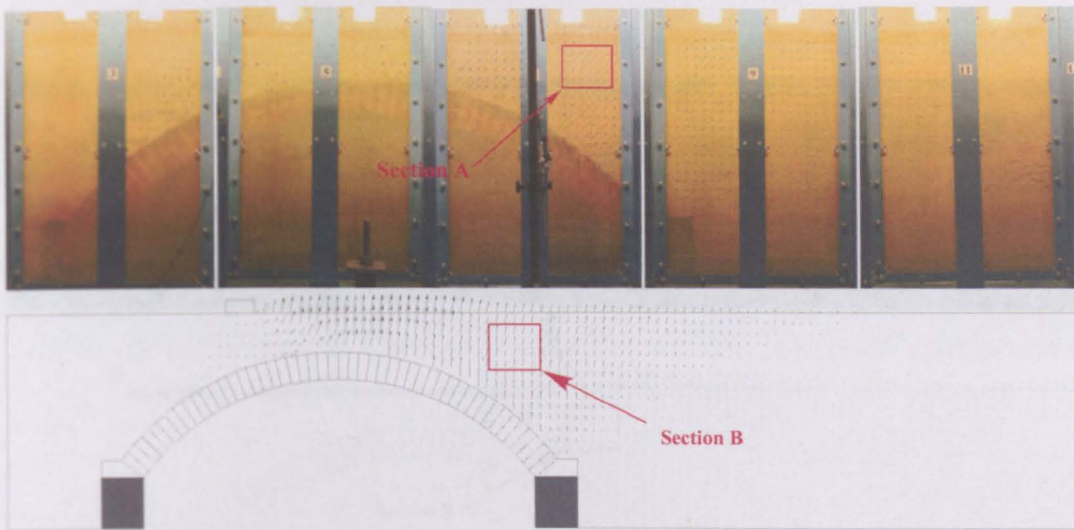
FIGURE 4.33: Arch01: Comparison of velocity field given by PIV and FELA
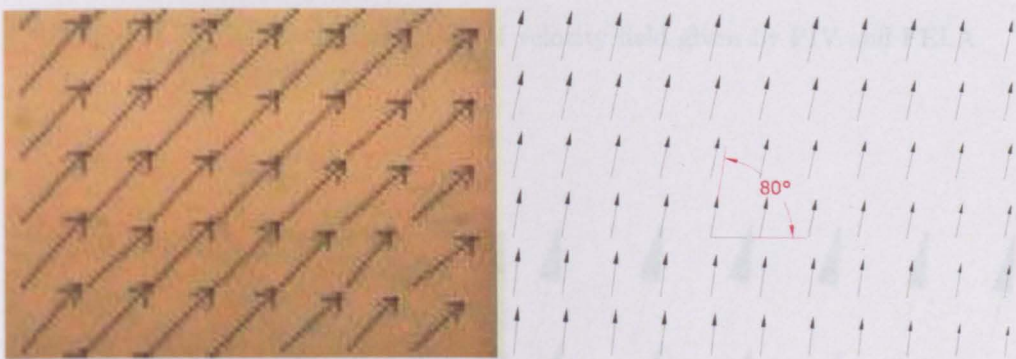
FIGURE 4.34: Arch01: Velocity field given by PIV (Section A) and FELA (Section B)

- For bridges with near-road surface reinforcement (beams), the load is more widely spread than is the case for similar bridges without reinforcement.
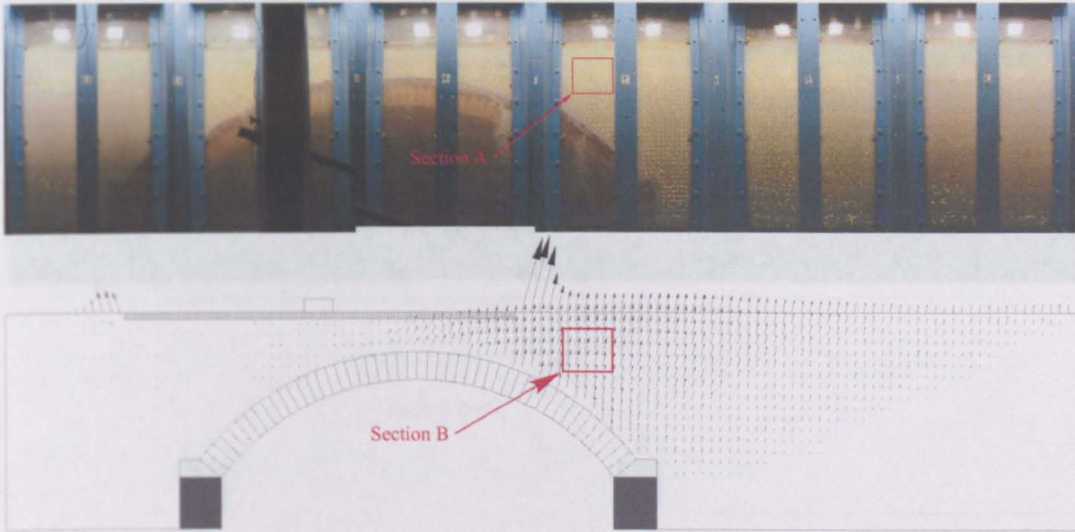
FIGURE 4.35: Arch05: Comparison of velocity field given by PIV and FELA
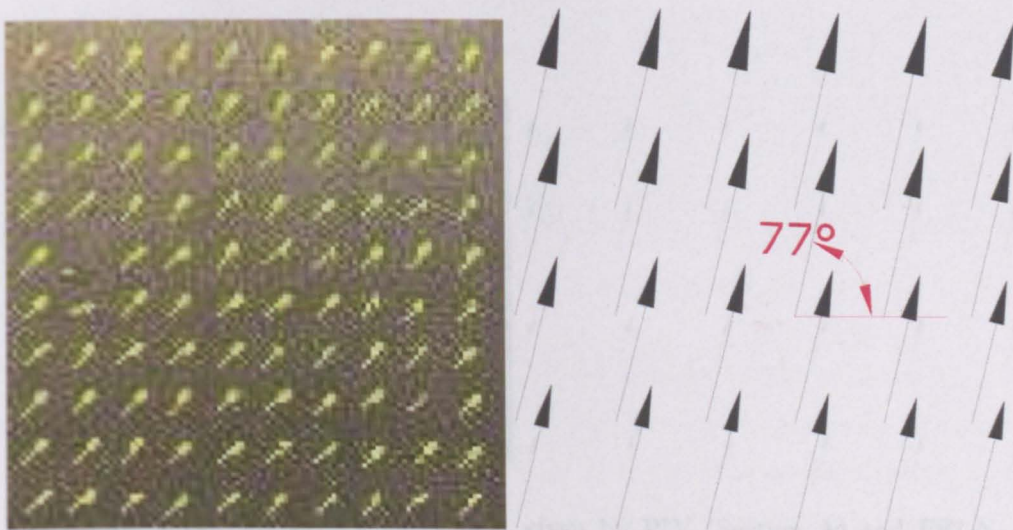
FIGURE 4.36: Arch05: Velocity field given by PIV (Section A) and FELA
(Section B)
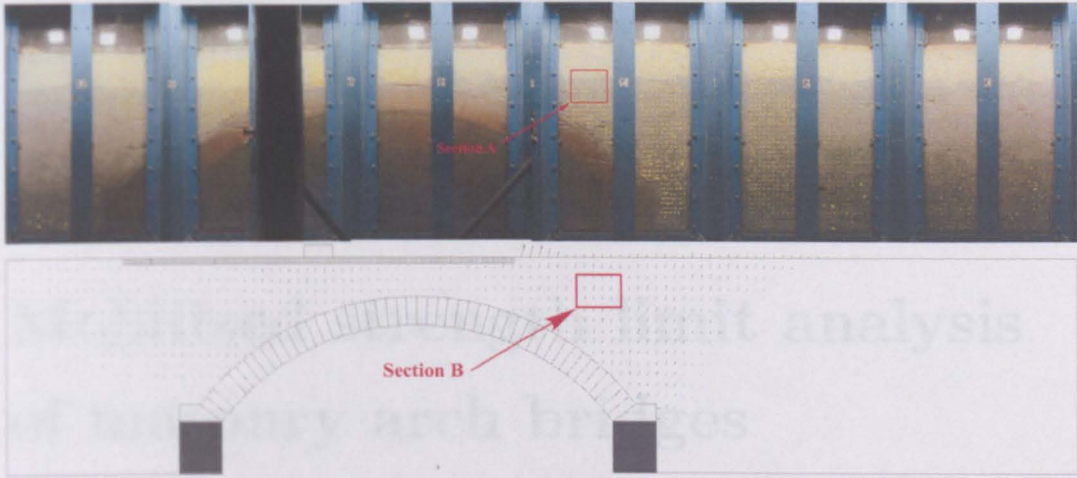
FIGURE 4.37: Arch06: Comparison of velocity field given by PIV and FELA
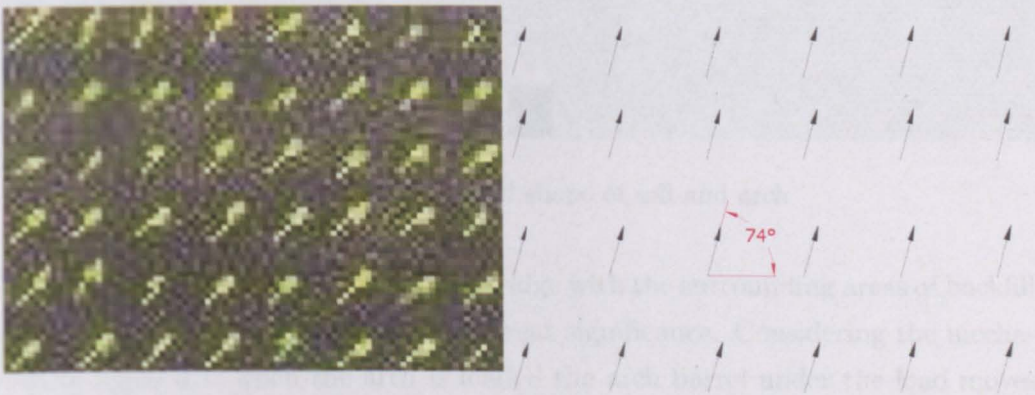
FIGURE 4.38: Arch06: Velocity field given by PIV (Section A) and FELA
(Section B)

Chapter 5

Mobilized strength limit analysis of masonry arch bridges

5.1 Introduction
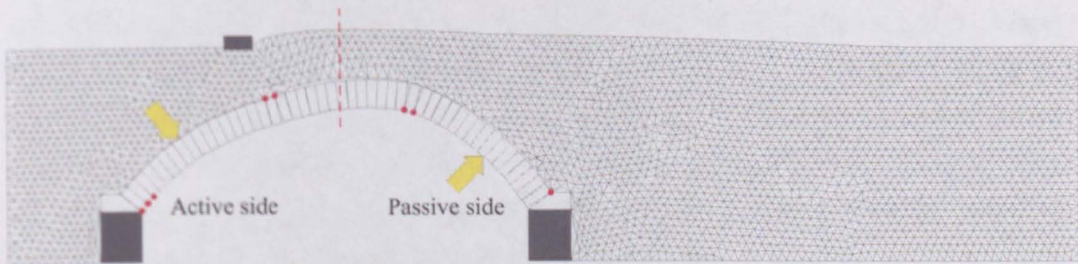
FIGURE 5.1: Deformed shape of soil and arch

The interaction of the barrel of an arch bridge with the surrounding areas of backfill material has been found to often be of great significance. Considering the mechanism in figure 5.1, when the arch is loaded the arch barrel under the load moves away from the backfill (*active* condition), whilst the arch barrel on the right moves into the fill (*passive* condition). When a section of the arch barrel moves into the fill, substantial passive horizontal pressures can be mobilized, thus restraining the barrel and strengthening the bridge. These restraining pressures will be especially

important in the case of deep arches. The beneficial effects of horizontal backfill pressures on the strength of masonry arch bridges was appreciated by Crisfield & Packham (1987), who included this effect in the analysis of an arch bridge. Many workers have included horizontal backfill pressures in their analysis methods, and, almost without exception, have used the equations of classical passive pressure theory. Indeed, despite the dissimilarities between the shape of an arch barrel and a vertical wall, Rankine's passive pressure developed for a vertical wall have been used when analysing masonry arch bridges (Crisfield & Packham (1987), Choo & Gong (1990)). The result is that overestimates of the passive resistance attainable will be made unless the passive pressure coefficients are empirically scaled down. Recently, work by Burroughs et al. (2002) confirms that full passive pressure limits are not reached and they suggest the applied pressures are scaled down towards the hinge point. Including backfill pressures in arch bridge analysis is however problematic for another reason. This is because full passive pressures tend to be mobilized only after large movements of the retaining wall have taken place (see e.g. Chen (1975)). Conversely an arch barrel is most able to carry applied loads in its undeformed state - large movements of the barrel significantly reduce the ability of the arch to carry load. In an elastic arch bridge analysis, (e.g. Choo & Gong (1990), Crisfield & Packham (1987)) the failure of a bridge is likely to occur well before full passive pressures are mobilized and thus the assumed initial stiffness of the backfill material will be important. However, in the case of plastic analysis, the full passive resistance is unlikely to be mobilized at the point of bridge failure and this makes it is difficult to predict the amount of restraint which will be offered by the backfill.

As with retaining wall analysis, the concept of mobilized strength appears to be important when performing a soil-arch analysis. The strength of a backfilled arch derives partly from the masonry structure itself and partly from the backfill. However the full strength of each component is not typically mobilized simultaneously. As the arch itself initially starts to deform, its full strength will be mobilized, but this will decrease as deformation modifies its geometry. Simultaneously, the deforming arch gives rise to shear strains within the soil; however a moderate amount of arch deformation is required before these shear strains mobilize full soil strength.

Somewhere between these two stages, the combined soil-arch system will generate its peak load capacity. Implicit in the model presented in the previous chapter is the assumption that soil and arch will mobilize their peak strength simultaneously; this does not always hold true as indicated by the over-estimated predicted bridge load carrying capacities obtained. In the first section of this chapter, a mobilization factor is applied to the passive side of the arch to study its effect on bridge capacity, thereby informing the needs of an improved model.

5.2   Simple mobilized strength analysis

5.2.1   The influence of mobilized soil strength

In this section, Arch01 and Arch02 are revisited, with a mobilization factor applied to the passive side of the arch. It is assumed that the soil on the active side is fully mobilized with $c = 3.3, \phi = 54.5$ and that the soil on the passive side has strength c_{mob}, ϕ_{mob}. The soil-arch interface friction is assumed to be $\phi/3$. Table 5.1 shows the variation of collapse load with mobilization factor for Arch01. The results suggest that with a mobilization factor of approximately 0.33, the predicted collapse load by the lower and upper bound analysis would be close to the actual test collapse load of 128kN. Table 5.2 shows the variation of collapse load with mobilization factor for Arch02 in which * denotes a local footing failure. The full mobilized shear strength was taken as $c = 80$kPa and the soil-arch interface as $\frac{1}{3}c$. It is interesting to note that the arch fails when there is a low mobilization factor on the passive side, whereas for a higher mobilisation factor, a local footing failure is predicted. In figure 5.2, the soil is yielding under the load and on the passive side of the arch when the mobilization factor is 0.01, indicating arch failure. The arch barrel on the passive side pushes the soil upwards causing yield of the soil. From this simple analysis, it can be concluded that it is important to use soil mobilized strength when using finite element limit analysis; ignoring soil mobilized strength could lead to an over prediction and may even predict an incorrect failure mechanism.

Mobilization factor	Lower-bound	Upper-bound
0.01	79.4	105.4
0.1	84	115.3
0.25	95.6	127.1
0.33	100.2	135.2
0.45	106	142.3
0.5	111.3	151.53
0.67	127	172.4
0.8	142.4	195.1
1.0	175	228.5

TABLE 5.1: Arch01: Collapse load (kN) with various mobilization factors

Mobilization factor	Lowerbound	Upperbound
0.01	69.6	106
0.1	90.2	118.2
0.2	108.1	124.5
0.5	122.7*	141.5*
1.0	148*	200*

TABLE 5.2: Arch02: Collapse load (kN) with various mobilization factors

v >0.98   v=0.59   v<0.14
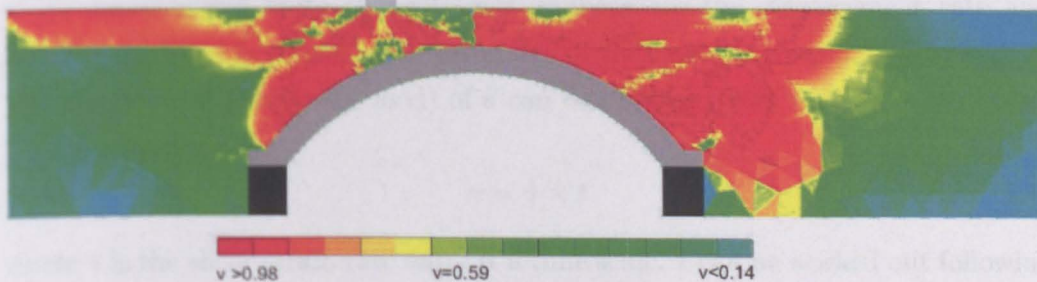
FIGURE 5.2: Arch02: variation in maximum shear stress relative to the yield
stress with mob=0.01

5.2.2 Simple model for mobilized strength analysis
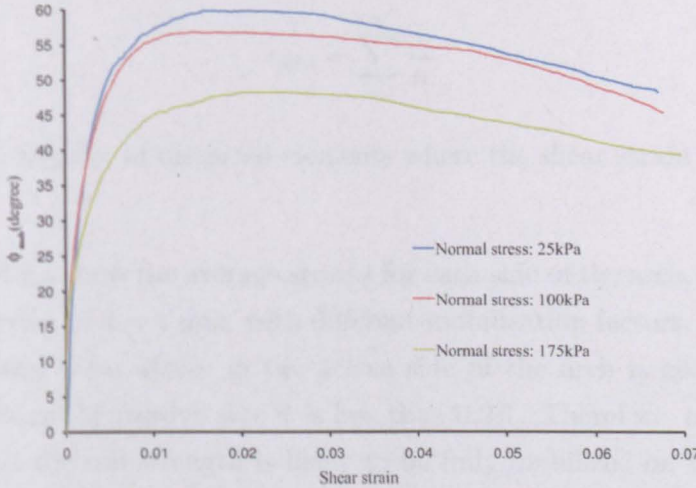
FIGURE 5.3: Limestone mobilised soil strength against shear strain

From the preceding section, it can be seen that applying a mobilization factor could lead to a good prediction on bridge capacity. However, the obvious question that arises is: what mobilization factor should be used? In this section, a simple model is developed with the aim of answering this question.

Considering Arch01: the arch is divided into an active side and a passive side and the mobilization factor is applied for each side of the arch separately. Subsequently, the average shear strain is calculated for each side of the arch. Since the products of an upper-bound finite element limit analysis are the displacement rate and strain rate, it can be argued that estimates of the strain corresponding to a given arch displcement (under the load) of d can be obtained with a suitable multiplier t, as in equation 5.1.

$$\gamma = \dot{\gamma} \times t \tag{5.1}$$

where $\dot{\gamma}$ is the shear strain rate and t is a time scale. t can be worked out following the equation:

$$t = \frac{d}{\dot{d}} \tag{5.2}$$

in which $\dot{d}$ is the displacement rate and d is the assumed radial displacement of the arch barrel. The average shear strain can be worked out following equation:

$$\gamma_{ave} = \sum_{i=1}^{n} \frac{\gamma_i}{n} \qquad (5.3)$$

where n is the number of distorted elements where the shear strain rate is greater than zero.

Tables 5.3 and 5.4 show the average strains for each side of the arch, corresponding to the assumption of $d = 1$ mm, with different mobilization factors. It can be seen that the average shear strain in the active side of the arch is generally greater than 2%, while in the passive side it is less than 0.2%. Therefore, from figure 5.3, it appears that the soil strength is likely to be fully mobilized on the active side. On the passive side with 0.2% shear strain, ϕ_{mob} is approximately 25°; this leads to the mobilization factor of 0.45. With this factor, from table 5.1, the predicted collapse load will be 106kN and 142kN for the lower bound and upper bound approach respectively.

Active mobilization factor	Active average shear strain	Passive average shear strain	Collapse load (kN)
1	0.026	0.0011	241
0.95	0.029	0.0009	220
0.9	0.026	0.001	201
0.85	0.033	0.001	182
0.8	0.087	0.0016	155
0.75	Local failure	-	-

TABLE 5.3: Average shear strain for various active mobilisation factor

From the above analysis, the simple model for mobilized strength analysis (called MSD) is described as below:

1. Solve the problem with the peak soil strength on both sides of the arch.

2. Work out the average shear strain rate and assuming the radial displacement of the arch.

Passive mobilization factor	Active average shear strain	Passive average shear strain	Collapse load (kN)
1	0.03	0.0013	241
0.8	0.021	0.0011	195
0.5	0.028	0.0011	152
0.25	0.032	0.0014	127
0.1	0.033	0.0019	115

TABLE 5.4: Average shear strain for various passive mobilisation factor
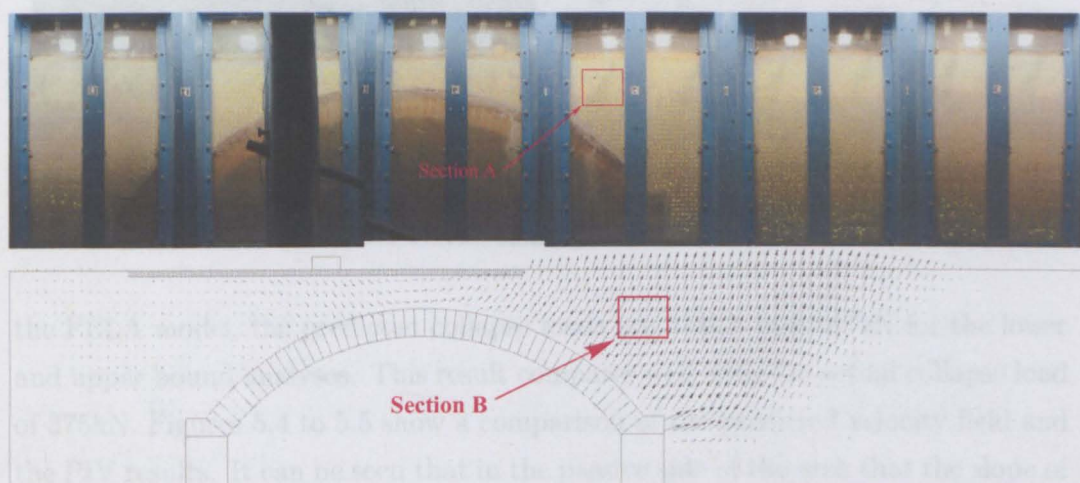
FIGURE 5.4: Arch05: Comparison of velocity field given by PIV and MSD

3. From the assumed radial displacement, work out the average shear strain for the active and passive sides of the arch.

4. From this average shear strain, deduce the mobilized soil strength from the actual shear strain-strength curve.

5. Use the mobilized soil strength and re-analyse.

This simple model is used to re-analyse Arch05 (recall that in Chapter 4 the predicted collapse load was a significant over-estimate of the actual bridge capacity). The average shear strain for the active side is 0.51%, whereas for the passive side it is 0.11%. From figure 5.3, the mobilized strength will be $\phi = 48^o$ and $\phi = 25^o$ for the active and passive side respectively. Applying these mobilised soil strengths to
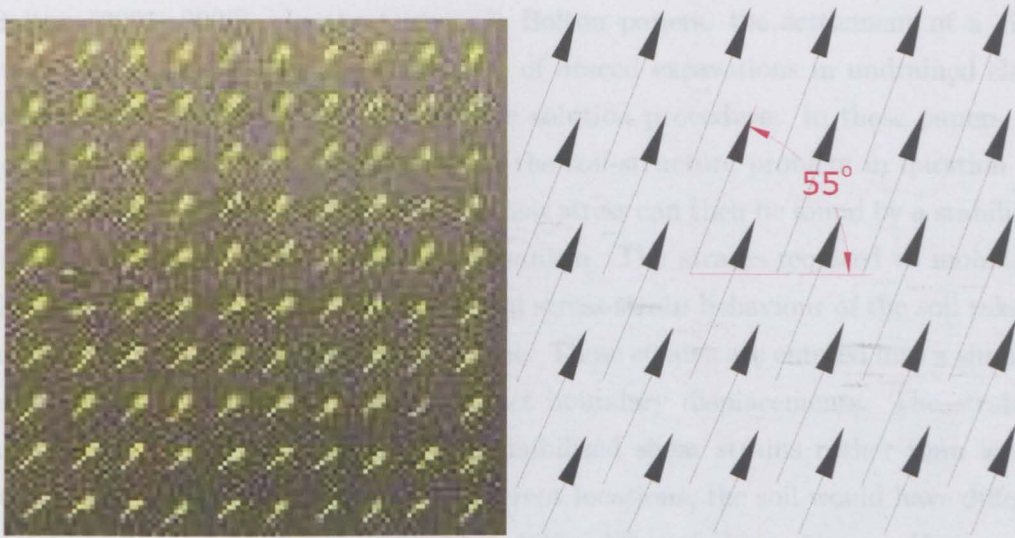
FIGURE 5.5: Arch05: Velocity field given by PIV(Section A) and MSLA (Section B)

the FELA model, the predicted collapse loads are 318kN and 387kN for the lower and upper bound analyses. This result compares well with the actual collapse load of 375kN. Figures 5.4 to 5.5 show a comparison of the predicted velocity field and the PIV results. It can be seen that in the passive side of the arch that the slope of the velocity vector given by the MSLA is greater than the PIV by approximately 10°.

However, it is uncertain what value the arch displacement would be. This poses a limit on the above procedure. Furthermore, the simple model can not be used when the local soil failure is likely to occur (as was the case with Arch02). Therefore, a more powerful model is required.

5.3 Mobilized strength limit analysis: MSLA

In this section, an alternative numerical kinematic plastic model is presented. The idea of mobilized strength design (MSD) was introduced almost two decades ago by Bolton et al. (1989, 1990); Bolton & Sun (1991) and recently by Osman &

Bolton (2005, 2006). In the Osman & Bolton papers, the settlement of a circular footing and the ground movement of braced excavations in undrained clay were predicted using a kinematic plastic solution procedure. In these papers, a compatible plastic deformation field for the soil-structure problem in question is determined in advance. The mobilized shear stress can then be found by a stability calculation based on the predicted mechanism. The strains required to mobilize these stresses are deduced from the actual stress-strain behaviour of the soil taken from a selected location in the plastic zone. These strains are entered into a simple plastic deformation mechanism to predict boundary displacements. The strains used in the MSD method are average mobilized shear strains rather than local strains at every location. In fact, at different locations, the soil would have different stress-strain responses and would mobilize different shear stresses. Hence use of a pre-described plastic mechanism in MSD is only suitable for simple problems. The new numerical model presented by the author could potentially offer a versatile alternative compared to the Bolton and Osman model in that it can handle problems with complicated geometries where the plastic deformation is hard to foresee. This approach, termed Mobilized Strength Limit Analysis (MSLA), is described as follows:

1. Initialize the problem with an assumed low mobilized soil strength in each element.

2. Determine the collapse load for the currently defined mobilized soil strengths.

3. Determine the shear strain rate for each element.

4. Update the accumulated shear strain for each element over a specified time step t.

5. Update the shear strength for each element, according to the shear strain.

6. Repeat from 2 until termination criteria are met.

In the above procedure, the time step t can be determined using the following equation:

$$t = \frac{\epsilon_{incr}}{\epsilon_{max}} \tag{5.4}$$

and the accumulated shear strain ϵ_a for each element is determined following the equation:

$$\epsilon_a = \epsilon_{pre} + t\epsilon_{rate} \tag{5.5}$$

in which ϵ_{incr} is the required maximum strain increment for each iteration and is specified in advance, ϵ_{max} is the maximum shear strain rate of the deformed elements in a particular iteration. ϵ_{pre} is the accumulated strain in the previous iteration. ϵ_{rate} is the shear strain rate of an element. The mobilized strength can be determined from actual soil strength-strain data. The termination criteria can be based either on the load or the displacement. The above procedure takes into account strain-hardening behavior and non-linear stress-strain characteristics. One of the simplifying assumptions in the model is that the problem geometry does not change during the strain-increment process. The ideal model would model changes in geometry after each iteration. However, this would involve remeshing and reformulation of the LP problem after every iteration. If the remeshing process is adopted, this also leads to another difficulty in that the accumulated shear strain for each element is hard to determine. One of the features of the above model is that it can be used to estimate the actual load-displacement curve of a given soil-structure problem.

5.3.1 Foundation settlement on a clay

The above numerical procedure is compared with a non-linear finite element prediction of immediate settlement for a foundation resting on clay. Bolton & Sun (1991) carried out a series of non-linear finite element analyses for a clay that has a stress-strain relationship of the form:

$$\frac{c_{mob}}{c_u} = (\frac{\gamma}{\gamma_u})^b \tag{5.6}$$

and applied to an isotropic soil body with no history of shear strain. The foundation settlement can be evaluated following the equations:

$$\frac{\delta_{ave}}{B} = I_{ave}\gamma_u(\frac{q}{5.14c_u})^{1/b} \tag{5.7}$$

$$\frac{\delta_{max}}{B} = I_{max}\gamma_u\left(\frac{q}{5.14c_u}\right)^{1/b} \tag{5.8}$$

These equations are the result of Bolton's work and were worked out following the combination of different plastic mechanisms. In the above equations, I_{ave} and I_{max} are determined by non-linear finite element analysis as a function of b see (figure 5.7). q is the footing pressure and c_u, γ_u, b are the governing factor for non-linear stress-strain curve. δ_{ave} is the average settlement of under the width of a rigid footing and δ_{max} is the maximum settlement under the center of flexible footing. Figure 5.8 obtained from Bolton & Sun shows the actual stress-strain data with the a approximation stress - strain model by using equation 5.6.

Similar to an example provided in Bolton & Sun's paper, consider a 4m strip footing which rests on the surface of a 15m thick London Clay layer overlying very stiff Woolwich Beds, which are assumed to be rigid. A good quality sample of the London Clay tested in an undrained triaxial test with internal strain measurement showed that the stress-strain curve could be represented by equation 5.6, where $c_u = 70\text{kN/m}^2$, $\gamma_u = 2\%$ and $b = 0.5$. The footing pressure was applied in small steps up to maximum value of 250kN/m^2. A relatively coarse mesh composed of 1752 elements was used for the MSLA analysis. Parameters used for the MSLA analysis were initial $c_{mob} = 1\text{kPa}$ and shear increment $\epsilon_{incr} = 0.25\%$, or 12.5% of γ_u. Figure 5.6 shows that the results from the MSLA. For the same applied pressure, the MSLA model predicts an approx. 20% larger maximum settlement than Bolton's model. For example, if the applied pressure is 150kN/m^2, the maximum settlement given by Bolton's model will be 16mm, whereas the MSLA model predicts 20mm of settlement.

Table 5.5 shows results for various shear increments, ϵ_{incr}. In the table, the loads were obtained at 60mm settlement. From table 5.5 and figure 5.6,it can be seen that the MSLA solution is very insensitive to ϵ_{incr} when ϵ_{incr} is small. The disadvantage of the MSLA method is that it is a time consuming process. As illustrated in table 5.5, for a simple strip footing problem, with relatively coarse mesh, the time taken to solve is approximately one hour on a powerful Dell desktop computer equipped with Intel Core 2 Quad-core PC running at 2.4GHz and with 2GB
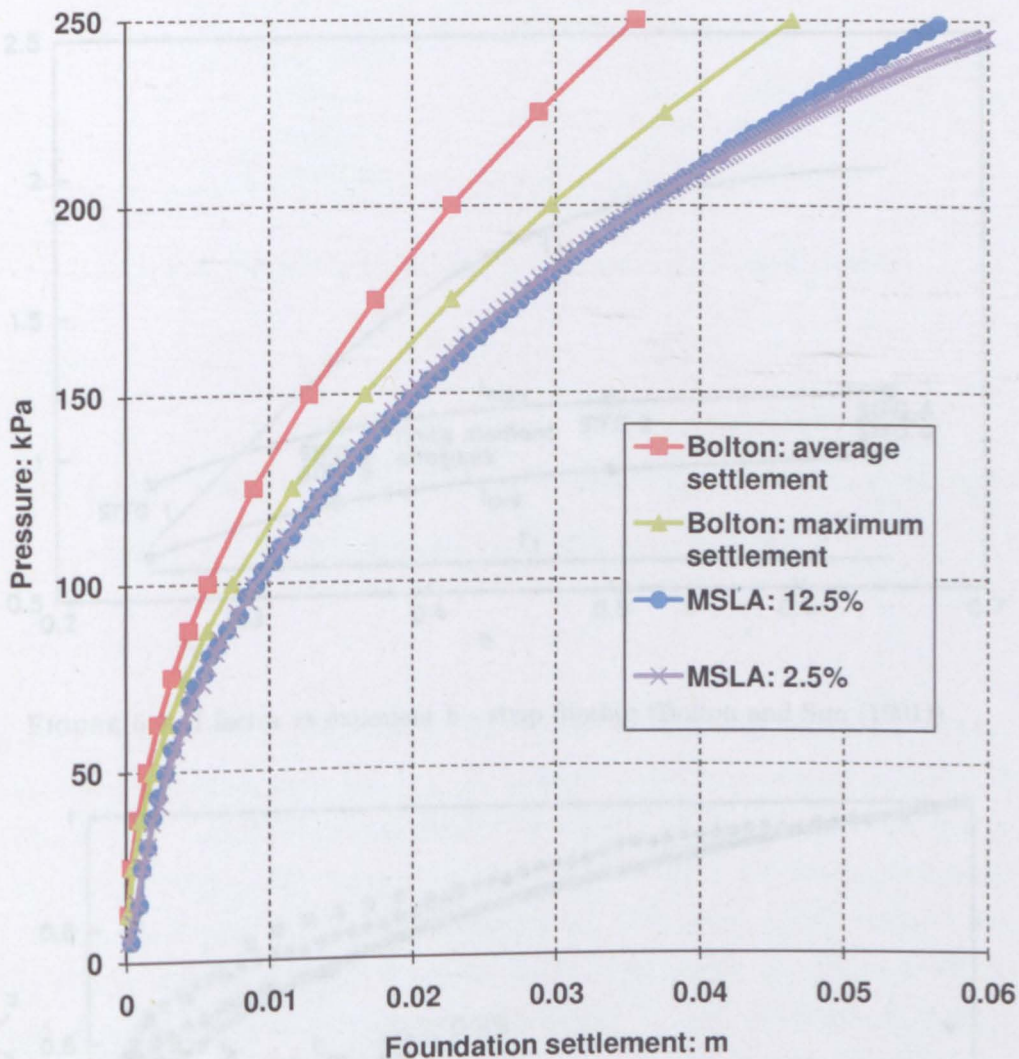
FIGURE 5.6: Load vs foundation settlement

ϵ_{incr} %γ_u	Load kN	Number of iteration	Computational time (s)
12.5	249.2	82	3321
7.5	248.1	105	4252
5	247.8	137	5370
2.5	244.7	169	6884

TABLE 5.5: Parametric study on the influence of shear strain increment for MSLA method
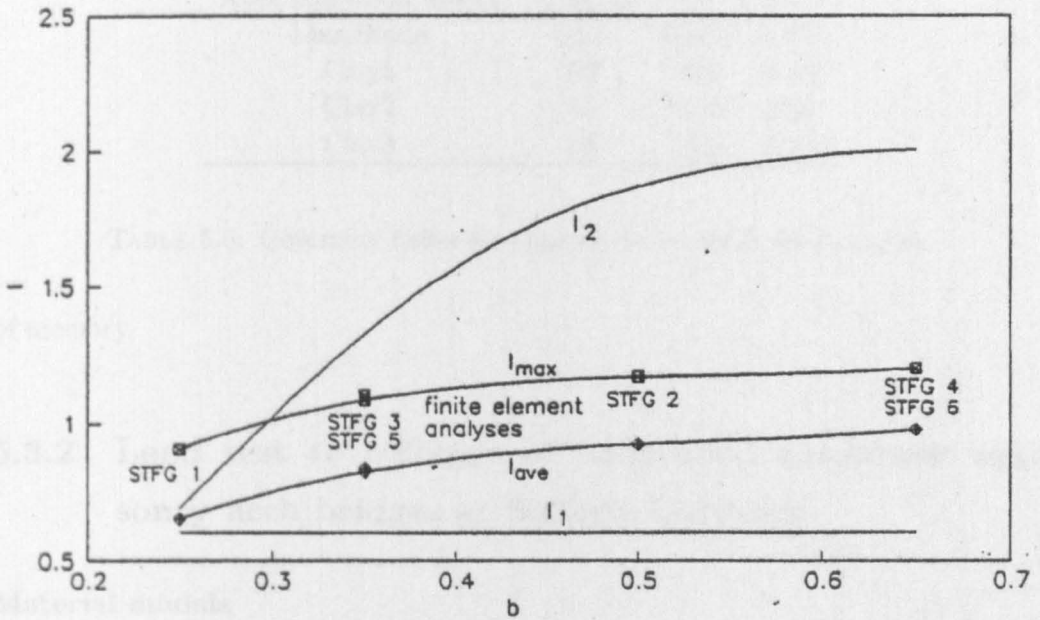
FIGURE 5.7: I factor vs exponent b - strip footing (Bolton and Sun (1991))
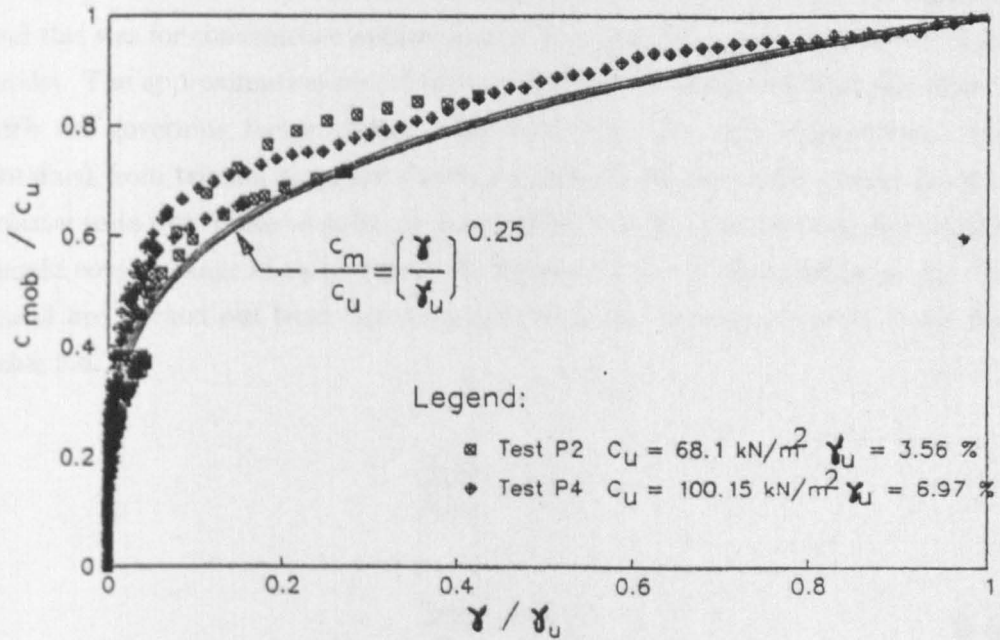
FIGURE 5.8: Typical response of kaolin following load reversal (Bolton and Sun (1991))

Approximation model	c_u/ϕ_{peak}	γ_u	b
LimeStone	54.5	0.015	0.25
Clay1	52	0.05	0.38
Clay2	35	0.05	0.38
Clay3	68	0.05	0.45

TABLE 5.6: Governing factor for approximation stress-strain curves

of memory.

5.3.2 Load test to collapse of back-filled brickwork masonry arch bridges at Salford University

Material models

The MSLA model was used to analyse the Salford bridge tests. The actual stress-strain curves of the limestone obtained from shear box tests are shown in figure 5.9 and this was for convenience approximated by a non-linear elastic-perfectly plastic model. The approximation model for the limestone is evaluated from equation 5.9 with the governing factors taken from table 5.6. The clay stress-strain curves obtained from triaxial tests are shown on figure 5.10. Since the results from the triaxial tests were quite variable, it was decided that the numerical approximations should cover a range of these curves. In figure 5.10 the approximation models 1, 2, and 3 are worked out from equation 5.10 with the governing factors taken from table 5.6.

$$\frac{\phi_{mob}}{\phi_{peak}} = (\frac{\gamma}{\gamma_u})^b \tag{5.9}$$

$$\frac{c_{mob}}{c_u} = (\frac{\gamma}{\gamma_u})^b \tag{5.10}$$
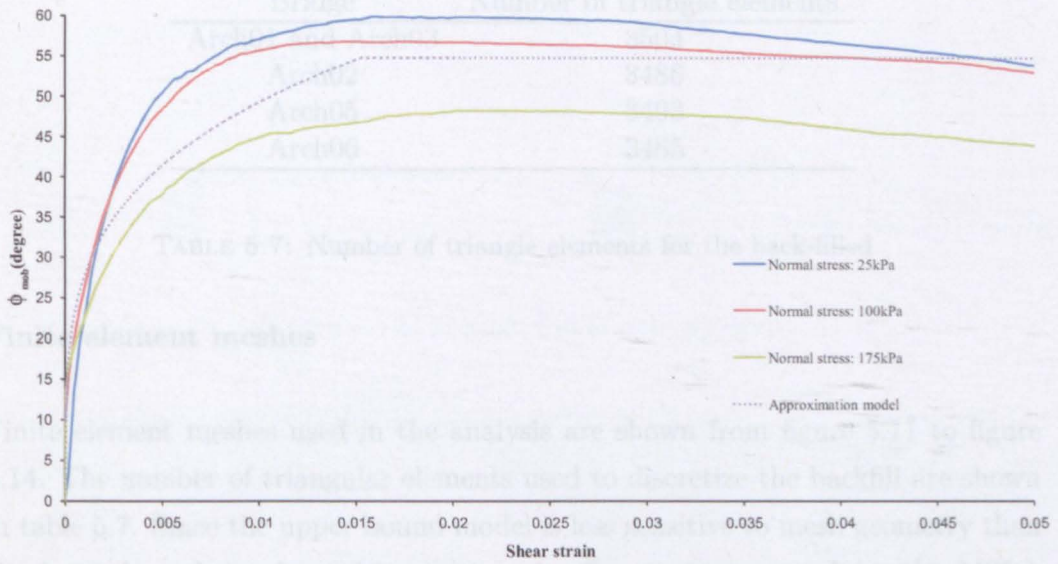
FIGURE 5.9: LimeStone mobilised soil strength against shear strain and approximation model
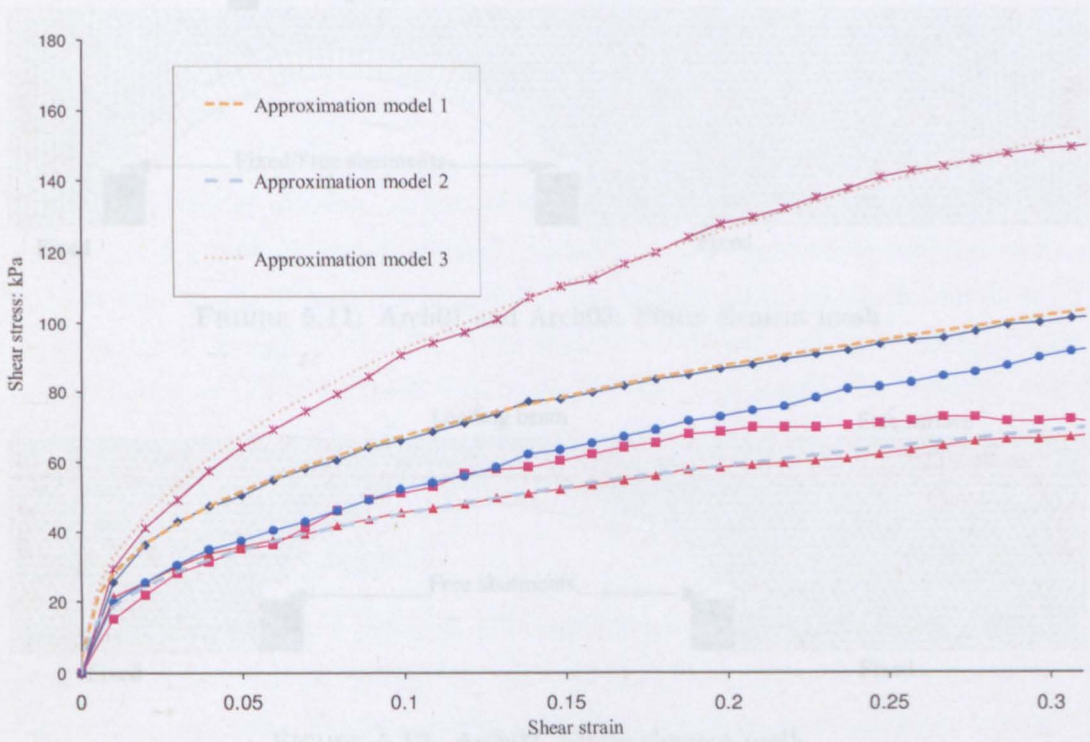
FIGURE 5.10: Clay stress strain curves and approximation models

Bridge	Number of triangle elements
Arch01 and Arch03	3504
Arch02	3486
Arch05	3493
Arch06	3485

TABLE 5.7: Number of triangle elements for the back-filled

Finite element meshes

Finite element meshes used in the analysis are shown from figure 5.11 to figure 5.14. The number of triangular elements used to discretize the backfill are shown in table 5.7. Since the upper bound model is less sensitive to mesh geometry than the lower bound, meshes without manual refinement were used for the MSLA analysis.
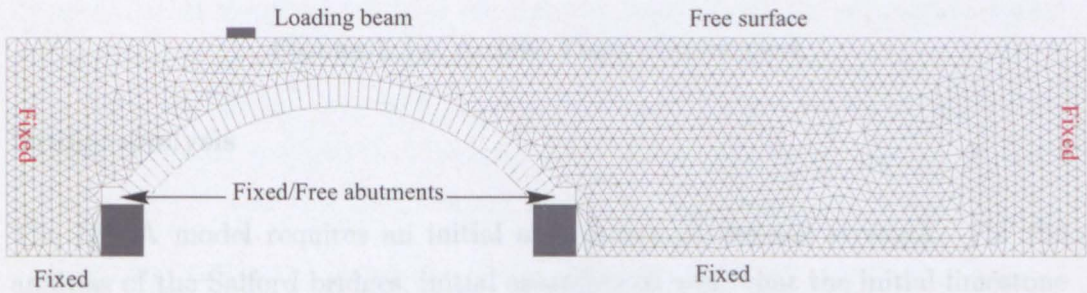
FIGURE 5.11: Arch01 and Arch03: Finite element mesh
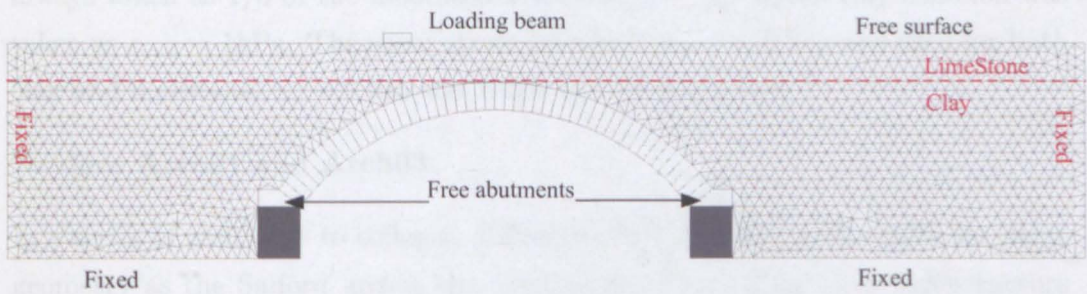
FIGURE 5.12: Arch02: Finite element mesh
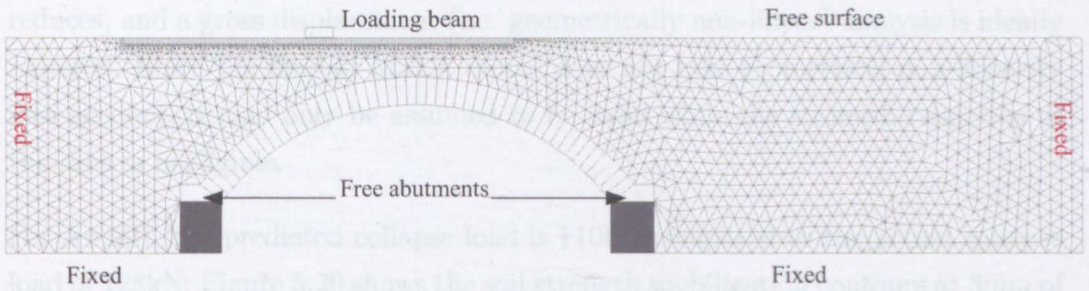
FIGURE 5.13: Arch05: Finite element mesh
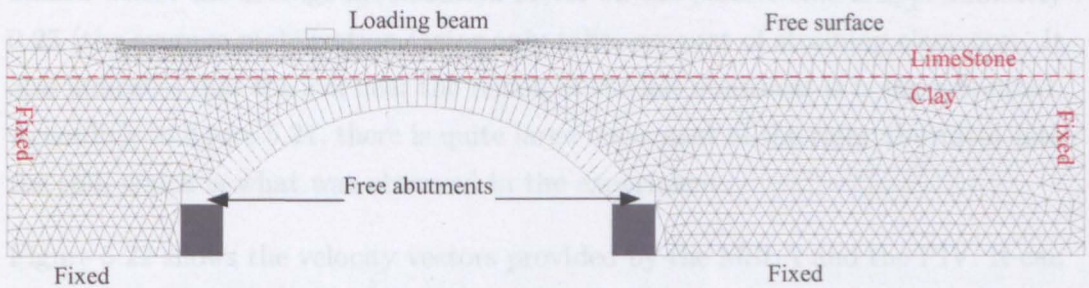
FIGURE 5.14: Arch06: Finite element mesh

Bridge analysis

The MSLA model requires an initial assumption of the soil strength. For the analysis of the Salford bridges, initial assumptions were that the initial limestone friction was $\phi_{mob} = 1^o$ and, for simplicity, the cohesion part of the limestone was kept constant as $c_{mob} = 3.3$kPa. The interface between soil and masonry was always taken as $1/3$ of the mobilized soil strength. The initial clay cohesion was taken as $c_{mob} = 1$kPa. The shear strain increment $\epsilon_{incr} = 5\%\gamma_u$ was used for both clay and limestone. $\gamma_u = 0.015$ was taken for the limestone.

Bridges Arch01 and Arch03

In a series of arch tests to collapse, Gilbert (1997) considers arches with the same geometry as the Salford arches but without the fill so there is no soil-structure interaction involved. The arch is likely to reach its peak load carrying capacity at a small radial displacement under the load of approximately 3mm or 0.1% of the arch span. At larger displacements the strength of the arch progressively

reduces, and a gross displacement (i.e. geometrically non-linear) analysis is ideally required. Since the present MSLA model does not take geometrical non-linearity into account, it may only be assumed to be valid while the strength reduction of the arch is negligible.

For Arch01, the predicted collapse load is 110kN compared to the actual collapse load of 128kN. Figure 5.20 shows the soil strength mobilization contours at 3mm of radial displacement, indicating that the soil strength under the footing is fully mobilized whilst the average mobilization factor on the passive side is approximately 0.25 (the average mobilization factor only takes account of straining elements). It also indicates that the soil near the region of the left abutment is being mobilized. According to figure 5.21, there is quite large movement of the right abutment into the soil, which is what was observed in the experiment.

Figure 5.22 shows the velocity vectors provided by the MSLA and the PIV. It can be seen that on the passive side of the arch the slope of velocity vectors are similar (at approximately $45°$). This is in contrast to the FELA model, where the slope of velocity vectors was very high (approximately $80°$). As is shown in figure 5.15, the MSLA model predicts that the arch will move slightly when the load reaches around 50kN. Under this load, the soil under the footing is being mobilised.

For Arch03, the predicted collapse load is 138kN compared to the actual collapse load of 145kN. The larger bridge capacity compared to Arch01 was due to the fixed abutments in this test. This feature demonstrates that the MSLA model is more realistic than the FELA model (recall that in chapter 4 there was no difference in load and mechanism for Arch01 and Arch03). In fact, fixing the abutment is likely to increase the bridge capacity. Figure 5.16 shows the load-radial displacement curve provided by the MSLA model. It shows that when the load is less than 80kN, there is no arch movement and the soil under the load is mobilizing. This compares reasonably well with the experiment, where the first crack was identified at an applied load of 80kN.

Bridge Arch02

Bridge	MSLA	Experiment	%Difference
Arch01	110	128	14
Arch02	95	90	5.5
Arch03	138	145	4.8
Arch05	281	360	21.9
Arch06	198	240	17.5

TABLE 5.8: Predicted collapse loads (kN) of Salford bridge tests

Clay model	MSLA	Experiment
1	113	
2	95	90
3	118	

TABLE 5.9: Predicted collapse loads (kN) of Arch02 for different clay models

Recall that in chapter 4, the FELA model of Arch02 always predicted local soil failure regardless of the soil strength. This unrealistic mode is a consequence of the fact that it is inappropriate to assume full shear strength is mobilized everywhere. In this section, the MSLA model will be used to re-analyze this bridge. As in figure 5.10, the obtained data from triaxial clay tests were quite variable. A back-analysis is therefore required to find the most appropriate model. Applying three approximate clay models for Arch03, the predicted collapse loads are shown in table 5.9. The collapse load obtained from clay model 2 is 95kN and is the value closest to the test load. Figure 5.17 shows the actual and predicted load-deflection for the Arch02. The MSLA predicts that there in no arch movement when the applied load is less than 50kN. Figures 5.20 shows that both limestone and clay under the footing are fully mobilised, whilst the soil in the passive side is not. The failure mechanism shown in figure 5.21 is similar to the experimentally observed mechanism, where sliding of the abutment remote from the load was observed. As is evident from figure 5.24 and 5.25, the slope of the velocity vectors from the MSLA model and the PIV results are quite different. The slope vector given by the MSLA is much greater and it was approximately 50° while for the PIV, it was only around 20°.

Bridges Arch05 and Arch06

From the experimental load displacement curves shown in figures 5.18 to 5.19, it can be seen that in the presence of near-road surface reinforcement ensures that peak capacity is only reached when arch displacements are very large. For three bridges (Arch01, Arch02 and Arch03), the ultimate collapse loads are achieved at approximately 15mm radial displacement. However for bridges Arch05 and Arch06, the maximum loads are reached at approximately 40mm and 60mm radial displacement respectively. In the Arch06 test, when the applied load reached approximately 240kN and 40mm of radial displacement (measured under the load), the abutments were changed from free to fixed. Based on the behaviour of Arch05, where the maximum load was reached at 40mm displacement, it is reasonable to consider that 240kN is the maximum load for Arch06 with free abutments.

From table 5.8, the predicted collapse loads for Arch05 and Arch06 are 281kN and 198kN, which differ by 21.9% and 17.5% from the actual collapse loads. Figure 5.20 shows that for both bridges, the soil is not fully mobilized either on the loaded side or the passive side of the arch. As is evident from figures 5.26 to 5.29, the slope of the velocity vectors from the MSLA and the PIV are also found to be similar. The failure mechanisms depicted in figure 5.21 are also found to be similar to the experiments.
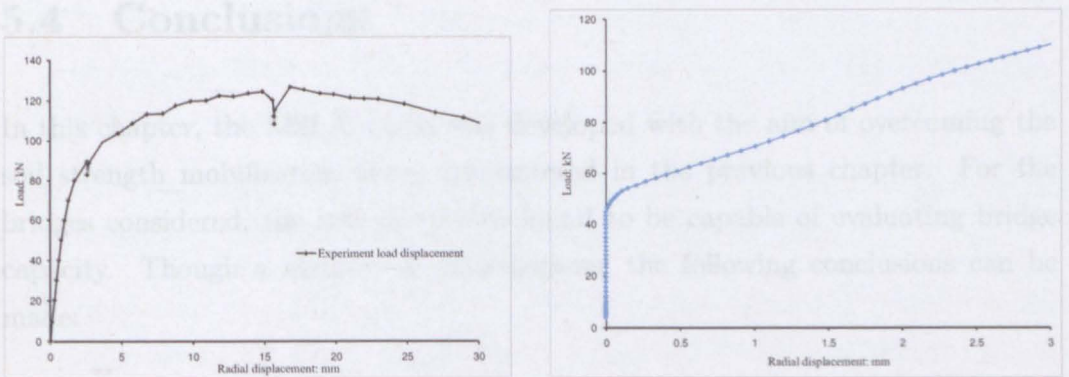
FIGURE 5.15: Actual and predicted load-deflection response of Arch01
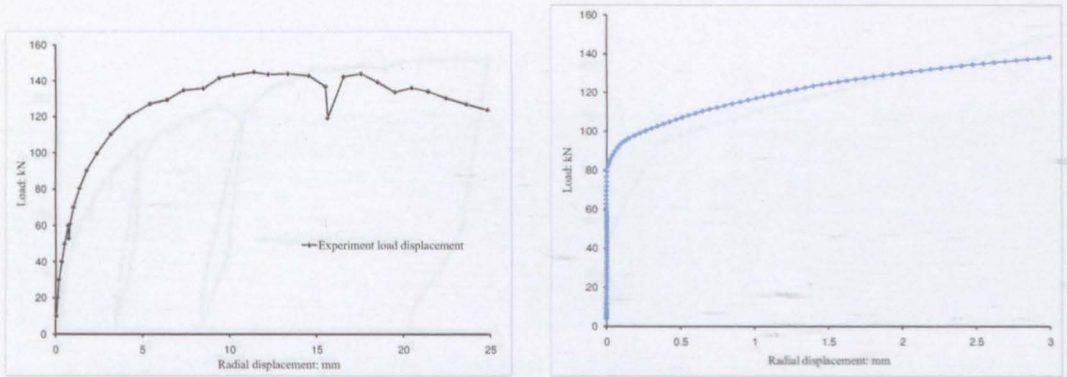
FIGURE 5.16: Actual and predicted load-deflection response of Arch03
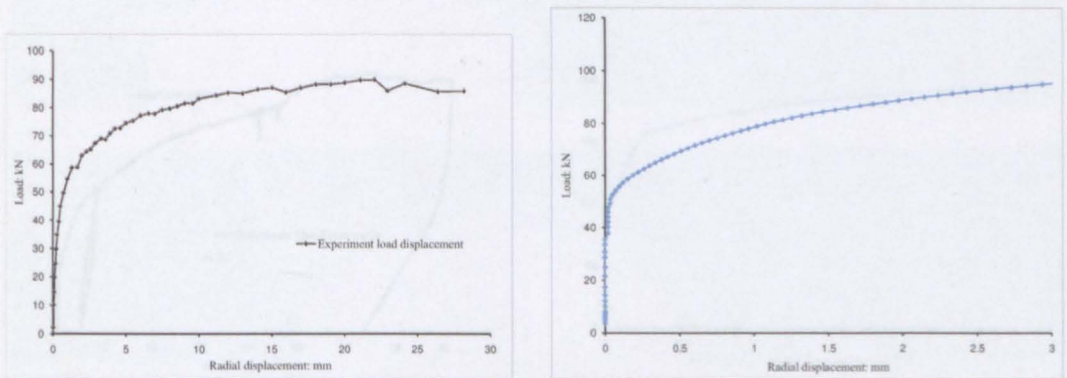
FIGURE 5.17: Actual and predicted load-deflection response of Arch02

5.4   Conclusions

In this chapter, the MSLA model was developed with the aim of overcoming the soil strength mobilization issues encountered in the previous chapter. For the bridges considered, the new method is found to be capable of evaluating bridge capacity. Though a number of examinations, the following conclusions can be made:

1. Simple soil strength mobilization analysis (MSD) can be used to assess bridge capacity. However, it can not be applied for certain cases, e.g. when a local footing failure has occurred.
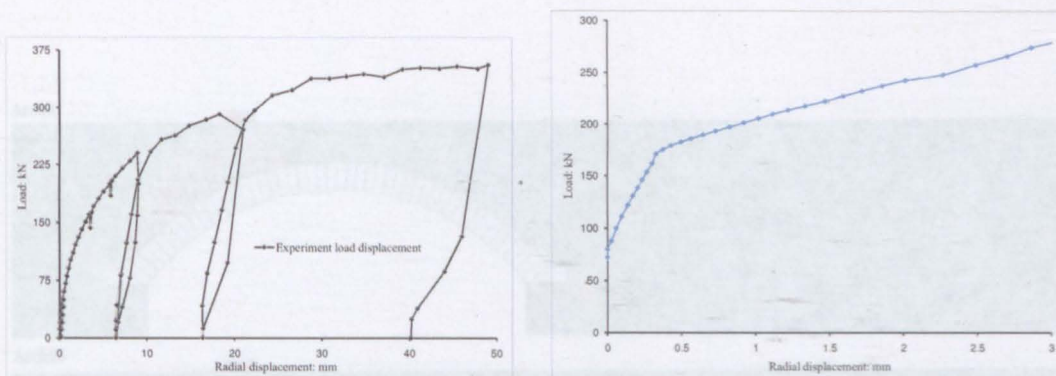
FIGURE 5.18: Actual and predicted load-deflection response of Arch05
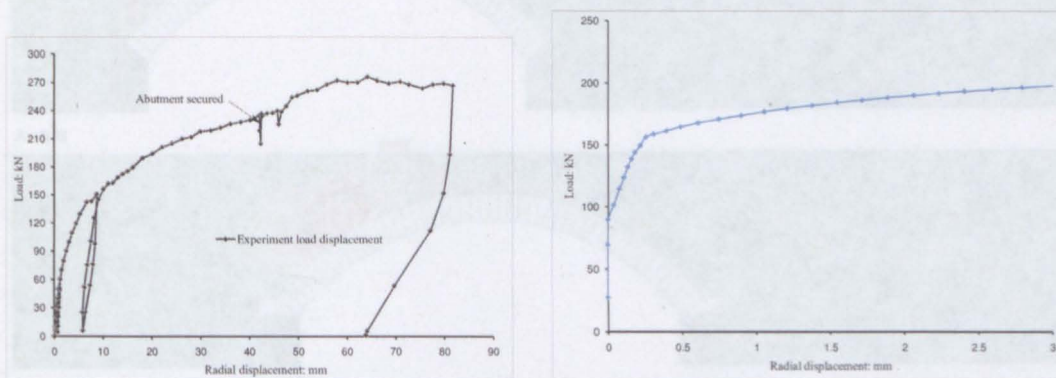
FIGURE 5.19: Actual and predicted load-deflection response of Arch06

2. In the case of bridges without near-road surface reinforcement, the soil strength is likely to be fully mobilized under the load whilst on the passive side, the soil is not fully mobilized.

3. For bridges with near-road surface reinforcement, the soil is unlikely to be fully mobilized either on the active or passive side of the arch.

4. In contrast to traditional kinematic limit analysis where the result is a displacement rate, the proposed MSLA model can be used to evaluate actual displacements. For the settlement of a strip footing on a cohesive soil, the MSLA solution predicts the actual load-displacement curve reasonably well (to within 20% in terms of displacements), compared with finite element analysis.
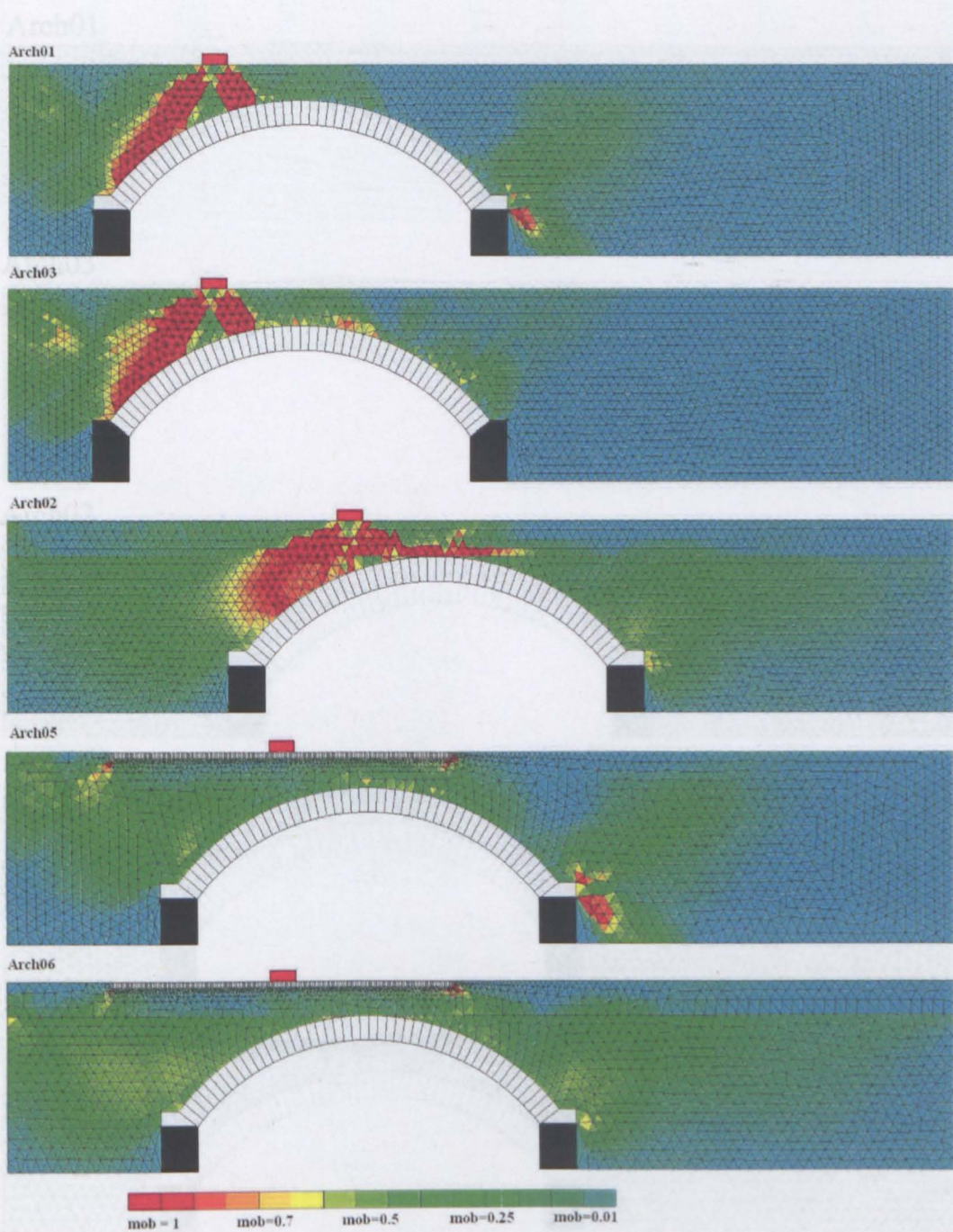
FIGURE 5.20: Variation of soil strength mobilization

Arch01

Arch03

Arch02
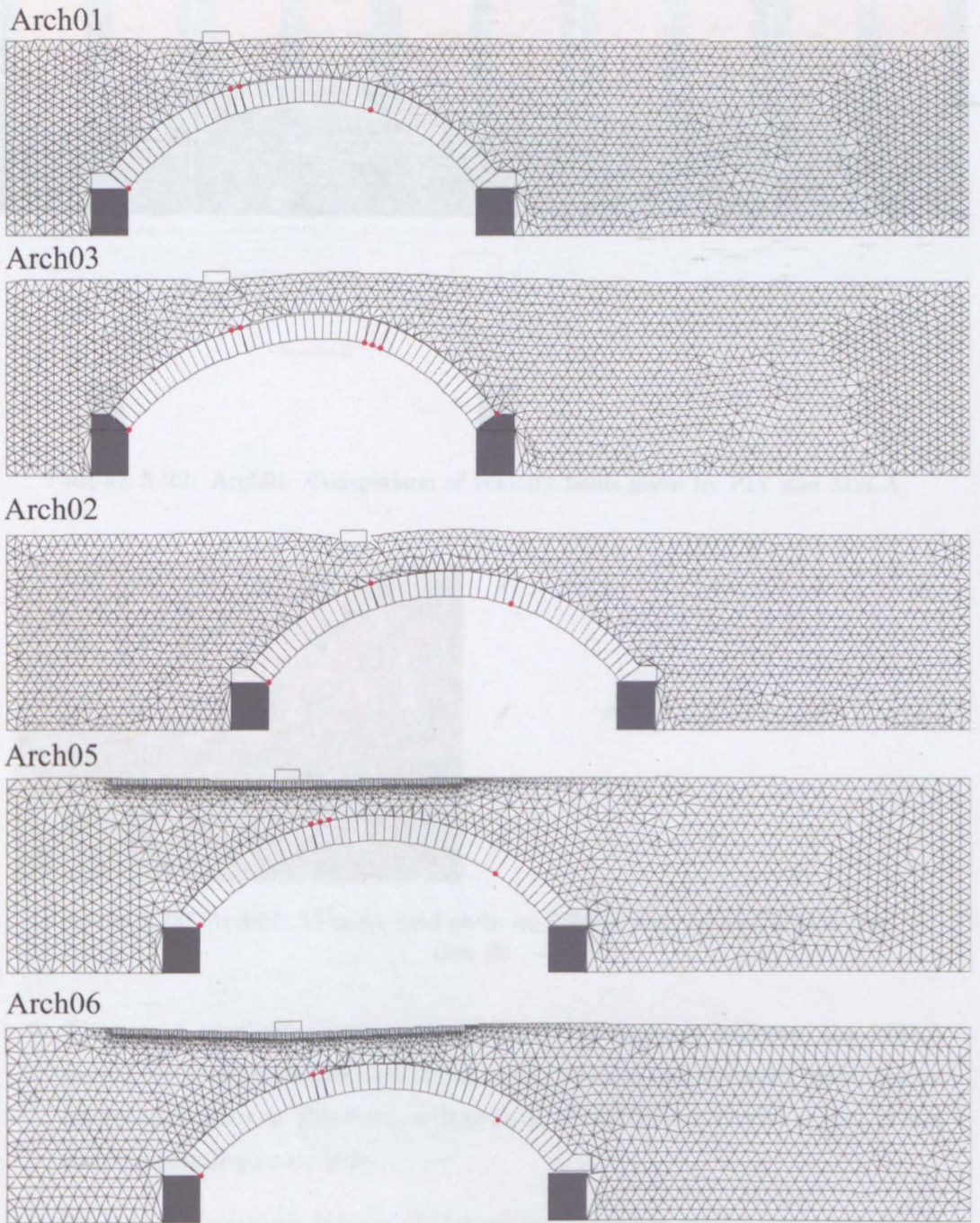
Arch05

Arch06

FIGURE 5.21: Deformed shape of soil and arch
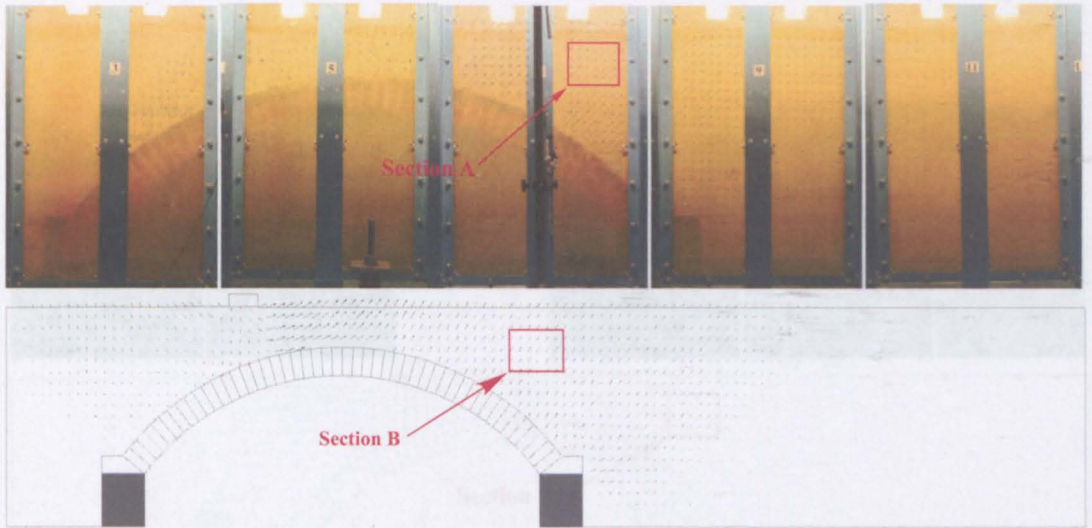
FIGURE 5.22: Arch01: Comparison of velocity fields given by PIV and MSLA
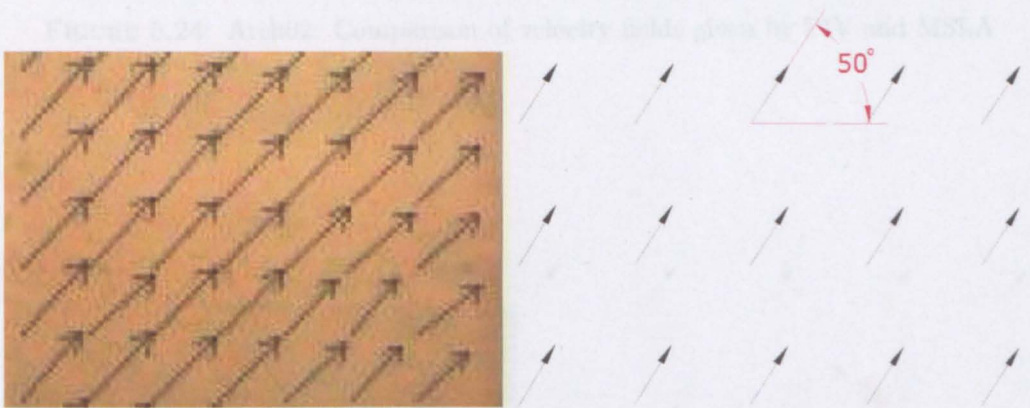
FIGURE 5.23: Arch01: Velocity field given by PIV(Section A) and MSLA (Section B)

5. Through a number of investigations on bridge tests to collapse, the MSLA model has demonstrated that it can overcome the soil strength mobilization issues encountered. However, a drawback of the MSLA model is that it is a time-consuming procedure.

6. Providing near-road surface reinforcement by using steel beams can significantly improve bridge load carrying capacity. In the present study, bridge capacity can be increased by at least a factor of 2.
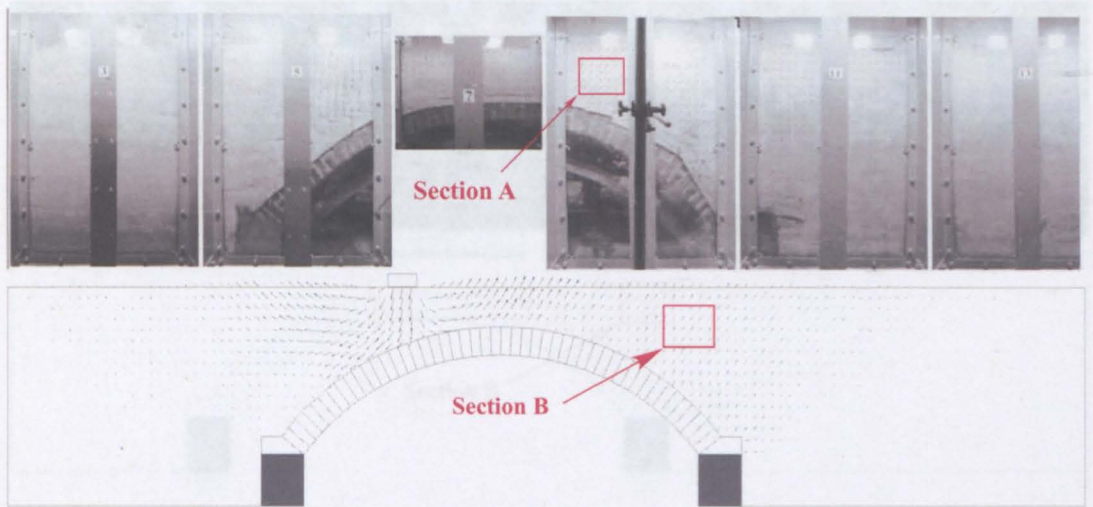
FIGURE 5.24: Arch02: Comparison of velocity fields given by PIV and MSLA
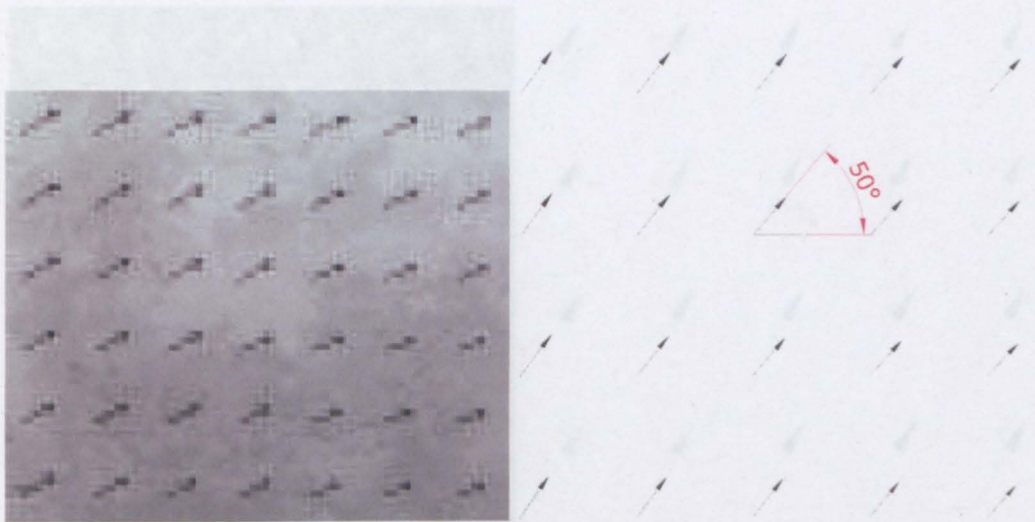
FIGURE 5.25: Arch02: Velocity field given by PIV(Section A) and MSLA (Section B)
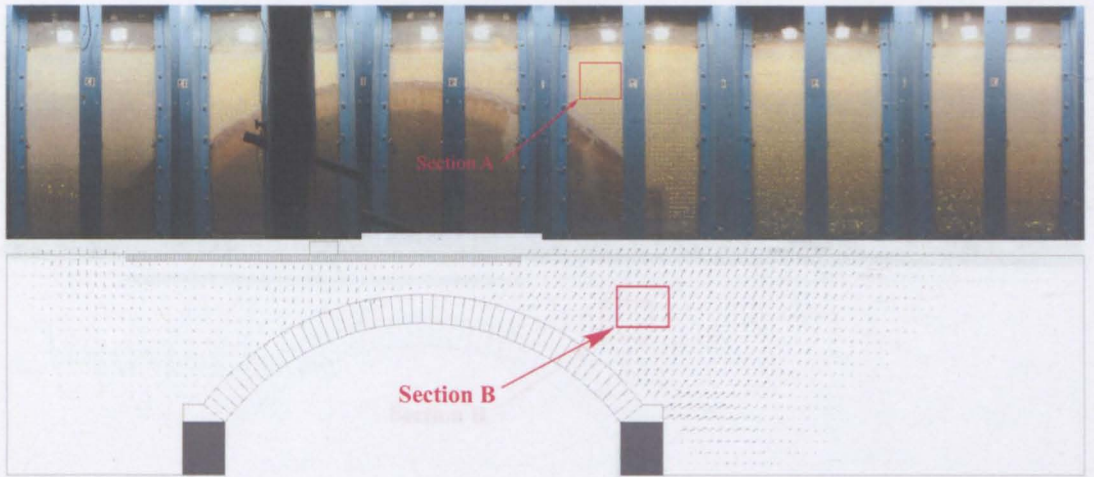
FIGURE 5.26: Arch05: Comparison of velocity fields given by PIV and MSLA
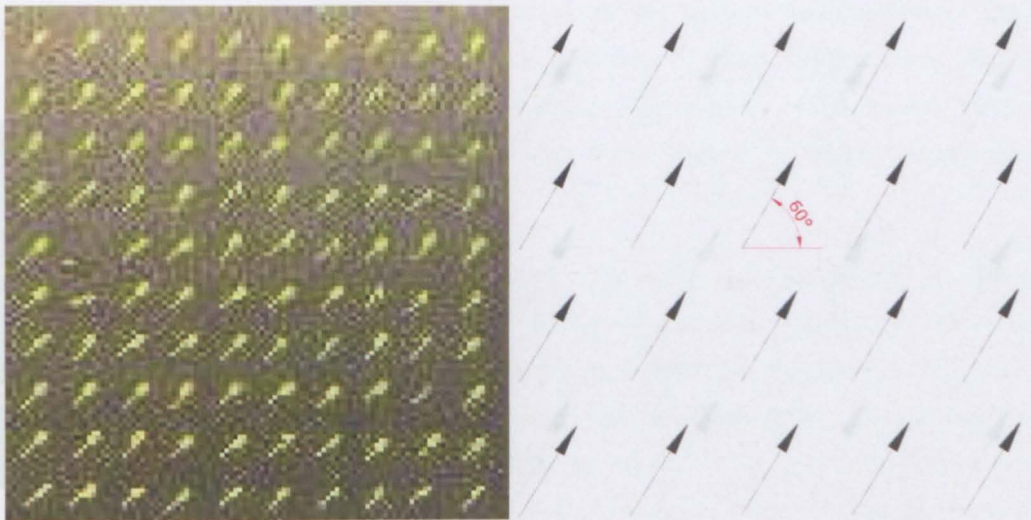
FIGURE 5.27: Arch05: Velocity field given by PIV(Section A) and MSLA (Section B)
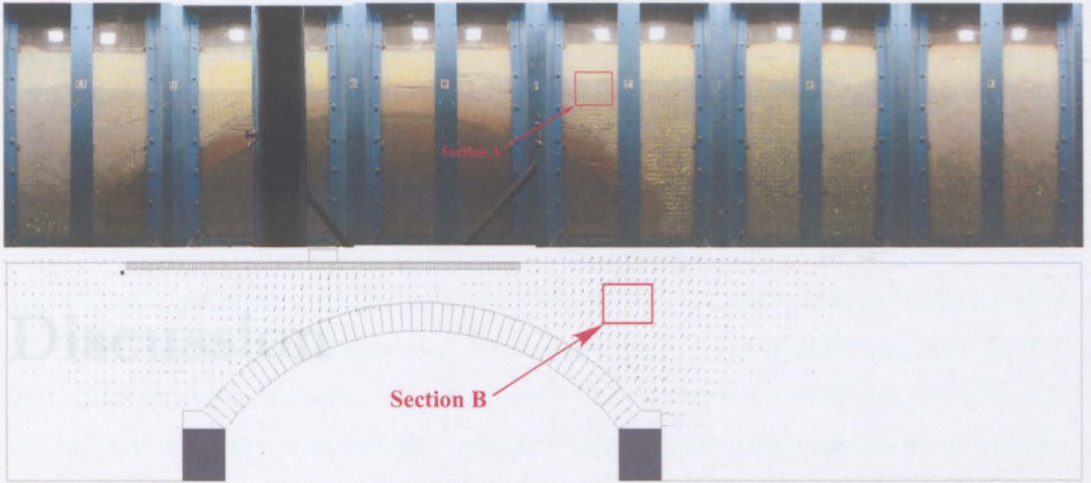
FIGURE 5.28: Arch06: Comparison of velocity fields given by PIV and MSLA

The overall objective of this research has been to establish a general computational limit analysis model for the practically important soil-structure interaction problem found when analysing masonry arch bridges. However, the finite element limit analysis model developed can be applied to a variety of other SSI problems; examples include problems involving earth retaining walls, slopes, and masonry tunnel
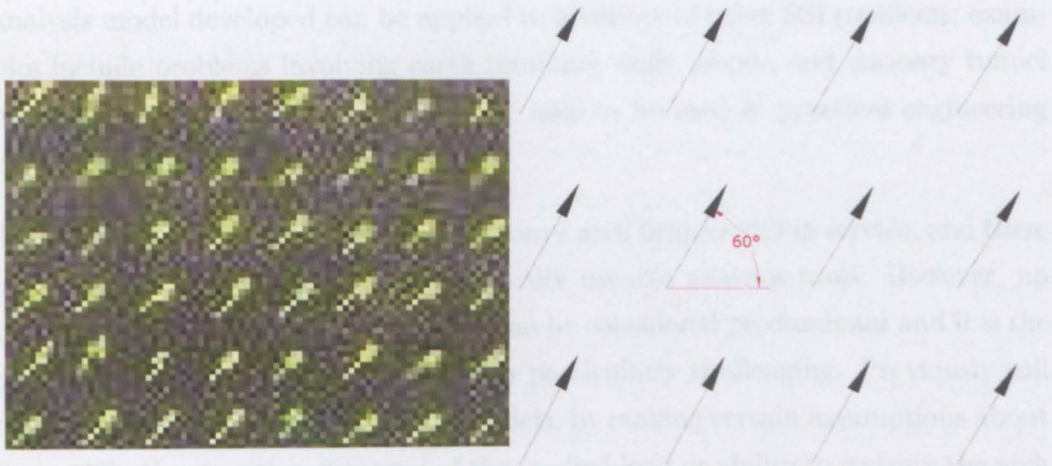
FIGURE 5.29: Arch06: Velocity field given by PIV(Section A) and MSLA (Section B)

Chapter 6

Discussion

6.1 Introduction

The overall objective of this research has been to establish a general computational limit analysis model for the practically important soil-structure interaction problem found when analysing masonry arch bridges. However, the finite element limit analysis model developed can be applied to a variety of other SSI problems; examples include problems involving earth retaining walls, slopes, and masonry tunnel linings. The model developed should be able to be used in practical engineering projects as an assessment or design tool.

There are a large number of existing masonry arch bridges still in service, and there is a strong need for efficient and practically useable analysis tools. However, up until now, no one existing analysis tool can be considered predominant and it is the presence of soil that makes the problem particularly challenging. Previously soil has been modelled only indirectly in models, by making certain assumptions about its contribution to either dispersal of the applied load or ability to restrain the arch barrel. This is acceptable for practical purposes provided that the assumptions are validated against experimental evidence. However, when 'non-standard' backfill materials are involved the likely influence of the soil cannot easily be estimated.

This thesis has tried to address this through the development of a holistic soil-structure interaction model using finite element limit analysis. However, through the previous 5 chapters, difficulties in developing a fast and reliable finite element limit analysis model for this application have become apparent. Here a number of limitations of the model developed will be discussed. In this chapter, the potential usefulness of a combined limit analysis - limit design synthesis model is also discussed (for application to the design of strengthening schemes for existing structures). Furthermore, in an attempt to overcome a number of the drawbacks of the FELA method, Smith & Gilbert (2007) have recently developed the so-called 'discontinuity layout optimization' (DLO) method, which is a conceptually simple but efficient limit analysis method. Whilst examining the usefulness of DLO, the author has developed an efficient scheme which allows mechanisms to be visualized for a given set of slip-lines. This scheme 'injects life' into the classical slip-line solutions which engineers are used to seeing as black and white line drawings in textbooks, but might often have trouble visualizing in terms of mechanisms of failure. This scheme has now successfully been incorporated in the commercially available LimitState:GEO software, available from www.limitstate.com.

6.2   The mesh dependency problem

When applied to soil bearing capacity problems, and subsequently to more complex backfilled masonry arch bridge problems, it has been found that when established formulations (e.g. that proposed by Sloan (1988)) were used, the geometry of the mesh used in the vicinity of singularities in the stress field influenced the results to an unacceptable degree. It may be observed that in the literature carefully tailored meshes have frequently been used in order to obtain solutions which are acceptably close to the true solution. Others have recently come to a similar conclusion, and have put forward enhanced finite element formulations to address this. Examples include the work of Borges et al. (1999), who focussed on obtaining upper bounds, and the adaptive mesh refinement schemes for the lower bound problem proposed by Lyamin et al. (2005). However, when carrying out a lower

bound analysis, the presence of stress singularities still need to be identified prior to performing an analysis. This issue does not affect the ability of finite element limit analysis to generate useful solutions from an academic standpoint, but does limit the usefulness of the method when applied to generic problems. Adaptive mesh refinement schemes can potentially overcome this problem, although it might be argued that the resulting analysis procedure is overly complex considering the simple rigid-plastic material idealization involved. Whilst enhanced formulations of the sort mentioned above were latterly trialled in the present project, and did enable tighter bounds on a true solution to be obtained, the initial mesh refinement problems stimulated Smith & Gilbert (2007) to consider alternative numerical approaches, eventually leading to the development of a new computational limit analysis technique, Discontinuity Layout Optimization (DLO).

6.3 The 'locking' problem

The so-called 'locking' problem (Nagtegaal and et al (1974)) causes major problems for many finite element limit analysis formulations. Although when treating plane strain problems the use of higher order elements can overcome this, use of these leads to large numbers of variables and constraints being present in the Mathematical Programming (MP) matrix. Therefore, the successfulness of this strategy will largely depend on the efficiency of the mathematical optimization solver used. The locking problem is even more troublesome when dealing with axisymmetric and three dimensional problems. It is evident from figure 6.1 that for three dimensional elements, almost all common types of finite elements will be prone to the locking problem (*the locking problem will occur when the ratio between degrees of freedom and constraints is less than* 1). Although in Lyamin et al. (2007), constant strain tetrahedra arranged in a cube have been used when analysing the bearing capacity of a footing, it should be noted that the mesh has to be carefully arranged in a specific way. It can be surmised that unless an efficient means of overcoming the locking problem can be found, the usefulness of FELA will be severely limited.
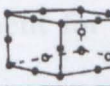
Element Type and Arrangement	Constraints Element	Ratio Nodes Elements	Ratio Deg.Freedom Constraints
5 constant strain tetrahedra in cube; cubes in regular lattice	1	1/5	3/5
8-node isoparametric cubes in regular lattice	7	1	3/7
5 linear strain tetrahedra in cube; cubes in regular lattice	4	7/5	21/20
20-node isoparametric cubes in regular lattice	≥ 16	4	≤ 3/4

FIGURE 6.1: The effect of mesh refinement on the ratio of total degrees of freedom to total number of incompressibility constraints for some common arrangements of three-dimensional finite elements (Nagtegaal and et al (1974))

6.4 Potential application of layout optimization to the design of strengthening existing structures

Reinforcement has been incorporated in plastic limit analysis models by workers such as Orduna & Lourenco (2003), Lourenco et al. (2004) and Chen et al. (2007) The main concern is that the addition of reinforcement may lead to undesirable brittle failure modes. For examples including near-surface reinforcement in a multi-ring brick work arch may increase the likelihood of ring separation. However, if bridge strength is inadequate to carry the given load, where should additional reinforcement be placed?

Limit analysis and design formulations are virtually identical, with the main difference being the differing goal of the optimization process (e.g. considering an equilibrium formulation, the 'analysis' objective is to maximise the load factor

whereas the 'design' objective might be to minimise the cost of reinforcing elements). Other constraints (i.e. equilibrium and yield constraints) remain unchanged. The CLADU integrated analysis and design software framework has been designed to take advantage of these similarities, making it relatively easy to synthesize 'optimum' retrofit reinforcement. Surprisingly, very little work has been done in this field (though Krabbenhoft et al. (2005) does use optimization to address the problem of designing sheet pile walls). Two examples are now considered (the mathematical formulation has been described in section 3.6).

Design reinforcement for an arch rib

Assessing an existing arch rib using usual standard limit analysis techniques may identify that the arch has insufficient strength. Engineers may wish to reinforce the arch, so therefore the location and the size of the requisite reinforcing elements needs to be identified. Figure 6.2 shows a simple example where truss bars are added to an under strength arch to permit a heavy applied load to be carried. For the current applied load, the best location and the sizes of the reinforcing bars are shown.
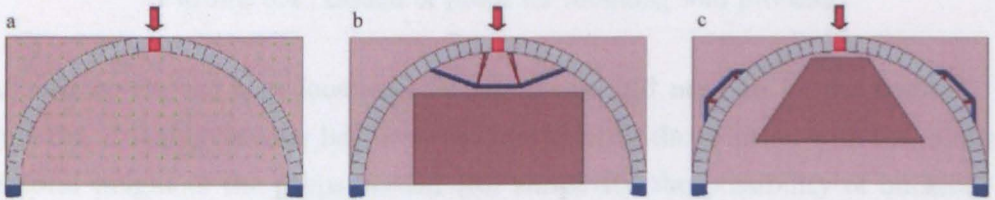
FIGURE 6.2: Design of reinforcement for an arch rib: (a) overloaded arch and design domain, (b) optimum layout of truss bar (rectangular prohibited zone), (c) revised layout of truss bars (trapezoidal prohibited zone)

Design of props for retaining wall

Suppose that a new building is to be constructed close to an existing retaining wall, as shown in figure 6.3. Engineers would need to carry out an analysis to determine whether the retaining wall is capable of sustaining the additional load, and, if not, to identify a solution (e.g. whether to move the building foundation somewhere else or to strengthen the existing wall). One strengthening option is to prop the

of the
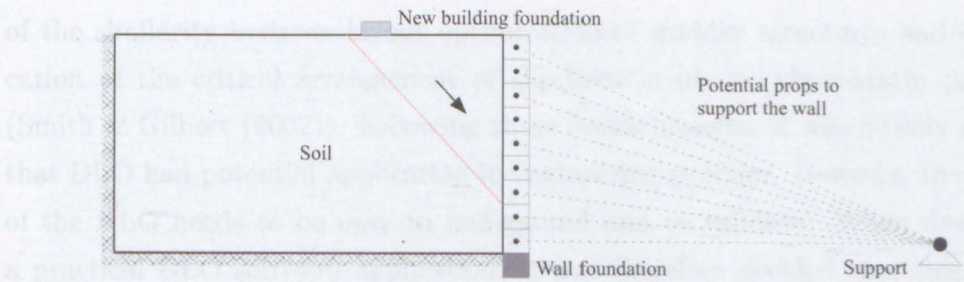
FIGURE 6.3: A retaining wall problem
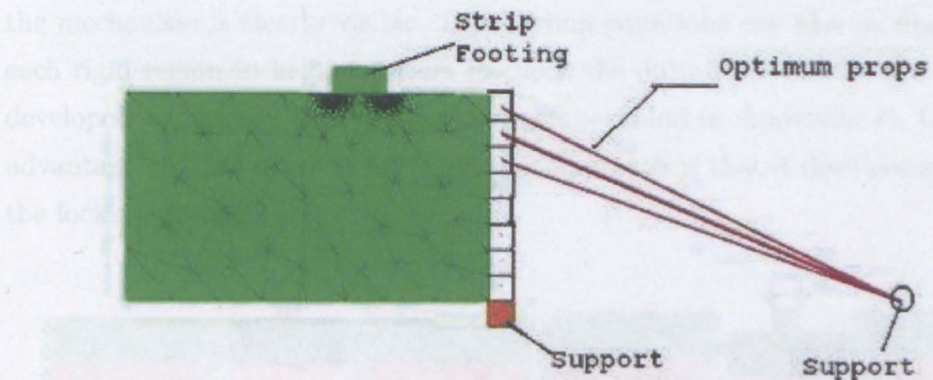
FIGURE 6.4: Design of props for retaining wall problem

wall. However, the best locations for the props still need to be determined. In figure 6.4, design synthesis has been used to identify the solution which minimizes the total weight of the props needed (for simplicity the possibility of buckling of the props has been ignored). This exciting method clearly has the potential to be a considerable time saver.

6.5 Discontinuity layout optimization

As has been mentioned in Chapter 2, the success of DLO relies on two important developments: (i) an *adaptive refinement scheme* which allows very large layout optimization problems to be solved (Gilbert & Tyas (2003)), and (ii) identification

of the similarity between layout optimization of gridlike structures and identifi-
cation of the critical arrangement of slip-lines in plastic plane-strain problems
(Smith & Gilbert (2007)). Following these breakthroughs, it was quickly realized
that DLO had potential application in engineering practice. However, the output
of the DLO needs to be easy to understand and to validate. When developing
a practical DLO software application, it was therefore decided that this should
be capable of clearly displaying the failure mechanism. This involves identifying
the rigid regions which lie between slip-lines, and then displacing these so that
the mechanism is clearly visible. Equilibrium equations can also be displayed for
each rigid region to help engineers to check the output. Details of the algorithm
developed to identify the rigid regions can be found in Appendix E. One of the
advantage of DLO over the finite element approach is that it does not suffer from
the locking problem.
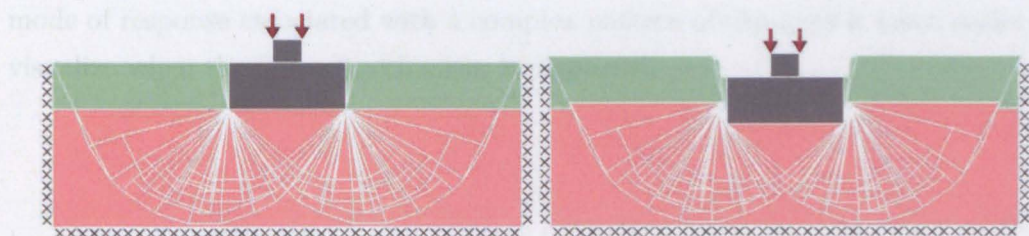
FIGURE 6.5: DLO Strip footing problem: optimum layout of slip lines and
displaced failure mechanism

FIGURE 6.6: DLO Slope problem: optimum layout of slip lines and displaced
failure mechanism

Figures 6.5, 6.6 and 6.7 illustrate various failure mechanisms generated using the
DLO-based LimitState:GEO software. In figure 6.5 the ability of DLO to identify
singularities around the edges of the footing automatically is evident (i.e. no
'model refinement' was necessary). It can also be seen from the figures that the
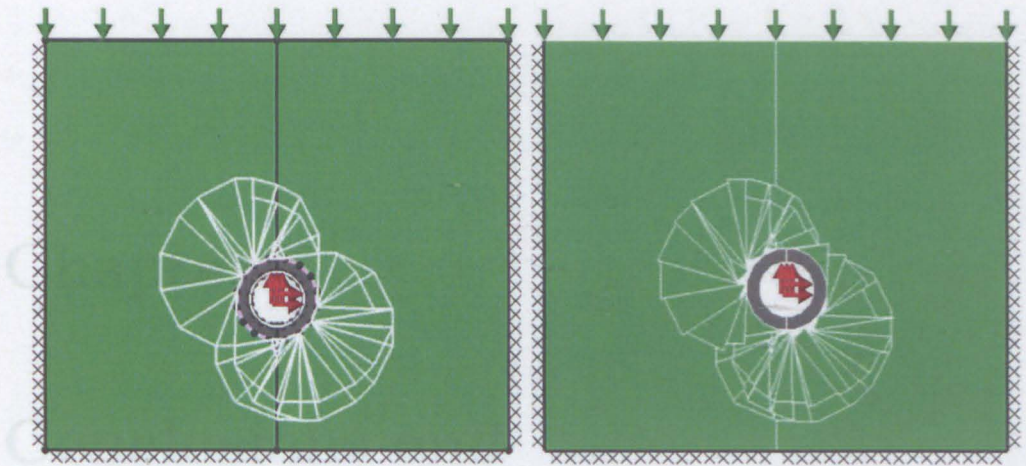
FIGURE 6.7: DLO Pile problem: optimum layout of slip lines and displaced failure mechanism

mode of response associated with a complex pattern of slip-lines is much easier to visualize when the failure mechanism is displaced.

Chapter 7

Conclusions and recommendations

7.1 Introduction

The purpose of this chapter is twofold. Firstly, the aims and objectives of the thesis, as set out in chapter 1, are re-visited. The developments described in Chapters 3,4 and 5 are discussed and compared with these goals in order to measure the success of the project. Secondly, as a result of issues that have arisen during the current study, further investigations are recommended.

7.2 Measuring the success of the project

7.2.1 Objective 1: development of a finite element limit analysis model for combined soil and masonry problems, and initial verification of this through application to a number of standard benchmark problems.

Finite element limit analysis models for the analysis soil-masonry structure problems were developed in Chapter 3. The numerical solutions obtained were verified against a number of benchmark problems and it has been found that the use of quadratic elements in the upper bound formulation leads to improved solutions. The use of higher order elements also prevents the 'locking' problem from occurring, and the mesh geometry does not need to be specially tailored in advance of an analysis. Furthermore, whereas traditionally a large number of linear planes are used to approximate the non-linear yield surface involved (if linear programming is employed), here an iterative solution algorithm which involves only refining the representation of the failure envelope where required has been used in order to maximize computational efficiency.

7.2.2 Objective 2: more in-depth verification of the model through application of this to a number of full scale bridge tests.

Although the developed finite element limit analysis model is able to qualitatively predict the mode of response of the soil-arch system, when peak soil strengths are used in the analysis the model fails to accurately predict bridge bearing capacity. As has been described in Chapter 4, through comparison with results from bridge tests conducted at Salford University, FELA significantly overestimates the experimentally observed collapse loads when peak soil strength are used in the

analysis. This is due to the fact that the peak strength of the soil is unlikely to be everywhere simultaneously mobilized .

7.2.3 Objective 3: implementation of enhancements to the model as proves necessary.

Mobilization of soil strength is a particularly significant issue in soil-arch interaction problems. This is because whilst soil strengths increase as movements become larger, conversely the structure rapidly starts to lose strength when movements become significant. Thus a key project finding is that the use of peak soil strength parameters in limit analysis models will often be inappropriate (when the soil is modelled explicitly). However, use of mobilized strengths proved to be a promising way forward, yielding much closer correlation with experimental data. The approach used has similarities with the 'Mobilized Strength Design' method advocated e.g. by Osman & Bolton (2005), and was illustrated in Chapter 5 . Subsequently a more sophisticated incremental analysis method in which mobilized strengths are increased according to the magnitude of strain within individual elements has been investigated. As has been presented in Chapter 5, it has been termed the MSLA method. However, one drawback of the MSLA model is that it is a time-consuming procedure.

7.2.4 Objective 4: consideration of other potential applications of the developed numerical model.

Other potential applications of the model developed have been briefly discussed in Chapter 6. It has been shown that the combination of finite element limit analysis and layout optimization provides a potentially useful tool for engineers.

7.2.5 Concluding remarks

The works in this thesis have been presented at two international conferences and they can be found at Nguyen et al. (2007) and Gilbert et al. (2007). The work was also selected for presentation at the IStructE Young Researchers conferenceheld in London in 2007. The project website is featured in the EPSRC 'Beyond Brunel' website (see: http://cladu.shef.ac.uk/projects/holistic/). Further details of the developments to the DLO method as described in Chapter 6 are also expected to be published in due course. Throughout the six chapters, it is clear that the objectives of this thesis have been largely met. However, there are several areas that warrant further consideration; these are described in the next section.

7.3 Recommendation for further work

7.3.1 On the development of computational limit analysis and design synthesis

Various issues relating to the conventional *continium* finite element limit analysis method have been discussed throughout this thesis. Two of the most challenging are (i) the issue of mesh sensitivity, and (ii) the volumetric locking problem. Although, mesh adaptivity can be used to improve the solution, examples are the works of Lyamin et al. (2005); Christiansen & Pedersen (2001), this is computationally expensive because re-meshing is required. Moreover, when the problem involves strong singularities, adaptive mesh refinement is not always applicable. Recently, the meshfree method has been considered as an attractive alternative to the finite element method. However, this method has not yet been widely applied in the field of computational limit analysis, early studies have been performed by Canh et al. (2008) and Chen et al. (2008). Further study of the meshfree method for the application to geotechnical problem is thus recommended. The volumetric locking problem is rather more difficult to overcome and up until now an efficient method to address this does not exist. However, as has been indicated by Askes

et al. (1999); Dolbow & Belytschko (1999); Mendez (2001), for some particular cases, the meshfree method can alleviate the locking problem.

As an alternative to the traditional *continuum* approach, the DLO method provides an exciting new approach. At present, only translational failure modes are considered, and further study is required so that rotational modes can be simulated. Moreover, at present the DLO method is an upper bound approach, and it remains unclear whether it is possible to develop a lower bound formulation. Since limit analysis and design synthesis problems are virtually identical, the question of whether *continuum* finite element limit analysis formulations can be applied to design problems naturally arises; this deserves more in-depth study. As discussed in Chapter 6, the combination of limit analysis and design synthesis offers a great potential application for practical engineers. It is thus recommended that further work in this field be conducted.

7.3.2 On the development of finite element limit analysis models for the assessment of masonry arch bridges

Soil strength mobilization is an important issue to consider when analyzing masonry arch bridge. The MSLA method has been introduced to tackle this problem. However, it is a computationally expensive procedure and thus it may impractical for use in practice. Moreover, the MSLA method currently does not take account of gross displacement of the arch. Thus further work is required to improve the MSLA method.

Up until now, limit analysis software has generally focussed on solving two dimensional problems. Consequently when such software is applied to real, three-dimensional bridges, certain assumptions have to be made about the third dimension. Extending the FELA method to three dimensions is an obvious next step. A 3D model will be able to tackle problems involving asymmetric loading and could model skew bridges. It will also enable the assessment of masonry domes and vaulted structures.

7.3.3   On the strengthening of masonry arch bridges

In this thesis, it has been seen that near-road surface reinforcement using steel beams greatly increases bridge load carrying capacity, at least by a factor of 2. This strengthening method is simple, and relatively quick to construct, leading to relatively little traffic disruption. Furthermore, during experiments and also from numerical models, it was found that large movements of the abutment remote from the load occur when such reinforcement is used. This suggests that further increase in bridge capacity could be achieved if this abutment was more securely fixed. Investigation on the influence of near-road surface concrete slab reinforcement could also be investigated.

References

Alwis, W. 2000 Discrete element slip model of plasticity. *Engineering Structures* **22**, 1494-1504.

Anderheggen, D. & Knopfel, H. 1972 Finite element limit anlysis using linear programming. *International Journal Solids Structures* **3**, 1413-1431.

Andersen, D., Christiansen, D. & Overton, L. 1998 Computing limit loads by minimizing a sum of norms. *SIAM Journal on Scientific Computing* **19**, 1046-1062.

Andersen, D. & Christiansen, E. 1995 Limit analysis with dual affine scaling algorithm. *Journal of Computational and Applied Mathematics* **59**, 233-243.

Archie-M 2007 *Masonry arch bridge software. http://www.obvis.com/*, version 2.3 edn, OBVIS Ltd.

Askes, H., Borst, R., & Heeres, O. 1999 Condition for locking-free elasto-plastic analyses in the element-free galerkin method. *Computer Methods in Appllied Mechanics and Engineering* **173**, 99-109.

BA16 1997 The assessment of highway bridges and structures. *The Highways Agency* **3**.

BD21 2001 The assessment of highway bridges and structures. *The Highways Agency* **3**.

Begg, D. & Fishwick, R. 1995 Numerical analysis of rigid block structures including sliding. *Proceedings of Third International Symposium on Computer Methods in Structural Masonry* pp. 1-7.

Belytschko, T., Lu, Y. & Gu, L. 1994 Element-free Galerkin methods. *International Journal for Numerical Methods in Engineering* **37**, 229–256.

Betti, M., Drosopoupos, G. & Stavroulakis, G. 2008 Two non-linear finite element models developed for the assessment of failure of masonry arches. *Comptes Rendus Mecanique* **336**, 42 53.

Bolton, M., Powrie, W. & Symons, I. 1989 The design of in-situ walls retaining overconsolidated clay: Part I short term behaviour. *Ground Engineering* **22**, 44–48.

Bolton, M., Powrie, W. & Symons, I. 1990 The design of in-situ walls retaining overconsolidated clay: Part II long term behaviour. *Ground Engineering* **23**, 22–28.

Bolton, M. & Sun, H. 1991 Designing foundations on clay to limit immediate movements. *Proceedings 4th International Conference on Ground Movements and Structures, Cardiff* .

Boothby, T. 1994 Stability of masonry piers and arches including sliding. *Journal of Engineering Mechanics* **120**, 304–319.

Boothby, T., Domalik, D. & A, D. 1998 Service load response of masonry arch bridges. *Journal of Structural Engineering* **6**, 79–86.

Borges, L. 2001 An adaptive approach to limit analysis. *International Journal of Solids and Structures* **38**, 1707–1720.

Borges, L., Feijoo, R. & Zouain, N. 1999 A directional error estimator for adaptive limit analysis. *Mechanicas Research Communications* **26**.

Bottero, A., Negre, R. & Pastor, J. 1980 Finite element method and limit analysis theory for soil mechanics problems. *Computer Methods in Applied Mechanics and Engineering* **22**, 131–149.

Brencich, A. & Francesco, U. 2004 Assessment of multispan masonry arch bridges. *ASCE: Journal of Bridge Engineering* **11**, 582–590.

Burroughs, P., Hughes, T., Hee, S. & Davies, M. 2002 Passive pressure development in masonry arch bridges. *Procceedings of the Institution of Civil Engineers - Structures and Buildings* **152**, 331–339.

Callaway, P. 2007 *Soil-structures interaction in masonry arch bridges*, PhD thesis, University of Sheffield.

Canh, L., Gilbert, M. & Askes, H. 2008 Limit analysis of plates using the efg method and second-order cone programming. *Internation Journal for Numberical Methods in Engineering : Submitted* .

Capsoni, A. & Corradi, L. 1997 A mixed finite element model for plane strain elastic-plastic analysis. *Computer Methods in Applied Mechanics and Engineering* **141**, 67–79.

Casciaro, R. & Cascini, L. 1982 A mixed formulation and mixed finite elements for limit analysis. *International Journal for Numerical Methods in Engineering* **18**, 211–243.

Cavicchi, A. & Gambarotta, L. 2005 Collapse analysis of masonry bridges taking into account arch-fill interaction. *Engineering Structures* **27**, 605–615.

Cavicchi, A. & Gambarotta, L. 2007 Lower bound limit analysis of masonry bridges including arch-fill interaction. *Engineering Structures* **29**, 3002–3014.

Chen, J., Yin, J. & Lee, C. 2004 Rigid finite element method for upperbound limit analysis of soil slopes subjected to pore water pressure. *ASCE: Journal of Engineering Mechanics* **130**(8), 886–893.

Chen, S., Liu, Y. & Cen, Z. 2008 Lower-bound limit analysis by using the efg method and non-linear programming. *Internation Journal for Numberical Methods in Engineering* **74**, 391–415.

Chen, W. 1975 *Limit analysis and soil plasticity*. Elsevier Scientific Publishing, Amsterdam.

Chen, Y.. Ashour, A. & Garrity, S. 2007 Modified four-hinge mechanism analysis for masonry arches strengthened with near-surface reinforcement. *Engineering Structures* pp. 1864-1871.

Choo, B.S. Coutie, M. & Gong, N. 1990 Analysis of masonry arch bridges by a finite element method. *Proceedings of the Forth Rail Bridge Centenary International Conference* pp. 381-392.

Christiansen, E. 1991 Computation of the collapse state in limit analysis using the LP primal affine scaling algorithm. *Journal of Computational and Applied Mathematics* **34**, 47-63.

Christiansen, E. & Andersen, D. 1999 Computation of collapse states with Von Mises type yield condition. *International Journal for Numerical Methods in Engineering* **46**, 1185-1202.

Christiansen, E. & Pedersen, O. 2001 Automatic mesh refinement in limit analysis. *International Journal for Numerical Methods in Engineering* 50(6), 1331-1346.

CIRIA 2006 Masonry arch bridges condition, appraisal and remedial treatment. *London* .

Ciria, H. & Peraire, J. 2004 Computation of upper and lower bounds in limit analysis using second-order cone programming and mesh adaptivity. *Proceedings of 9th Specialty Conference on Probabilistic Mechanics and Structural Reliability, Albuquerque* .

Coulomb, C. 1773 Essai sur une application des regies des maximis et minimis a quelques problemes de statique relatifs a l'architecture. *Mem. pres. pardiv. savants* **7**, 343-382.

Crisfield. M. & Packham, A. 1987 A mechanism program for computing the strength of masonry arch bridges. *Transport and Road Research Laboratory* **124**.

Dantzig, G. 1963 *Linear programming and extensions*. Princeton University Press, New York, USA.

Davey, N. 1953 Tests on road bridges. *National Building Studies, Research Paper No 16. London:HMSO* .

de Saint-Venant, B. 1870 Memoire sur i'etablissement des equations differentielles des mouvements interieurs operes dans les corps solides ductiles au dela des limites ou i'elasticite pourrait les ramener a leur premier etat. *C.R. Acas. Sci. Paris* **70**.

Dolbow, J. & Belytschko, T. 1999 Volumetric locking in the element-free Galerkin method. *International Journal for Numerical Methods in Engineering* **46**, 925–942.

Dorn, W., Gomory, R. & Greenberg, H. 1964 Automatic design of optimal structures. *J. de Mechanique* **3**, 25–52.

Drosopoulos, G., Stavroulakis, G. & Massalas, C. 2006 Limit analysis of a single span masonry bridge with unilateral frictional contact interfaces. *Engineering Structures* **28**, 1864–1873.

Drucker, D. 1952 A more fundamental approach to plastic stress-strain relations. *Proc. 1st US Nat. Congr. Appl. Meek, ASME, New York* pp. 487–491.

Drucker, D. 1954 Coulomb friction, plasticity and limit loads. *Journal of Applied Mechanics* **21**, 71–74.

Fanning, P. & Boothby, T. 2001 Three-dimensional modelling and full-scale testing of stone arch bridges. *Computers and Structures* **79**, 2645–2662.

Ferris, M. & Tin-loi, F. 2001 Limit analysis of frictional block assemblies as a mathematical program with complementarity constraints. *International Journal of Mechanical Sciences* **43**, 209–224.

Ford, T., Augarde, C. & Tuxford, S. 2003 Modelling masonry arch bridges using commercial finite element software. *The 9th International Conference on Civil and Structural Engineering Computing, Netherlands* .

Gid9 2008 *The mesh generator software. http://gid.cimne.upc.es*, 9.0 edn.

Gilbert, M. 1997 Gross displacement mechanism analysis of masonry bridges and tunnel linings. *Proceedings of the 11th International Brick/Block Masonry Conference. Shanghai* p. 473482.

Gilbert, M., Casapulla, C. & H.M., A. 2006 Limit analysis of masonry block structures with non-associative frictional joints using linear programming. *Computers and Structures* **84**, 873887.

Gilbert, M. & Melbourne 1994 Rigid-block analysis of masonry structures. *The Structural Engineer* **72**, 356–360.

Gilbert, M., Nguyen, D. & Smith, C. 2007 Computational limit analysis of soil-arch interaction in masonry arch bridges. *Proceedings of the 5th International Arch Bridges Conference, Madeira* pp. 633–640.

Gilbert, M. & Tyas, A. 2003 Layout optimization of large-scale pin-jointed frames. *Engineering Computations* **20**, 1044–1064.

Harvey, W. 2006 Some problems with arch bridge assessment and potential solutions. *The Structural Engineer* **84**, 45–50.

Harvey, W., Tomor, A. & Smith, F. 2005 A three dimensional model for masonry arch bridge behaviour. *Structural Engineering International* **2**, 4–7.

Hemp, W. & Chan, H. 1966 Optimum design of pin-jointed frameworks. *Report No 1015.66, Department of Engineering Science, Oxford* .

Heyman, J. 1966 The stone skeleton. *International Journal Solids and Structures* **2**, 249–279.

Heyman, J. 1982 *The masonry arch.* Ellis Horwood Limited.

Hill, R. 1948 Ma variadonal principle of maximum plastic work in classical plasticity. *Q.J. Meek Appl. Matk* **1**, 18–28.

Hughes, T. & Blackler, M. 1997 A review of the uk masonry arch assessment methods. *Procceeding of the Institution of Civil Engineers - Structural and Buildings* **122**, 0 11.

Hughes, T., Hee, S. & Soms, E. 2002 Mechanism analysis of single span masonry arch bridges usign a spreadsheet. *Procceedings of the Institution of Civil Engineers - Structures and Buildings* 4, 341-350.

Karmarkar, N. 1984 A new polynomial-time algorithm for linear programming. *Combinatorica* 4, 373-3954.

Khan, A. & Huang, S. 1995 *Continuum Theory of Plasticity*. Wiley-Interscience.

Kooharian, A. 1952 Limit analysis of voussoir (segmental) and concrete. *Journal of the american concrete institute* 24, 31728.

Krabbenhoft, K. & Damkilde, L. 2003 A general non-linear optimization algorithm for lower bound limit analysis. *International Journal for Numerical Methods in Engineering* 56, 165-184.

Krabbenhoft, K., Damkilde, L. & Krabbenhoft, S. 2005 Ultimate limit state design of sheet pile walls by finite elements and nonlinear programming. *Computers and Structures* 83, 383-393.

Livesley, R. 1978 Limit analysis of structures formed from rigid blocks. *International Journal for Numerical Methods in Engineering* 12, 1853-1871.

Loo, Y. & Yang, Y. 1991 Cracking and failure analysis of masonry arch bridges. *Journal of Structural Engineering* 117, 1641-1659.

Loukidis, D., Bandini, P. & Salgado, R. 2003 Stability of seismically loaded slopes using limit analysis. *Geotechnique* 5, 463-479.

Lourenco, P., Palacio, K. & Barros, J. 2004 Design recommendation for reinforced masonry arches. *Proceedings of the 4th International Arch Bridges Conference, Barcelona* pp. 583-592.

Lyamin, A., Salgado, R., Sloan, S. & Prezzi, M. 2007 Two and three dimensional bearing capacity of footings in sand. *Geotechnique* 57, 647-662.

Lyamin, A. & Sloan, S. 2002a Lower bound limit analysis using non-linear programming. *International Journal for Numerical Methods in Engineering* **55**, 573–611.

Lyamin, A. & Sloan, S. 2002b Upper bound limit analysis using linear finite elements and non-linear programming. *International Journal for Numerical and Analytical Methods in Geomechanics* **26**, 181–216.

Lyamin, A., Sloan, S., Krabbenhoft, K. & Hjiaj, M. 2005 Lower bound limit analysis with adaptive remeshing. *International Journal for Numerical Methods in Engineering* **63**, 1961–1974.

Lysmer, J. 1970 Limit analysis of plane problems in soil mechanics. *ASCE: Journal of Soil Mechanics and Foundations Division* **96**, 1311–1336.

Mabon, L. 2002 Assessment, strengthening and preservation of masonry structures for continued use in todays infrastructure. *IABSE Symposium Report, Melbourne* **86**, 565–572.

Makrodimopoulos, A. & Martin, C. 2005 Limit analysis using large-scale SOCP optimization. *13th ACME Conference - University of Sheffield* **96**, 1311–1336.

Makrodimopoulos, A. & Martin, C. 2006 Advances in numerical upper bound limit analysis. *Proceedings of the International Conference in Memoriam of Prof. P.D. Panagiotopoulos* pp. 213–220.

Martin, C. 2003 *User Guide for ABC Analysis of Bearing Capacity. OUEL Report No. 2261/03*, version 1.0 edn, University of Oxford.

Martin, C. & Makrodimopoulos, A. 2008 Finite-element limit analysis of MohrCoulomb materials in 3D using semidefinite programming. *ASCE: Journal of Engineering Mechanics* **134**, 339–347.

Melbourne, C. & Gilbert, M. 1995 The behaviour of multiring brickwork arch bridges. *The Structural Engineer* **73**, 39–47.

Mendez, S. 2001 Meshfree methods and finite elements: Friend or foe. *Doctoral thesis, Universitat Politecnica de Catalunya* .

Merifield, R., Sloan, S. & Yu, H. 1999 Rigorous plasticity solutions for the bearing capacity of two-layered clays. *Geotechnique* **49**, 471–490.

Merifield, R., Sloan, S. & Yu, H. 2001 Stability of plate anchors in undrained clay. *Geotechnique* **51**(2), 141–153.

Michalowski, R. & Shi, L. 1995 Bearing capacity of footings over two-layer foundation soils. *ASCE: Journal of Geotechnical Engineering* **121**, 421–428.

Mosek 2006 *The MOSEK optimization tools manual. http://www.mosek.com*, version 4.0 (revision 35) edn, Mosek ApS.

Mosley, W., Bungey, J. & Hulse, R. 1995 Structural and stress analysis. *Published by Elsevier,ISBN 0340631961, 9780340631966* .

Mosley, W., Bungey, J. & Hulse, R. 1999 *Reinforced concrete design, fifth edition.* PALGRAVE Houndmills, Basingstoke.

Motta, E. 1994 Generalized coulomb active earth pressure for a distanced surcharge. *ASCE: Journal of Geotechnical and Geoenvironmental Engineering* **120**, 1072–1079.

Nagtegaal, J., Parks, D. & Rice, J. 1974 On numerically accurate finite element solutions in the fully plastic range. *Computer Methods in Applied Mechanics and Engineering* **4**, 153–177.

Nash, S. & Sofer, A. 1996 Linear and non-linear programming.. *McGraw-Hill, London, UK* .

Ng, K. & Fairfield, C. 2004 Modifying the mechanism method of masonry arch bridge analysis. *Construction and Building Materials* **18**, 91–97.

Ng, K., Fairfield, C. & Sibbald, A. 1999 Finite-element analysis of masonry arch bridges. *Proceedings of the Institution of Civil EngineersStructures and Buildings* **134**, 119–127.

Nguyen, D., Gilbert, M. & Smith, C. 2007 Application of limit analysis to soil-structure interaction problems. *Proc. 10th Australia New Zealand Conference on Geomechanics* 1, 196–201.

Orduna, A. 2003 Seismic assessment of ancient masonry structures by rigid blocks limit analysis. *PhD Thesis: Universidade do Minho* .

Orduna, A. & Lourenco, P. 2003 Cap model for limit analysis and strengthening of masonry structures. *ASCE: Journal of Structural Engineering* 10, 1367–1375.

Osman, A. & Bolton, M. 2005 Simple plasticity based prediction of the undrained settlement of shallow circular foundations on clay. *Geotechnique* 55, 435–447.

Osman, A. & Bolton, M. 2006 Ground movement predictions for braced excavations in undrained clay. *Journal of geotechnical and geoenvironmetal engineering* 132, 465–477.

Owen, D., Peric, D., Petrinic, N., Brookes, C. & James, P. 1998 Finite/discrete element models for assessment and repair of masonry structures. *Proceedings of Internationl Conference of Arch Bridges-Rotterdam* pp. 195–204.

Page, J. 1987 Load tests to collapse on two arch bridges at Preston, Shropshire and Prestwood, Staffordshire. *TRRL Research report 110. Crowthorne. UK* .

Page, J. 1988 Load tests on two arch bridges at Torksey and Shinafoot. *TRRL Research Report 159, Crowthorne, UK* .

Page, J. 1989 Load tests to collapse on two arch bridges at strathmashie and barlac. *Departement of Transport. TRRL Research Report 201, Transport Research Laboratory, Crowthorne* .

Page, J. 1993 Masonry arch bridges. *HMSO* .

Pappin. J., Simpson, B., Felton, P. & Raison, C. 1986 Numerical analysis of flexible retaining walls. *International Conference Numerical Methods in Engineering: Theory and Applications, Swansea* 120, 213–242.

Pastor, J., Thai, T. & Francescato, P. 2003 Interior point optimization and limit analysis: an application. *Communications in Numerical Methods in Engineering* **19**, 779–785.

Peraire, J., Vahdati, M., Morgan, K. & Zienkiewicz, O. 1987 Adaptive remeshing for compressible flow computations. *Journal of Computational Physics* **72**, 449–466.

Pippard, A. & Chitty, L. 1952 A study of the voussoir arch. *Research Paper. London: National Building Studies: HMSO* .

Pippard, A., Tranter, E. & Chitty, L. 1936 The mechanics of the voussoir arch. *Journal of the Institution of Civil Engineers* **4**(2), 281–306.

Powrie, W. 1997 *Soil Mechanics - Concepts and applications.* Chapman and Hall,London,UK.

Prandtl, L. 1921 ber die eindringungsfestigkeit (hrte) plastischer baustoffe und die festigkeit von schneiden. *Zeitschrift fr angewandte Mathematik und Mechanik* **1**, 15 20.

Pritchard, T. 2004 Novel techniques in structural layout optimisation. *PhD Thesis - University of Sheffield* .

Rankine, W. 1857 On the stability of loose earth. *Philosophical Transactions of the Royal Society* **147**, 9–27.

Rozvany, G., Bendsøe, M. & Kirsch, U. 1995 Layout optimization of strucures. *Applied Mechanics Reviews* **48**, 41–119.

Shiau, J., Lyamin, A. & Sloan, S. 2003 Bearing capacity of a sand layer on clay by finite element limit analysis. *Canadian Geotechnical Journal* **40**, 900–915.

Sicilia, C., Pande, G. & Hughes, T. 2001 A homogenisation-based FE model for the analysis of masonry arch bridges. *Proceedings of the 3rd International Arch Bridges Conference, Paris* pp. 465–470.

Sigmund, O. 2000 Topology optimization: A tool for the tailoring of structures and materials. *Philosophical Transactions of the Royal Society of London* **358**, 211–227.

Sloan, S. 1988 Lower bound limit analysis using finite elements and linear programming. *International Journal for Numerical and Analytical Methods in Geomechanics* **12**, 61–77.

Sloan, S. 1989 Upper bound limit analysis using finite elements and linear programming. *International Journal for Numerical and Analytical Methods in Geomechanics* **13**, 263–282.

Sloan, S. & Kleeman, P. 1995 Upper bound limit analysis using discontinuous velocity fields. *Computer Methods Applied Mechancis and Engineering* **127**, 293–314.

Sloan, S. & Randolph, M. 1982 Numerical prediction of collapse loads using finite element methods. *International Journal for Numerical and Analytical Methods in Geomechanics* **6**, 47–76.

Smith, C. & Gilbert, M. 2007 Application of discontinuity layout optimization to plane plasticity problems. *Proceedings of the Royal Society A: Mathematical, Physical and Engineering Sciences* **463**(2086), 2461–2484.

Sokolovskii, V. 1965 *Statics of granular media.* Pregamon press Ltd, Oxford, London.

Thavalingam, A., Bicanic, N., Robinson, J. & D.A., P. 2001 Computational framework for discontinuous modelling of masonry arch bridges. *Computers and Structures* **79**, 1821–1830.

Tin-Loi, F. & Ngo, N. 2003 Performance of the p-version finite element method for limit analysis. *International Journal of Mechanical Sciences* **45**, 1149–1166.

Topping, B. 1984 Shape optimization of skeletal structures : A review. *ASCE: Journal of Structural Engineering* **109**, 1933–1951.

Tresca, H. 1864 Sur i'ecoulement des corps solides soumis a de fortes pressions. *C.R. Acas. Sci. (Paris)* **59**, 754.

Ukritchon, B. & Klangvijit, C. 2003 Calculations of bearing capacity factor n_γ using numerical limit analyses. *ASCE: Journal of Geotechnical and Geoenvironmental Engineering* **5**, 468–474.

Vanderbei, R. 1998 Linear programming: Foundations and extensions. *Kluwer Academic Publishers, London, UK* .

Von Mises, R. 1913 Mechanik der festen korper im plastisch deformablen zustand. *Gottin. Nacher. Math. Phys.* **1**, 582592.

Von Mises, R. 1928 Mechanik der plastischen formaenderung von kristallen. *Z. angew. Math. Meek* **8**, 161–185.

Yu, H., Houlsby, G. & Burd, H. 1991 A rational displacement interpolation function for axisymmetric finite element analysis of nearly incompressible materials. *Finite Elements in Analysis and Design - Elsevier Science Publishers* **10**, 205–219.

Yu, H., Sloan, S. & Kleeman, P. 1994 A quaratic element for upperbound limit analysis. *Engineering Computations* **11**, 195–212.

Zienkiewicz, O., Taylor, R. & Too, T. 1971 Reduced integration technique in general analysis of plates and shells. *International Journal for Numerical Methods in Engineering* **3**, 275–290.

Zienkiewicz, O., Taylor, R. & Too, T. 1976 Reduced integration, function smoothing and non-conformity in finite element analysis (with special reference to thick plates). *Journal of The Franklin Institute* **302**, 443–461.

Zouain, N. & Herskovits, J. 1993 An iterative algorithm for limit analysis with non-linear yield functions. *International Journal of Solids and Structures* **30**, 1397–1417.

Appendix A
Mathematical programming

Mathematical Programming is an operations research technique that solves problems in which an optimal value is sought subject to specified constraints. Mathematical programming models include linear programming, quadratic programming, and dynamic programming. In a mathematical programming or optimization problem, one seeks to minimize or maximize a real function of real or integer variables, subject to constraints on the variables. The term mathematical programming refers to the study of these problems: their mathematical properties, the development and implementation of algorithms to solve these problems, and the application of these algorithms to real world problems.
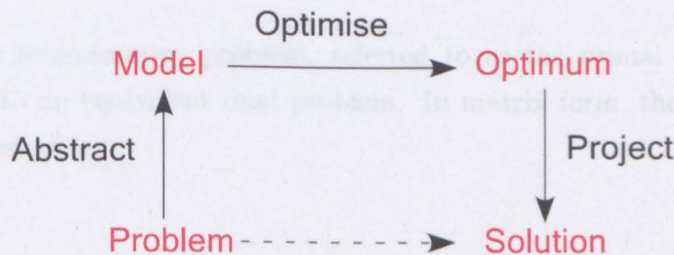
FIGURE A.1: Mathematical programming features

There are two popular methods in use today: the Simplex method and Interior-point method. The simplex method as introduced by Dantzig (1963) has been

the standard technique for solving linear programming problems since the 1940s . The simplex method passes from vertex to vertex on the boundary of the feasible polyhedron, repeatedly increasing the objective function until either an optimal solution is found, or it is established that no solution exists. In principle, the time required might be an exponential function of the number of variables, and this can happen in some contrived cases. In practice, however, the method is highly efficient, typically requiring a number of steps which is just a small multiple of the number of variables. Linear programs in thousands or even millions of variables are routinely solved using the simplex method on modern computers. Efficient, highly sophisticated implementations are available in the form of computer software packages.

Karmarkar (1984) introduced an interior-point method for linear programming. This method does not pass from vertex to vertex, but passes only through the interior of the feasible region. The analysis of interior-point methods is much less easily understood than the behavior of the simplex method. Interior-point methods are now generally considered competitive with the simplex method in most, though not all, applications, and sophisticated software packages implementing them are now available.

A.1 Linear programming and duality concept

Every linear programming problem, referred to as the primal problem, can be converted into an equivalent dual problem. In matrix form, the primal problem can be expressed as:

$$\text{maximize } c^T x$$

$$\text{subjec to } Ax \leq b \tag{A.1}$$

$$x \geq 0$$

the corresponding dual problem is:

$$\text{maximize } b^T y$$

$$\text{subjec to } A^T y \geq c \tag{A.2}$$

$$y \geq 0$$

where y is used instead of x as the variable vector.

There are two ideas fundamental to duality theory. One is the fact that the dual of a dual linear program is the original primal linear program. Additionally, every feasible solution for a linear program gives a bound on the optimal value of the objective function of its dual. The weak duality theorem states that the objective function value of the dual at any feasible solution is always greater than or equal to the objective function value of the primal at any feasible solution. The strong duality theorem states that if the primal has an optimal solution, x^*, then the dual also has an optimal solution, y^*, such that $c^T x^* = b^T y^*$.

A linear program can also be unbounded or infeasible. Duality theory tells us that if the primal is unbounded then the dual is infeasible by the weak duality theorem. Likewise, if the dual is unbounded, then the primal must be infeasible. However, it is possible for both the dual and the primal to be infeasible.

A full explanation of LP theory can be found in a number of books, most notably, Dantzig (1963),Vanderbei (1998), Nash & Sofer (1996).

Appendix B

Finite element limit analysis - computer code

There are number of programming languages available at the moment, however there is no perfect language. It all depends on the tools and the objective. For the development of engineering software, the C++ object oriented language is probably a good choice. It provides flexible data structures and easy reuse of codes. In this chapter, a short review of the basic features of object oriented programming will be presented.

B.1 Object-oriented programming

The object oriented programming approach considers a problem as a collection of objects. Each object is a structure that can contain both data and function and more importantly can communicate with other objects. Therefore the program can be described as a collection of interacting objects. Object-oriented programming is an organizational style, but it helps programmers create reusable code because the code to do a specific thing is entirely contained within a single section of code, and to use the code to perform tasks - for instance, creating a menu - involves using

179

only a small number of functions to access the internals of the object. Object-oriented programming simplifies the transfer of source code from one program to another program by encapsulating it - putting it all in one place.

B.2 Classes and objects

In C++, the class forms the basis for object-oriented programming. The class is used to define the nature of an object, and it is C++'s basic unit of encapsulation. A class in C++ is a very flexible data structure, it associates several data items with each other. Classes, which can contain data and functions, introduce user-defined types into a program. User-defined types in traditional programming languages are collections of data which, taken together, describe an object's attributes and state. Class types in C++ enable programmer to describe attributes and state, and to define behavior.

B.3 The finite element limit analysis framework

The **fem** program is built upon a general limit analysis and design synthesis software framework developed by CLADU at the University of Sheffield. The main structure has been developed over many years following the first commercial **ring** software. Since then, a number of application have been developed, based on the framework. Examples include **fem, geo, form** and **ring**. Of these, two applications have been fully developed as commercial software, these are **ring** and **geo**. Important components of the framework are described below:

core is a C++ library providing the base structure for the framework. **core** has the following components: **clf** defines the base classes and the whole structure for the framework. **clv** is viewer toolbox, it contains viewers and forms that control the visual part of **clf**. **geometry** is a helper library which

allows construction of basic geometrical elements. **so** is a scene-object library built to create visual components of **clf**.

mpl is a C++ library and is used as a wrapper layer to give access to different mathematical programming solvers, for instance Mosek.

ult is a C++ library for computational limit analysis and design synthesis.

fem is the C++ library is developed for the current work. The flow chart of **fem** is shown in figure B.1. The basic classes of **fem** are:

Project : Project class is the basic class to create a project. This class can also create an MP problem. Use of the lower or upper bound approach can be specified so that when elements are constructed, a suitable corresponding matrix can be established.

Zone : Zone class is a container. The role of Zone class is to store all project elements.

StressPoint : the StressPoint class is used to create a geometry point and to the create stress variables for a point within the MP problem.

DisplacementPoint : the DisplacementPoint class is used to create a geometry point and and also create the displacement variables for a point within the MP problem.

TriangleElementLinear : the TriangleElementLinear class is constructed from three geometry points and a integer. The integer is used to defined the number of equilibrium constraints to be created for the MP problem. This class also establishes the equilibrium matrix for the element.

TriangleElementQuadratic : the TriangleElementQuadratic class is constructed from six geometry points. It used for upper bound analysis only.

BoundaryElement : the BoundaryElement class is used to define boundary conditions. It is constructed from either a point or a line. Depending on the specified requirements of the problem, the boundary condition can be set.

PolygonElement : the PolygonElement is constructed from a number of geometry points and an integer. The PolygonElement class is used to model the masonry elements.

DiscontinuityElement : the DiscontinuityElement class is constructed from elements that are contact with each other. This class is used to model the interface between elements.

BarElement : the BarElement class is used to model reinforcement. It is constructed from two geometry points.

MaterialMohrColumb : the MaterialMorhColumb class is used to model a MohrCoulomb yield surface, it imposes the yield or flow rule condition at a point.

MaterialRockingOrduna : the MaterialRockingOrduna class is used to model crushing failure of masonry.

MaterialSimple : the MaterialSimple class is used to define the material properties of a reinforced element.

```
                    ╭─────────╮
                    │  BEGIN  │
                    ╰─────────╯
                         │
               ╭───────────────────╮
               │   Input mesh data │
               │   from a text file│
               ╰───────────────────╯
                         │
           ╭───────────────────────────╮
           │ Assigning problem property│
           ╰───────────────────────────╯
                         │
             ╭───────────────────────╮
             │  Add problem variables│
             ╰───────────────────────╯
                         │
       ╭───────────────────────────────────────╮
       │        Set-up problem constraints     │
       │ (e.g equilibirum, yield, boundary,etc...)│
       ╰───────────────────────────────────────╯
                         │
             ╭───────────────────────╮        ╭──────────────────╮
             │        Solve          │◄───────│ Adding additional│
             ╰───────────────────────╯        │   constraints    │
                         │                     ╰──────────────────╯
                   ◇─────────────◇                    ▲
              Yield condition satisfied?──────────────┘
                   ◇─────────────◇
                         │
           ╭───────────────────────────╮
           │ Output solution:  stress, │
           │ strain contours, deformation,│
           │ principal stress and so on...│
           ╰───────────────────────────╯
                         │
                    ╭─────────╮
                    │   END   │
                    ╰─────────╯
```
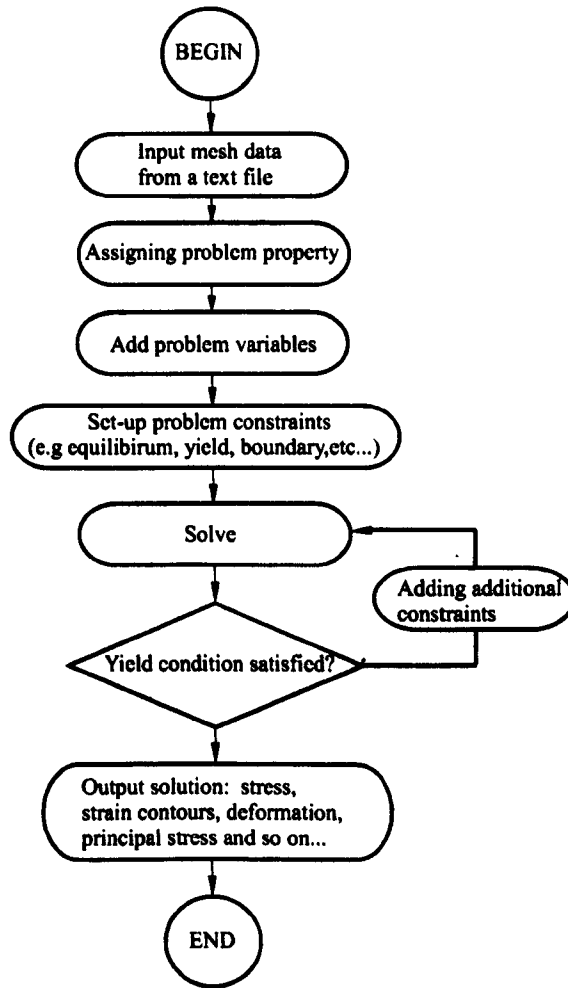
FIGURE B.1: Computer flow chart for **fem**

Appendix C

Simple model of concrete and steel beams

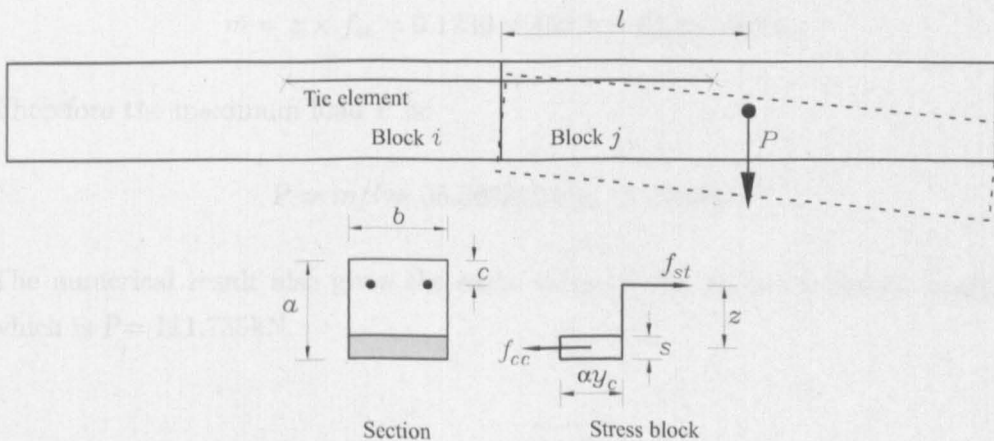## C.1 Two block cantilever beam analysis

FIGURE C.1: Two blocks with a strengthening element

Consider the example of 2 blocks connected to each other by a tie element as shown in figure C.1. Block i is fixed and load P is applied at the centroid of block j, distance $l = 0.5$m to the interface. The compressive strength of the blocks is

taken as $30\text{N}/\text{mm}^2$ (taking a reduction factor of $\alpha = 0.67$), and the block thickness $b = 0.2\text{m}$ and width $a = 0.2\text{m}$. The distance from the block edge to the centroid of the tie element is $c = 0.02\text{m}$. The two T25 tie elements have a tensile yield stress of $y_{st} = 460\text{N}/\text{mm}^2$, and section area of 490mm^2. Thus the tensile capacity offered by the tie elements is $2 \times 460 \times 490 = 450.8\text{kN}$. The objective is to find the maximum load P that can be carried by this structure. Similar to standard concrete beam design, and based on simple section analysis, the crush depth s can be computed as:

$$f_{cc} = s \times b \times \alpha \times y_c = f_{st}$$

thus

$$s = f_{st}/(b \times \alpha \times y_c) = 450.8/(0.2 \times 0.67 \times 30 \times 10^3) = 0.1121\text{m}$$

and the lever arm z can be calculated as:

$$z = a - c - s/2 = 0.2 - 0.02 - 0.11121/2 = 0.1239\text{m}.$$

Thus the resisting moment of the cross-section is

$$m = z \times f_{st} = 0.1239 \times 450.8 = 55.8678\text{kNm}.$$

Therefore the maximum load P is:

$$P = m/l = 55.8678/0.5 = 111.735\text{kN}.$$

The numerical result also gives the same value as the above analytical analysis, which is P= 111.735kN.

C.2 Concrete beam analysis

In this section, the capability of the numerical model to analysis a beam with pin and roller supports is verified. It is assumed that the beam is 6m in span, loaded at mid-span. The cross section of the beam has the following properties: effective
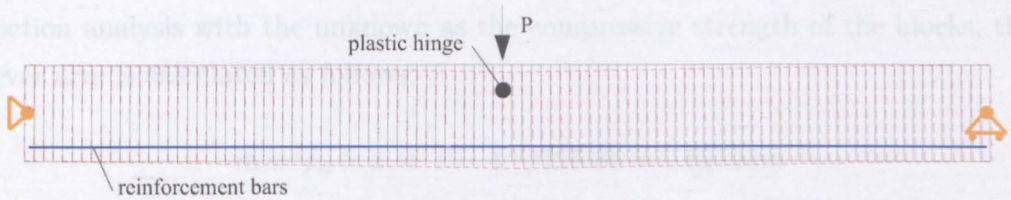
FIGURE C.2: $6m$ span concrete beam with pin and roller supports

width $d = 0.52$m, thickness $b = 0.3$m. Using 3T25 bars for bending resistance, provides 676.2kN tensile force. Using a similar analysis to the above procedure, the crushing depth is given by:

$$s = 676.2/(0.3 \times 0.67 \times 30 \times 10^3) = 0.11214\text{m}$$

and the lever arm:

$$z = 0.52 - 0.11214/2 = 0.464\text{m}$$

Therefore $m = 0.464 \times 676.2 = 313.709$, and P$= 4 \times m/l = 4 \times 313.709/3 = 209.14$kN, which is identical to the the numerical prediction.

C.3 Steel beam analysis

In order to model the steel beams used in the Salford experiments, it is necessary to verify that the above model is able to model a steel beam. The steel section has width $a = 0.05$m and thickness $b = 0.1$m. The plastic modulus of the beam section is given as $e_p = 17.5\text{cm}^3$, and the yield stress of steel is $y_{st} = 275\text{N/mm}^2$. Thus the plastic moment of the beam section can be calculated as (see e.g Mosley et al. (1995)):

$$m = e_p \times y_{st} = 17.5 \times 10^3 \times 275 = 4.8\text{kNm}$$

In order to replicate the steel beam using the above numerical model, each section of block is assumed to be similar to the steel section, giving $a = 0.05$m and $b = 0.1$m. The tie bar is assumed to consist of one T25 bar, thus the tensile capacity is $460 \times 491 = 225.86$kN. The assumed effective depth $d = 0.035$. Following standard

section analysis with the unknown as the compressive strength of the blocks, the lever arm is calculated as follows:

$$m = f_{st} \times z \Rightarrow z = 4.8/225.86 = 0.02125\text{m}$$

The crushing depth s can be calculated as: $s = 2 \times (d - z) = 0.0275\text{m}$. Therefore, the suitable compressive strength of block will be:

$$y_c = \frac{f_{st}}{s \times b} = \frac{225.86}{0.0275 \times 0.1} \approx 82 \times 10^3 \text{kN/m}^2 \text{ or } 82\text{N/mm}^2$$

With the above information, the 3m span steel beam can be modeled as shown
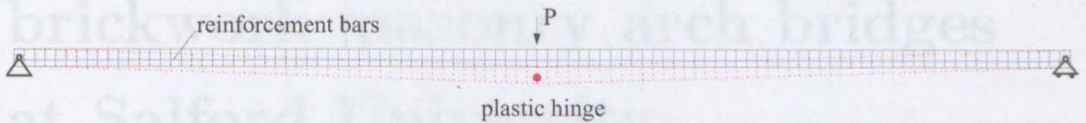

FIGURE C.3: 3m span steel beam with pin and roller supports

in figure C.3. The predicted ultimate collapse load is 6.4kN and the plastic hinge is formed at mid-span. The maximum load P can also be analytically worked out as:

$$P = 4 \times m/l = 4 \times 4.8/3 = 6.4\text{kN}$$

Therefore, the above model can be used to model the steel beam as used in the bridge tests.

Appendix D

Load test to collapse of back-filled brickwork masonry arch bridges at Salford University

The text in this appendix is taken verbatim or paraphrased from a series of data reports describing the Salford test series. These reports were authored by:

Matthew Gilbert, Colin C. Smith. *University of Sheffield, Department of Civil and Structural Engineering, Sheffield, UK*

J. Wang, C. Melbourne. *University of Salford, School of Computing, Science and Engineering, UK*

Phillip A. Callaway. *Network Rail, York, UK*

D.1 Introduction

D.1.1 Terms of reference

The test series was commissioned by Essex County Council as part of a programme of work to help more reliably determine the load carrying capacity of Essex County Council masonry arch bridges. The tests were designed by researchers from the Universities of Sheffield and Salford.

D.1.2 Test rig

Each test was carried out in the large Salford plane strain test rig. The dimensions of the test rig are shown in figure D.1. The frame was primarily constructed from heavy duty steel I sections (406 × 140 × 39UB, Grade S275) to ensure adequate stiffness so that the plane strain conditions were maintained under load. The frame was designed to ensure no end effects affected the results, taking into account the anticipated failure mechanisms. The length of the rig necessitated inclusion of several tie bars across the top and bottom of the frame to provide adequate lateral stiffness. The frame supported stiff walls consisting of 50mm thick plywood on the ends and along one side. On the other side, 50mm thick acrylic windows were incorporated in order that soil kinematics could be observed. Both walls had a further 6mm layer of acrylic sheet placed on their internal faces. The frame was the same for all tests, but the location of the arch barrel within the frame was changed for some tests.

D.1.3 Bridge and backfill geometry

The arch barrel was segmental and had a span of 3m, with a nominal span to rise ratio of 4 : 1. It consisted of two rings and alternate courses comprised headers. The back-fill materials used differed for each test and can be summarized as below
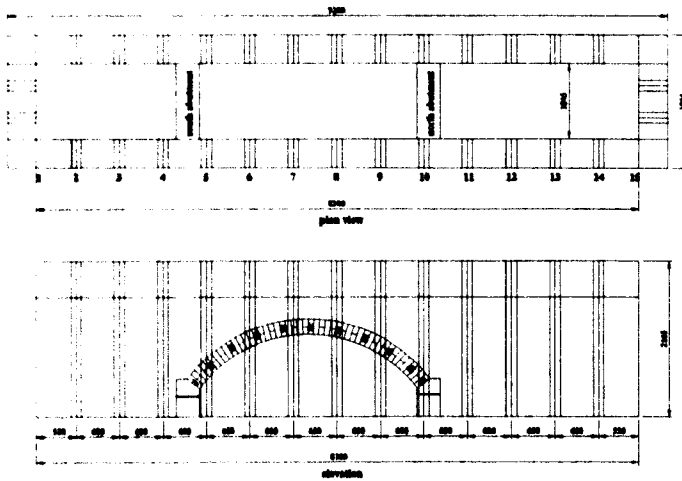
FIGURE D.1: Test rig (all dimensions in mm)

1. Arch01 was backfilled with crushed limestone.

2. Arch02 was backfilled with clay with a compacted limestone layer providing a fill depth of 300mm over the crown of the arch.

3. Arch03 is similar to Arch01 but with fixed abutments.

4. Arch05 is similar to Arch01 but with near-surface reinforcement (10No. 100× 50mm S275 steel channels, 3m long, centralized under load, replacing 50mm of fill)

5. Arch06 is similar to Arch02 but with near-surface reinforcement (10No. 100× 50mm S275 steel channels, 3m long, centralized under load, replacing 50mm of fill)

Material	Compressive Strength (N/mm^2)	Nominal Dimensions (mm)	Density (kg/m^3)
Class A engineering brick	154	215 x 102 x 65	2370
Mortar	1.9	-	1470-1570

TABLE D.1: Masonry properties

D.2 Materials

D.2.1 Bricks

Class A Engineering bricks (Marshalls Products Nori bricks) were used in the construction of the arch barrel. The average properties of the bricks are given in table D.1.

D.2.2 Mortar

The mortar, a 1 : 2 : 9 (cement:lime:sand) mix by volume was used throughout the arch barrel. The mean properties as determined from five 100mm cubes are presented in table D.1. The cubes were cured under the same conditions as the arch barrel.

D.2.3 Crushed limestone

The MOT Type 1 graded crushed limestone was sourced from Tarmac Central Ltd - Holme Hall Quarry. The soil properties were obtained from 300mm shear box tests carried out at normal stresses of 25kPa, 100kPa and 175kPa, employing 3 repeat tests for each stress level. Figure D.2 shows the shear stress against horizontal displacement obtained from the shear box test.
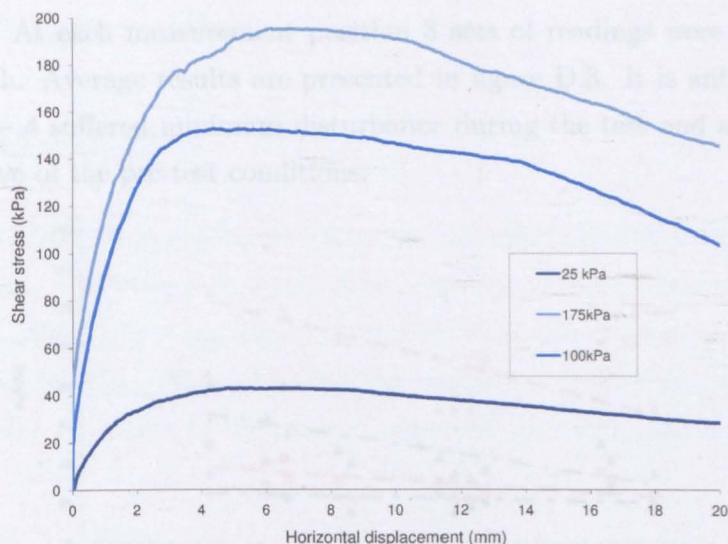
FIGURE D.2: Shear stress against horizontal displacement

D.2.4 Clay

The clay was supplied by Marchington Stone Ltd and was described as a firm reddish brown slightly sandy CLAY with occasional gravel. The supplier's determined index properties were as follows: natural moisture content 15%; optimum moisture content 9%; Liquid Limit 29%; Plastic Limit 12%. During placement of the clay, five readings were taken across the width of the tank at a range of locations using a pocket penetrometer. According to the manufacturer, the shear strength of purely cohesive materials can be obtained by dividing the scale reading by two. Following completion of the test, thirty-three 38mm diameter tube samples were retrieved from the exposed surfaces of the clay. Eighteen were retrieved from the surface beneath the limestone in line with columns $3 - 5$ and $9 - 14$ (2 per column across the width). The remaining fifteen were retrieved from the exposed face of the clay following removal of the plywood wall at depths 600mm and 900mm below the limestone base. Of these samples, fourteen were subjected to unconsolidated undrained (UU) tests. The bulk densities and moisture contents of the tested samples are plotted in Figure A.4, and the undrained shear strengths c_u are plotted in figure D.3. Both peak strengths and strengths mobilised at lower shear strains are plotted. Additional measurements were made using a 19mm

shear vane. At each measurement position 3 sets of readings were taken across the rig width. Average results are presented in figure D.3. It is anticipated that positions $2 - 4$ suffered minimum disturbance during the test and are thus most representative of the pre-test conditions.
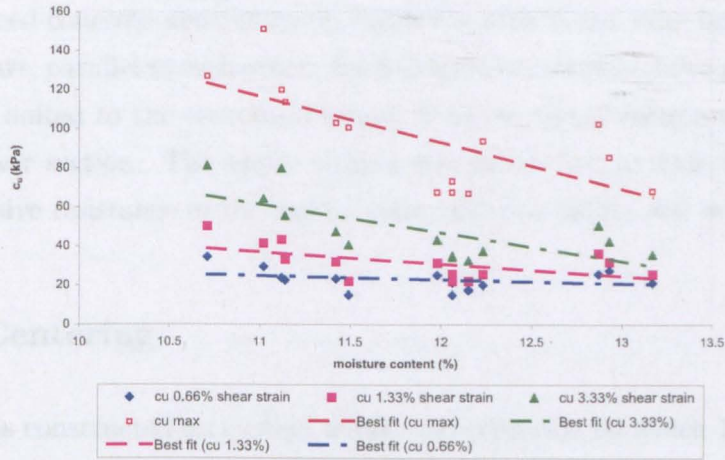

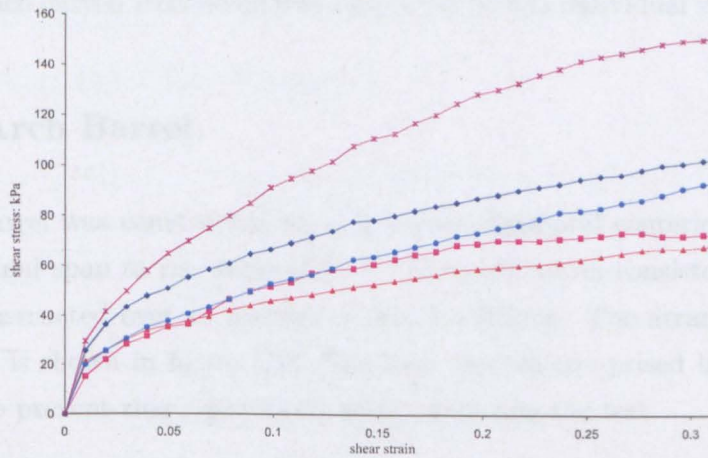FIGURE D.3: Peak and mobilised shear strengths of clay triaxial samples

FIGURE D.4: Clay shear strength vs strain

D.3   Construction

D.3.1   Abutments

Two reinforced concrete abutments on which the arch barrel were built were fixed 3000mm apart, parallel to each other. Each abutment comprised two parts: a lower section was bolted to the structural strong floor; an upper section was mortared onto the lower section. The upper section was hence free to slide once the frictional/adhesive resistance of the mortar joint between blocks was overcome.

D.3.2   Centering

The arch was constructed on custom made steel centering on which $101.6 \times 50.8 \times 1000$mm planks were placed, in turn covered by a sheet of plastic in order to minimise bonding of the masonry to the planks and facilitate easy removal of the centring. Each curved steel beam was supported by two individual stacks of bricks.

D.3.3   Arch Barrel

The arch barrel was constructed on a 3m span segmental centering (formwork), with a nominal span to rise ratio of 4 : 1. The arch barrel consisted of two rings and was constructed over an average width of 1010mm. The arrangement of the arch barrels is shown in figure D.5 .Alternate courses comprised headers. These were used to prevent ring-separation occurring during the test.

D.3.4   Tank construction

Following construction of the arch, the test frame was assembled around the arch. The average width of the test rig was 1045mm while the average width of the arch was 1010mm. In order to prevent fill falling between the gap between the arch
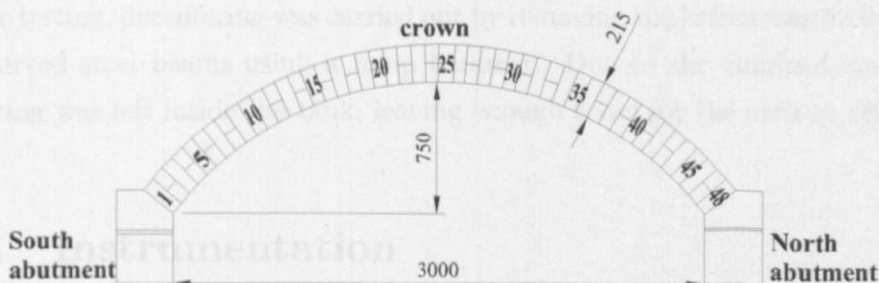
FIGURE D.5: General arrangement of the arch barrel

and the test rig walls, strips of closed cell foam were hotglued along the edges of the arch extrados so as to span the gap. The flexible foam was expected to accommodate any minor lateral arch movements while retaining the fill above.

D.3.5   Wall friction reduction

The tank was design to be sufficiently stiff to provide plane strain conditions. This meant that significant confining pressures might develop between the backfill and the tank sides. The consequence of these pressures would be to develop significant frictional forces. To minimise side wall friction, the full faces of the 6mm perspex sheets were covered in a layer of silicone grease followed by a 0.33mm thick latex sheet. Of those considered, greased latex offered the lowest friction angles for normal stresses greater than ≈ 5kPa. It was considered that such stresses would dominate in such a large model employing compacted backfill and with high stresses beneath the loading platen. For normal stresses greater than 10kPa, the interface friction angles of less than 2°.

D.3.6 Removal of centering

Before testing, decentering was carried out by removing the bricks which supported the curved steel beams using a lump hammer. Due to the confined space, the centering was left inside the tank, leaving enough room for the arch to deform.

D.4 Instrumentation

D.4.1 Deflection

Soil pressure cells are different for each tests. For the second test, four Linear Variable Differential Transformer (LVDT) type displacement transducers were placed beneath the intrados of the arch barrel to measure its movement. These gauges were capable of resolving displacements down to approx. 0.01mm. Figure D.6 shows the positions of these gauges. Two types of deflection gauges were used to measure the lateral movement of the test rig: nine LVDT type displacement transducers and six mechanical dial gauges with range of 50mm and accuracy of 0.01mm. They were placed horizontally against the test rig to monitor its movement. The positions of these gauges are shown in figure D.7.

D.4.2 Earth pressures

Soil pressure cells are different for each tests. From the second test onwards, a total of four soil pressure cells were embedded into the arch extrados (2No. Kyowa BER-A-200KP12S and 2No. Kyowa BER-A-500KP12S). The positions of these pressure cells are shown in Figure 4.4
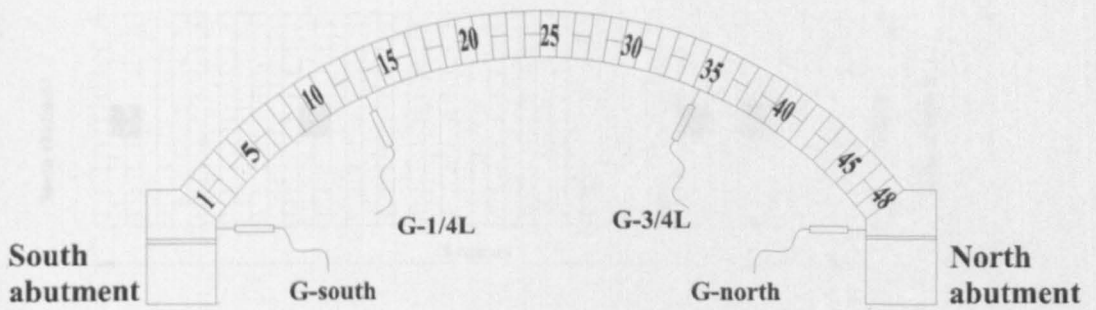
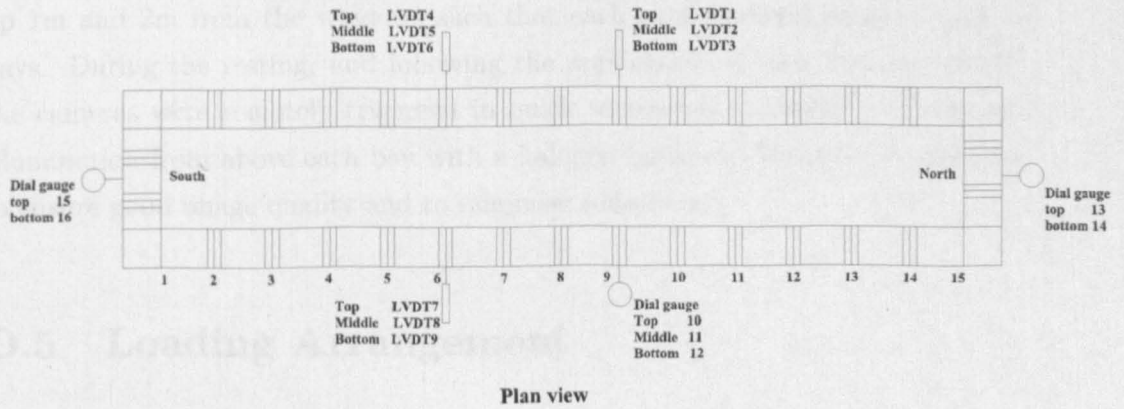FIGURE D.6: Layout of deflection gauges monitoring the arch

Plan view

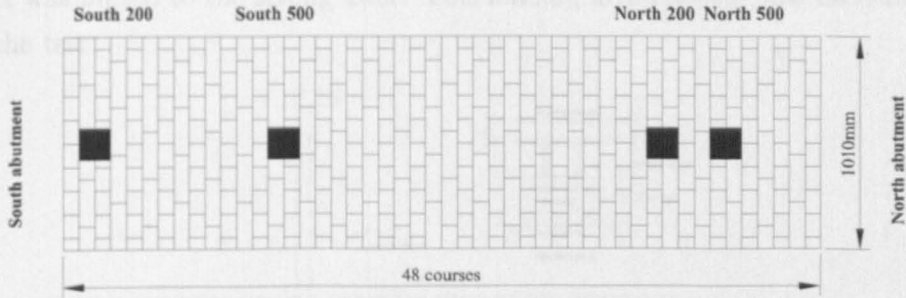FIGURE D.7: Layout of deflection gauges monitoring the rig

FIGURE D.8: Positions of pressure cells on arch extrados

D.4.3   Imaging

The frame provided 14 bays between the steel columns along its length. Of these, the middle 12 bays incorporated the acrylic windows. In order to capture the soil kinematics, a set of six SONY DSC-V1, 5MegaPixel, digital cameras were set up 1m and 2m from the windows such that each camera could image a pair of bays. During the testing, and following the application of each load increment, the cameras were remotely triggered in quick succession to capture the images. Illumination from above each bay with a halogen lamp was found to be essential to ensure good image quality and to minimise reflections.

D.5   Loading Arrangement

The loading arrangement was different for each test. Typically two hydraulic jacks supported from a steel reaction frame were used to apply a line load to the backfill at the south quarter of the arch. The load was applied vertically onto the surface of the backfill through a steel loading beam (base 920×219) resting on a wood

base 920×219 which was placed on the surface of the backfill, as shown in figure D.9. The two hydraulic jacks were used and loaded against a steel reaction frame which was bolted to the strong floor. This loading arrangement was used through out the test.
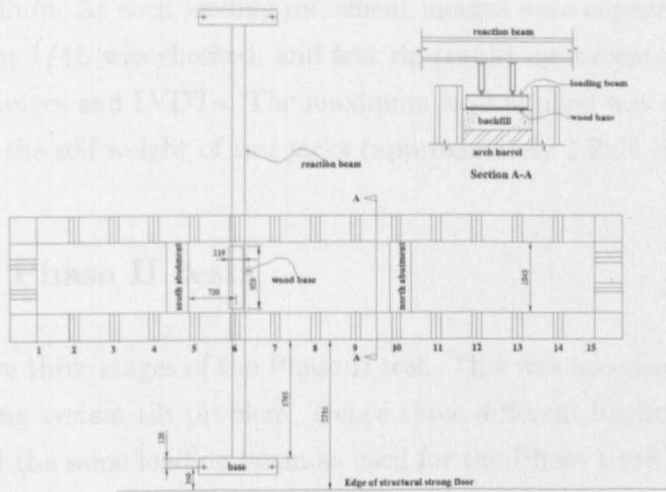
FIGURE D.9: Loading arrangement

D.6 Test Procedure

The test procedure for each test followed the same broad procedure. Here the procedure for Arch02 will be described as an example. This particular test was relatively complex due to events occurring certain stages of the test, and usefully illustrate the procedures followed. The test was carried out in two phases. The arch was taken to peak load in Phase I. In Phase II the arch was subjected to a large imposed displacement to observe the development of the post peak failure mechanism. The instrumentation, as described in Section 4, was monitored throughout all the tests

D.6.1 Phase I test

The nuts at the ends of the two tie bars connecting the abutments to the central column were first slackened off. The load was then applied in increments of approx. 5kN to failure. At each loading increment images were captured, the deflection of the arch at 1/4L was checked, and test rig (tank) movements were checked using the dial gauges and LVDTs. The maximum load applied was approximately 90kN including the self weight of two jacks (approximately 1.2kN each).

D.6.2 Phase II tests

There were three stages of the Phase II test. This was necessary due to recurrence of a loading system tilt problem. Hence three different loading beams were used. In Stage 1 the same loading beam as used for the Phase I test was employed. The problem of jack tilt occurred when the load reached to about 60kN. The load was subsequently removed. In Stage 2 a shallower steel beam was employed. At a load of approx. 60kN the jack tilt problem recurred once more. In Stage 3 the load was directly to the wood base through two steel platens. The load reached approx. 94kN, after which no further load could be applied.

Appendix E

DLO: Visualization of failure mechanisms

E.1 Solid identification procedure
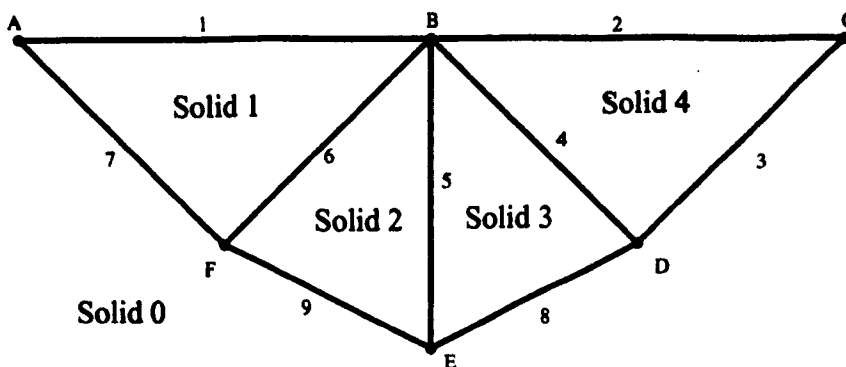
Figure E.1 shows the optimum layout of discontinuities for a simple strip footing resting on a cohesive soil (assuming that a vertical load is e.g. applied along edge AB). Since the product of a DLO solution is the optimum layout of discontinuities, only the relative displacements between solid elements are known, and both the geometry and absolute velocity of a given solid element are initially

unknown. A question therefore arises: how best to identify the displaced failure mechanism from a given set of discontinuities? The answer to this question was not immediately obvious. An initial thought was to plot moving dots along slip-lines. However, this will be difficult when normal and rotational displacements along interfaces are involved. Therefore, in order to visualize the failure mechanism, an obvious solution was to develop an algorithm to initially identify the solid elements.

This algorithm can be applied to the problem shown in figure E.1:

- Create a list of discontinuity end-points, as shown on figure E.2.

- For each end-point, add a list of pairs that contain discontinuities and solids (all solids are NULL at first).

- For each end-point, sort out pairs in a counter clockwise angular order (angle the discontinuity makes to that point).

- Start the identification process by looping through all end-points.

- At each end-point (called the 'master point'), loop through all pairs.

  1. At each pair, check if the solid is NULL.

  2. If solid is NULL, create a solid and assign the solid to the pair, carrying out the process below.

     (a) Determine the other end-point of the discontinuity.

     (b) End the loop if this end-point is the master point, if not carry on the loop.

     (c) At this stage find a pair that contains the same discontinuity.

     (d) Go to the pair that is immediately behind the previously identified pair. Assign the same solid to this pair.

The above process can further be explained by reference to figure E.2. Now, for example, the identification process starts form point A, where discontinuities 1 and

7 connect to it. Since the first pair at point A contain a NULL solid, Solid1 will be added to the first pair. Point B is end point of discontinuity 1, therefore solid 1 will also be added to the third pair at point B. Similarly, Solid1 will be added to second pair at point F. At second pair of point F, discontinuity 7 is actually connected to point A. The loop terminates and Solid1 is identified.

After all solids have been identified, the solid displacement phase can be performed. However, DLO provides only information on relative displacements (i.e. information on how solids move relative to each other), the next problem is how to work out the absolute displacement of a given solids. This will be illustrated in the next section.

Points	A		B		C		D		E		F	
Pairs	1	Solid 1	2		2	Solid 0	3	Solid 0	8	Solid 0	6	
	7	Solid 0	1	Solid 0	3		4		5		7	Solid 1
			6	Solid 1			8		9		9	Solid 0
			5									
			4									

FIGURE E.2: DLO problem: Optimum layout of discontinuities

E.2 On the calculation of solid absolute displacement

Fortunately, as can be seen in figure E.2, Solid0 is also identified from the above algorithm. Solid0 is actually constructed from all the outer discontinuities (discontinuities 1, 2, 3, 8, 9, 7). Moreover, Solid0 is stationary and its absolute displacement is zero. Therefore the absolute displacements of solids sharing the interface with Solid0 can be worked out. It means that that when solid absolute displacements are known, all the displacements of solids that are adjacent to it can be determined. The process is carried out as follows:

- Loop through the list of end-points as shown on figure E.2 (obviously, at this stage, all solids have been identified).

- At each point, looping through list of pairs.

- For a discontinuity at each pair, check if solids have been assigned. If not, assign the solid in the pair to the discontinuity. Also assign the solid of the pair below to the discontinuity.

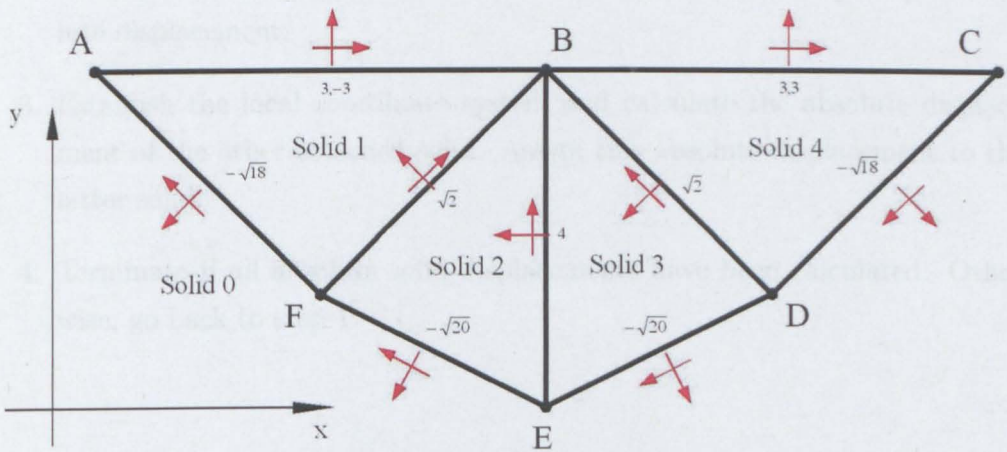- For a solid at each pair, assign the discontinuity to the solid.

FIGURE E.3: DLO problem: Relative displacements between solids

After this process, all discontinuities will contain information about their adjacent solids and all solids contain theirs discontinuities. The determination of the absolute displacement first involves transformation of the local coordinate axes (shown as red arrows in figure E.3) into the global coordinate system. However, before this can take place, the directions of the local coordinates need to be worked out. It can be seen that the displacement of Solid1 is $(x = 3, y = -3)$ because the relative displacement of discontinuity 1 is $(n = 3, s = -3)$, where n, s are respectively the normal and shear relative displacements. However, it should be noted that the local coordinate system for discontinuity 1 is aligned with the global coordinate system. The orientation of the local coordinate system can be found from the arrangement of points in a solid. Fortunately, the arrangement of points for

ᵗ

the solids shown in figure E.3 are all in a clockwise order. For Solid0 and Solid1, when the relative displacement of discontinuity 1 is taken into account, the local shearing direction is from point A to B. Similarly, for Solid0 and Solid1, when the relative displacement of discontinuity 7 is taken into account, the local shearing direction is from point F to point A. Generally, the absolute displacement of solids can be determined as follows:

1. Loop through all discontinuities.

2. At each discontinuity, check if at least one attached solid has a known absolute displacement.

3. Establish the local coordinate system and calculate the absolute displacement of the other attached solid. Assign this absolute displacement to this latter solid.

4. Terminate if all absolute solid displacements have been calculated. Otherwise, go back to step 1.